



POLITECNICO
MILANO 1863

SCUOLA DI INGEGNERIA INDUSTRIALE
E DELL'INFORMAZIONE

Development and experimental methods for ultra-high dose-rate radiation therapy using alanine dosimetry

TESI DI LAUREA MAGISTRALE IN
NUCLEAR ENGINEERING - INGEGNERIA NUCLEARE

Author: **Elena Agostoni**

Student ID: 10863964

Advisor: Prof. Davide Bortot

Co-advisors: Dr. Ludovic De Marzi, Dr. François Trompier

Academic Year: 2024-2025

Abstract

FLASH radiotherapy is an innovative cancer technique that delivers ultra-high dose-rate irradiation. It has significant potential for increasing the therapeutic ratio by sparing healthy tissues while maintaining tumor control. Until now, the transition of FLASH from experimental studies to clinical application has faced many challenges, one of them concerning dosimetry and requiring accurate dose measurements at these high dose-rates. A promising dosimeter for FLASH is alanine and electron paramagnetic resonance (EPR) dosimetry, also referred to as alanine/EPR dosimetry, due to its large dose-rate independence, high stability, and wide dynamic range.

Indeed, this thesis deals with the development and experimental characterization of dosimetric methods for ultra-high dose-rate irradiation using alanine dosimetry and Electron Paramagnetic Resonance (EPR) spectroscopy.

Furthermore, different dosimeters were evaluated and compared with EPR dosimetry, notably ionization chambers, radiochromic films and diamond detectors, with experimental irradiations delivered using proton and electron beams under conventional and FLASH conditions. The work was carried out in collaboration with two research institutions, including the Institut Curie (ICPO) and Institut de Radioprotection et de Sécurité Nucléaire (IRSN).

The results confirm the feasibility of alanine dosimetry and a protocol was developed for use in future FLASH applications. The study also highlights key factors influencing dosimetric accuracy, such as beam energy, Linear Energy Transfer (LET) effects for proton irradiation, and environmental parameters. Python scripts for EPR data analysis, that can be found in Appendix A, were also developed and tested with experimental data. This research contributes to the ongoing efforts to establish robust dosimetric protocols for FLASH therapy, paving the way for its safe and effective clinical implementation.

Keywords: FLASH radiotherapy, high dose-rate, alanine dosimetry, electron paramagnetic resonance, EPR, ionization chambers, proton therapy, radiochromic film, dosimetry protocols.

Abstract in lingua italiana

La radioterapia FLASH è una tecnica innovativa per il trattamento del cancro che impiega un’irradiazione a dose ultra-elevata. Essa presenta un significativo potenziale nell’aumentare il rapporto terapeutico, consentendo una maggiore protezione dei tessuti sani pur mantenendo l’efficacia nel controllo tumorale. Tuttavia, la transizione della FLASH dagli studi sperimentali all’applicazione clinica ha incontrato numerose difficoltà, tra cui una delle principali riguarda la dosimetria, che richiede misurazioni di dose estremamente accurate a questi alti ratei di dose.

Un dosimetro promettente per la FLASH è lalanina combinata alla risonanza paramagnetica elettronica (EPR), nota anche come dosimetria alanina/EPR, grazie alla sua ampia indipendenza dal rateo di dose, elevata stabilità e ampio range dinamico.

Questa tesi si concentra sullo sviluppo e sulla caratterizzazione sperimentale di metodi dosimetrici per l’irradiazione a dose ultra-elevata utilizzando la dosimetria con alanina e la spettroscopia EPR.

Inoltre, diversi dosimetri sono stati valutati e confrontati con la dosimetria EPR, in particolare le camere a ionizzazione, le pellicole radio-cromiche e i rivelatori a diamante, attraverso irradiazioni sperimentali con fasci di protoni ed elettroni in condizioni sia convenzionali che FLASH. Lo studio è stato condotto in collaborazione con due istituti di ricerca: l’Institut Curie (ICPO) e l’Institut de Radioprotection et de Sécurité Nucléaire (IRSN).

I risultati confermano la fattibilità della dosimetria con alanina e hanno portato allo sviluppo di un protocollo per future applicazioni FLASH. Lo studio evidenzia inoltre i principali fattori che influenzano l’accuratezza dosimetrica, come l’energia del fascio, gli effetti del Linear Energy Transfer (LET) per l’irradiazione con protoni e i parametri ambientali. Sono stati inoltre sviluppati e testati con dati sperimentali degli script Python per l’analisi EPR, disponibili in Appendice A.

Questa ricerca contribuisce agli sforzi in corso per stabilire protocolli dosimetrici affidabili per la terapia FLASH, aprendo la strada alla sua implementazione clinica sicura ed

efficace.

Parole chiave: radioterapia FLASH, alta dose, dosimetria con alanina, risonanza paramagnetica elettronica, EPR, camere a ionizzazione, terapia protonica, film radiocromici, protocolli dosimetrici.

Contents

Abstract	i
Abstract in lingua italiana	iii
Contents	v
1 Introduction	1
1.1 Preliminary remarks	1
1.2 Ionizing radiation	2
1.3 Linear Energy Transfer - LET	6
1.3.1 Restricted LET	6
1.3.2 Unrestricted LET	7
1.3.3 Dose averaged and track averaged LET definitions	8
1.4 Radiation therapy and FLASH	9
1.5 FLASH effect and dosimetry challenges	11
1.6 Radiation detection and dosimetry	14
1.6.1 Dosimetric quantities	14
1.7 Important concepts of dosimetry	16
2 Materials and methods	19
2.1 Dosimeters	19
2.1.1 Ion chamber detector	19
2.1.2 Diamond detector	21
2.1.3 Dosimetry protocol: Technical Reports Series N° 398	24
2.1.4 Film dosimetry	26
2.1.5 Film dosimetry protocols	29
2.1.6 Alanine	32
2.2 Electron Paramagnetic Resonance	35
2.2.1 The Zeeman Effect	35

2.2.2	Hyperfine Interactions	37
2.2.3	EPR spectrometer	38
2.2.4	EPR dosimetry	40
2.2.5	Alanine dosimetry protocols	45
2.2.6	Data analysis and signal manipulation for alanine dosimetry	46
2.2.7	Statistical analysis and Monte Carlo method	48
2.3	Irradiation facilities	49
2.3.1	Proton accelerator and gantry	49
2.3.2	How to irradiate dosimeters at the proton gantry	51
2.3.3	Electron FLASH LINAC	52
2.3.4	How to irradiate dosimeters at LINAC	53
3	Results	57
3.1	EPR parameter optimization	57
3.1.1	Modulation amplitude optimization	58
3.1.2	Microwave power optimization	61
3.1.3	Field sweep time optimization	64
3.1.4	Cavity temperature	65
3.2	Estimation of a dose calibration curve for proton irradiation	67
3.2.1	Irradiation in solid water phantom	68
3.2.2	Irradiation in water	69
3.2.3	Blind test	70
3.3	LET effects in a proton beam	71
3.3.1	Irradiation at different initial beam energies	71
3.3.2	Statistical analysis for different energies irradiation	72
3.3.3	Bragg peak measurement	73
3.3.4	Monte Carlo simulations	76
3.3.5	Discussion and radical investigation	79
3.4	Conventional and FLASH electron beam irradiation	83
3.4.1	Alanine and film dosimetry	83
3.4.2	Detectors inter-comparison	84
4	Conclusion	89
4.1	Future developments	90
Bibliography		91

A Appendix A	97
A.1 Film reading script	97
A.2 Saturation curve fit	98
A.3 Calibration curve	101
A.4 Bragg Peak curve	104
A.5 Alanine and film comparison (conventional and FLASH)	107
A.6 Detector inter-comparison	110
A.7 TOPAS simulation script	112
A.8 Alanine TOPAS construction	114
A.8.1 Alanine dosimeter composition and geometry	114
A.8.2 Alanine dosimeter construction	115
A.8.3 Alanine pellet geometry definition	115
A.8.4 Cylinder alanine geometry	115
B Appendix B	117
B.1 Images	117
C Appendix C	119
C.1 Tables	119
List of Figures	123
List of Tables	127

1 | Introduction

1.1. Preliminary remarks

Radiotherapy is currently one of the main techniques used to treat cancer. More than 50% of patients treated for cancer (around 180,000 a year in France and 200,000 in Italy) benefit from radiotherapy each year. However, tolerance of healthy tissue remains the main limitation of this type of treatment, especially in the case of particularly sensitive patients such as children, for whom controlling the side-effects of radiotherapy remains a major therapeutic challenge, or in the case of highly resistant tumors. Recently, innovative work initiated in France has demonstrated that ultra-high dose-rate irradiation (known as FLASH) has a major effect in sparing healthy tissue while preserving anti-tumour efficacy [1]. As irradiation with dose-rates several orders of magnitude higher than those of conventional radiotherapy present major metrological challenges, work on the dosimetry aspect of FLASH irradiation (monitoring, quality control, absolute dosimetry) is needed to secure the development of these irradiation techniques and enable their translation to clinical applications. Electron paramagnetic resonance (EPR) dosimetry uses solid materials such as alanine (an amino acid with a density close to that of water), which have great potential for application in radiotherapy thanks to their highly favorable dosimetric properties. Irradiation of this type of material leads to the generation of paramagnetic species (radicals that are stable over time), the number of which is proportional to the absorbed dose. The dose can be determined by estimating the absorption spectrum of unpaired electrons at a specific resonance frequency in a variable magnetic field. There are many possible applications of EPR dosimetry currently under study: in vivo dosimetry, small fields, remote audits and inter-comparisons, FLASH radiotherapy, magnetic field irradiation, neutron dosimetry, etc. However, this technique is not yet widely used due to a number of implementation difficulties, such as cost, complexity and low sensitivity for low doses (<5Gy). The thesis work is therefore part of an effort to improve methods for ionizing radiation dosimetry under specific conditions (high LET, high dose-rates). In this thesis, different detectors have been used (in particular ionization chambers in conventional mode and radiochromic films) as well as EPR with alanine dosimetry, and then

compared for various types of beams (protons, electrons, FLASH). Preliminary measurements have been analysed in collaboration with the Institut Curie and IRSN (Institut de Radioprotection et de Sécurité Nucléaire) in France, demonstrating the potential of alanine on this type of beams. In the following sections, we will detail the context, materials and methods used to achieve this.

1.2. Ionizing radiation

Radiation can be released from atomic or nuclear processes, in spontaneous or accelerator-driven emissions, and if it has enough energy to remove bound electrons from atoms or molecules, ionization processes can be added to excitation or heat transfer processes. Charged particles like electrons, ions and protons can directly ionize the atoms they encounter, while non-charged particles like gamma, x-rays and neutrons will be able to ionize the medium through secondary processes. The former will thus be called directly ionizing radiation, while the latter indirectly ionizing radiation. Particles are also distinguished between heavy particles or light particles. The heavy particles such as carbon ions and light particles such as protons ($m_p = 938.27 \frac{MeV}{c^2}$) are more densely ionizing than photons or electrons, and create secondary electrons and ions along their tracks. Their path in matter is overall straight since their mass is high (though multiple scattering occurs), and their energy loss per unit length can be well described by the Bethe-Bloch equation 1.1, which characterizes the stopping power of the material, $\frac{dE}{dx}$.

$$-\frac{dE}{dx} = K z^2 \frac{Z}{A} \frac{1}{\beta^2} \left[\frac{1}{2} \ln \left(\frac{2m_e c^2 \beta^2 \gamma^2 T_{max}}{I^2} \right) - \beta^2 - \frac{\delta}{2} \right] \quad (1.1)$$

where Z and A are the atomic number and atomic mass number of the medium, β is the ratio between the incoming particle's velocity and the speed of light, γ is the Lorentz's factor, T_{max} is the maximum kinetic energy transferable in one collision, I is the mean excitation potential of the medium, δ is a density correction for high energy, z is the charge of the incident particle and K is a constant. Stopping power can also be denominated with the denomination S, and the dependence on materials can also partly removed by using the mass stopping power, which is S divided by the density ρ .

For light or heavy particles, the stopping power increases significantly as the particle's velocity decreases, which leads to the characteristic Bragg peak shape at the end of their range. The Bragg peak consists in a sharp increase of ionization, and thus energy deposition, towards the end of a heavy charged particle's range. This is due to the inverse dependence between stopping power and velocity in the Bethe Bloch formula.

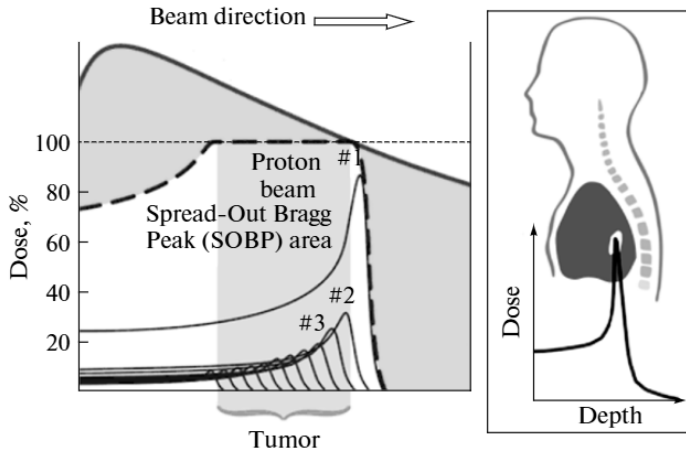


Figure 1.1: Spread out Bragg peak (SOBP) and comparison with a high energy proton beam (shaded area). The proton's range is adapted to the tumor's depth.

This characteristic shape holds the possibility to deliver most of a particle's energy to a specific depth in tissue, which can be regulated by choosing a certain entrance energy. On the other hand, the proximal area (before the peak) and the distal area (after the peak) present a much lower energy deposition. This is ideal for cancer treatment, because it leads to significant healthy tissue sparing compared to other particle types (e.g: photons). In addition, in clinical applications, the incoming particle's energy and intensity can be modulated so that the superimposed Bragg peaks form a flat plateau over the region of the tumor, called spread out Bragg peak (SOBP), that we can see in Figure 1.1.

Light particles such as electrons ($m_e = 0.511 \frac{MeV}{c^2}$), on the other hand, present a much different behavior. Because of their small mass they undergo significant deflection during multiple scattering leading to a chaotic trajectory, rather than the straight one typical of heavy charged particles. Their energy loss mechanisms can be broadly divided into collisional and radiative processes. Collisional losses ($-\frac{dE}{dx}_{\text{coll}}$) represent ionizations and excitations, while radiative losses ($-\frac{dE}{dx}_{\text{rad}}$), which mostly happen at higher energies, mark the emission of bremsstrahlung radiation: a continuous-spectra x-ray emission created by the deceleration of the electron by the electric field of an atom.

$$-\frac{dE}{dx}_{\text{rad}} = \frac{E}{X_0} \quad (1.2)$$

Where E is the energy of the electron and X_0 is the radiation length of the material of a

material with atomic number Z.

$$X_0 = \frac{716.4 \text{ g/cm}^2}{Z(Z+1) \ln(287/\sqrt{Z})} \quad (1.3)$$

$$-\frac{dE}{dx}_{\text{coll}} = \frac{4\pi N_A r_e^2 m_e c^2 Z}{A \beta^2} \left[\ln \left(\frac{T_{\max}(T_{\max} + 2m_e c^2)}{I^2} \right) - 2\beta^2 \right] \quad (1.4)$$

Where r_e is the electron radius. The range of electrons in matter depends heavily on their initial energy and is less predictable due to their scattering behavior. If we were to plot energy deposition against depth for electrons we would see no Bragg peak but instead a moderate dose increase and then rapid decrease caused by the buildup of secondary radiation and energy losses processes.

Finally, photons interact with matter in a fundamentally different way due to their lack of charge and mass. Photons do not lose energy continuously (as charged particles do) but in a discrete way at distant points along their path. These interactions result in the production of energetic secondary radiation such as electrons, which are responsible for the majority of the energy deposition in the medium.

The main interaction processes for photons are, in order of growing photon energy: photoelectric effect, Compton scattering and pair production ($E_\gamma > 1.022 \text{ MeV}$). For photons, the absorbed dose D is given by

$$D = \Phi \cdot E \cdot \frac{\mu_{en}}{\rho} \quad (1.5)$$

Where $\frac{\mu_{en}}{\rho}$ is the mass energy absorption coefficient [m^2/kg], which represents the fraction of energy transferred to the material. For charged particles, we can link stopping power and dose using the following relation:

$$D = \Phi \cdot \frac{S}{\rho} \quad (1.6)$$

Where Φ is the fluence, D [Gy] is the absorbed dose, S [$\frac{\text{MeV}}{\text{cm}}$] is the stopping power and ρ [$\frac{\text{kg}}{\text{cm}^3}$] is the mass density of the material.

In radiation therapy, knowing the electronic density as well as atomic composition of the tissue is crucial to convert the interaction processes (through stopping power or attenuation) into an actual dose value, since different tissues (bone, muscle, lung, etc.) have different densities.

We can also describe and compare the behavior of different particles when depositing dose

into the medium, which is showcased in Figure 1.2. Furthermore, we can introduce the equation for a particle's range:

$$R = \int_0^{E_0} \frac{1}{S(E')} dE' \quad (1.7)$$

Where E_0 is the initial kinetic energy of the particle, R is the continuous slowing down approximation (CSDA) range and $S(E)$ is the linear stopping power.

Some rule-of-thumb values of energy and range for different particles are reported in Table 1.1. While no single reference provides this exact tabulation, the numbers are based on commonly accepted ranges derived from multiple sources and experimental data.

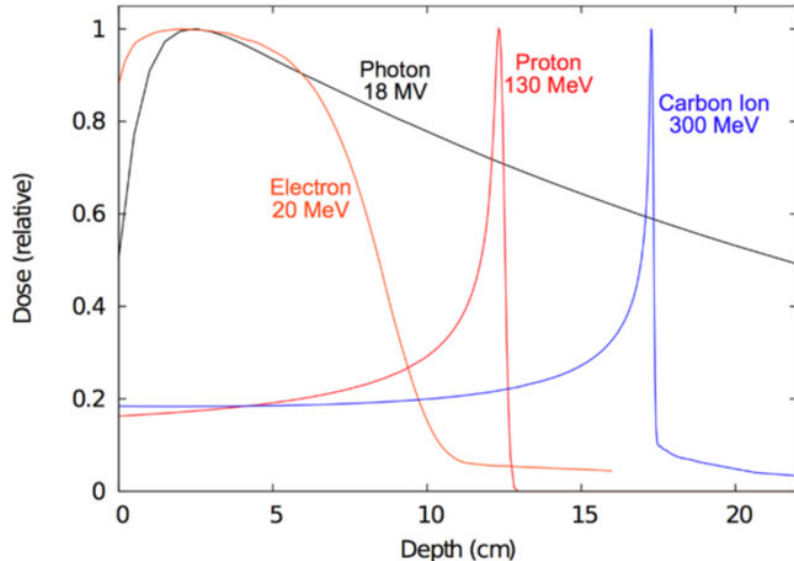


Figure 1.2: Relative dose deposition in depth in water for different particles.

Table 1.1: Average values for energy and range in water for particles employed in radiotherapy.

Radiation Type	Energy Range	Penetration Depth
Protons	60-250 MeV	6-30 cm
Electrons	6-20 MeV	3-10 cm
Carbon Ions	120-400 MeV/nucleon	8-30 cm
Photons	6-18 MV	10-25 cm

1.3. Linear Energy Transfer - LET

The energy deposition of a charged particle cannot be characterized only with quantities as the absorbed dose or the stopping power. This is because the energy deposition is not local, but also happens in depth and radially, because of secondary particles. Some simplification of this behavior can be taken into account, such as the continuous slowing down approximation, where we hypothesize that the particle loses energy continuously and smoothly along its trajectory, and we can neglect secondary particle transport outside the primary path, also called a track. The accuracy of this approximation is dependent also on a quantity called linear energy transfer. Given a certain material, the linear energy transfer (LET), or restricted linear electronic stopping power, L_Δ , for charged particles of a given type and energy is the quotient $\frac{dE_\Delta}{dl}$. dE_Δ is the mean energy lost by the charged particles due to electronic interactions in traversing a distance dl , minus the mean sum of the kinetic energies in excess of Δ of all the electrons released by the charged particles.

We will use the definitions provided in ICRU report number 16 [2] and number 60 [3], and describe the formerly mentioned quantities in the following sections.

1.3.1. Restricted LET

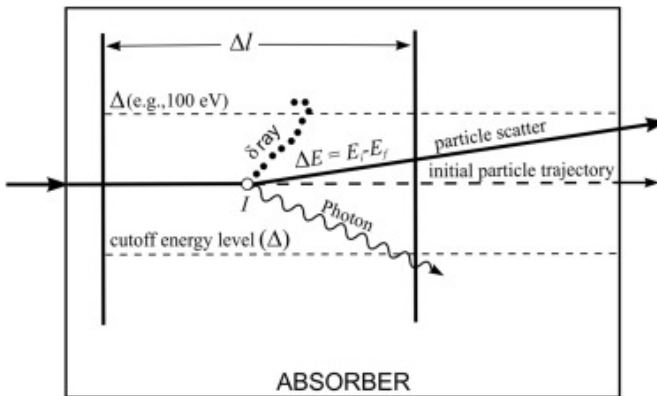


Figure 1.3: Cylinder model for energy deposition and cut-off definitions used for (un)restricted LET calculations .

Let us suppose, in first approximation, that the energy is deposited in two coaxial cylinders, whose axis is the primary particle track (see figure 1.3). The inner cylinder is represented by the space covered by uniform energy deposition from secondary electrons from soft collisions or scatter (up to 100 eV). Most of the energy will be deposited this way (delta ray deposition will be considered significant if higher than 10 %). The outer

cylinder is represented by the space covered by delta ray energy deposition.

$$L_\Delta = S_{el} - \frac{dE_{ke,\Delta}}{dl} \quad (1.8)$$

Where S_{el} is the linear electronic stopping power and $dE_{ke,\Delta}$ is the sum of the kinetic energies, greater than Δ , of all the electrons released by the charged particle traversing a distance dl .

As ICRP [3] points out, the definition expresses the following balance: energy lost by the primary charged particle in collision with electrons, along a track segment dl , minus the energy carried away by secondary electrons having kinetic energies greater than Δ , equals energy considered as "locally transferred" although the definition specifies an energy cutoff, Δ , and not a range cutoff.

Older versions of ICRU reports (like the one from 1980) define the restricted LET simply as in the following equation:

$$L_\Delta = \frac{dE_\Delta}{dl} \quad (1.9)$$

Where the main difference is that in Equation 1.8, L_Δ includes the binding energy for all collisions and the threshold of the kinetic energy of the released electrons is Δ as opposed to Δ minus the binding energy.

If $\Delta = 100eV$, the inner radius is a few nanometers: the same dimension as a DNA strand (see figure 1.4).

1.3.2. Unrestricted LET

If one considers just one cylinder of infinite radius, meaning $\Delta = \infty$, the energy loss will appear again only along the track length. This represents a situation of continuous slowing down of the particles and the following equation can be derived

$$L_\infty = S_{el} \quad (1.10)$$

In this case, we might replace L_∞ with L and we will call it unrestricted LET. Particle transport codes and Monte Carlo simulations can be used to estimate LET using its various definitions, in particular in complex geometries. An example of DNA-scale geometry is shown in Figure 1.4, where the ionization density for two different types of particle can be seen.

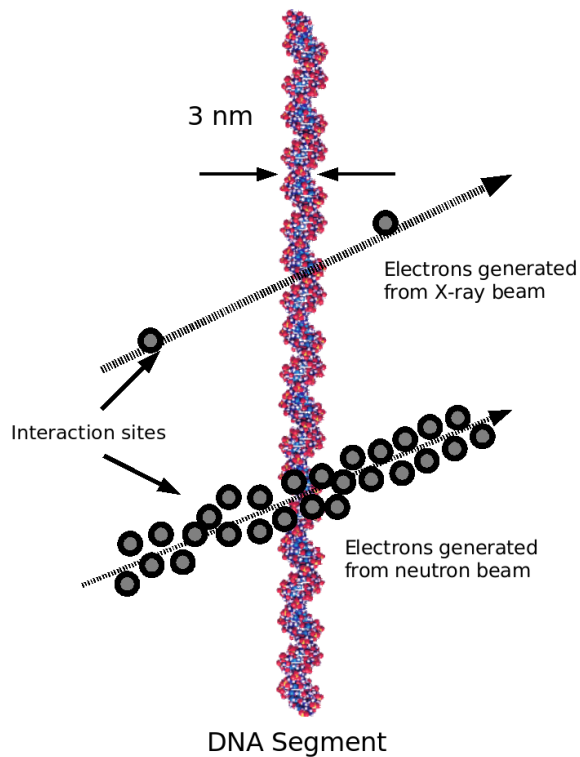


Figure 1.4: Differences between sparsely and densely ionizing particles (X-rays and carbon ions) and interactions at the DNA scale.

1.3.3. Dose averaged and track averaged LET definitions

LET is a fundamental quantity used to describe the energy deposition characteristics of ionizing radiation as it traverses a medium. Since the beam is not always mono-energetic, distributions functions are needed to describe dosimetric quantities such as LET. The distribution of LET is essential in particle therapy, since it can impact the relative biological effectiveness (RBE) and the deposition patterns of the dose. Furthermore, LET includes contributions from both primary and secondary particles produced with the beam's interactions. For example, the primary particles exhibit a well-defined LET distribution, which peaks near the Bragg peak, while the secondary particles have a broad range of LET values due to their varying masses and charges.

Because of this, the LET at a given point is often assessed using averaging techniques to provide a single representative value. The dose-averaged LET (L_d) and track-averaged LET (L_t) are the two most common methods employed for this purpose.

The choice of LET averaging method significantly influences the reported LET values and

their interpretation in radiobiological models.

If we consider an ideal sphere in the medium which is irradiated, the particle fluence Φ will describe the ratio between the number of particles dN incident on the sphere of cross sectional area dA .

Knowing this, we can define the track-averaged LET by weighting the LET of each charged particle by its fluence Φ_i (equations taken from Kalholm's paper [4]):

$$L_t = \frac{\sum_i \Phi_i \cdot L_i}{\sum_i \Phi_i}, \quad (1.11)$$

where Φ_i is the fluence of a charged particle i , and L_i is its LET. This averaging method emphasizes the LET of individual particle tracks and is particularly relevant for micro-dosimetric applications (techniques used to measure the stochastic distribution of energy deposited by radiation at microscopic sites) where particle fluence plays a critical role.

On the other hand, the dose-averaged LET accounts for the energy deposited by each particle track and is defined as:

$$L_d = \frac{\sum_i d_i \cdot L_i}{\sum_i d_i} = \frac{\sum_i \Phi_i \cdot L_i^2}{\sum_i \Phi_i \cdot L_i}, \quad (1.12)$$

where d_i is the microscopic dose given in an infinitesimally small volume contributed to by the track of a single particle, i .

Since higher LET particles deposit more energy per unit length, they contribute more significantly to L_d compared to L_t . Consequently, dose-averaged LET values tend to be higher than track-averaged LET values, as they give greater weight to high LET components in the radiation field.

The choice between L_d and L_t depends on the specific application. In clinical proton and carbon ion therapy, L_d is often preferred as it better correlates with biological effectiveness.

1.4. Radiation therapy and FLASH

The main techniques applied for cancer treatment are chemotherapy, surgery and radiotherapy. The subject of our study will be the latter, which uses radiation to obtain long-term tumor control while granting minimum toxicities to healthy tissues.

The term radiotherapy usually refers to the delivering of electrons and x-rays, while protontherapy and hadrontherapy entails the usage of heavily charged particles (protons

and carbon ions).

Radiotherapy has been used for a hundred years and is still widely used, mainly because compact linear accelerator (LINAC) can fit in most hospital rooms, unlike the cyclotrons or synchrotrons needed for proton and ion production.

That being said, proton therapy has been gaining popularity in the last decades due to its precision in sparing healthy tissues and targeting to tumors. However, both photon-based and particle-based radiotherapy continue to evolve, with significant efforts aimed at improving treatment outcomes.

There are indeed many methods to improve treatment's results and patient's experience. Intra-treatment and inter-treatment organ motion and patient's positioning errors can be mitigated using image guided and 4D treatment, dose conformity can be optimized by using IMRT (Intensity-Modulated Radiation Therapy).

An estimation or comparison of the effectiveness of the different treatments can be done thanks to the therapeutic index (TI) or therapeutic ratio (TR), that we can see in Figure 1.5. The tumor control probability is at the left of the healthy tissue complications probability, and their dose dependence is typically fitted using sigmoid curves. Larger separations are indicative of higher TRs. Ideally, normal tissue protection strategies would move the healthy tissue curve to the right without compromising tumor control by moving it to the right too, while the ideal case would see the movement of the tumor control curve to the left.

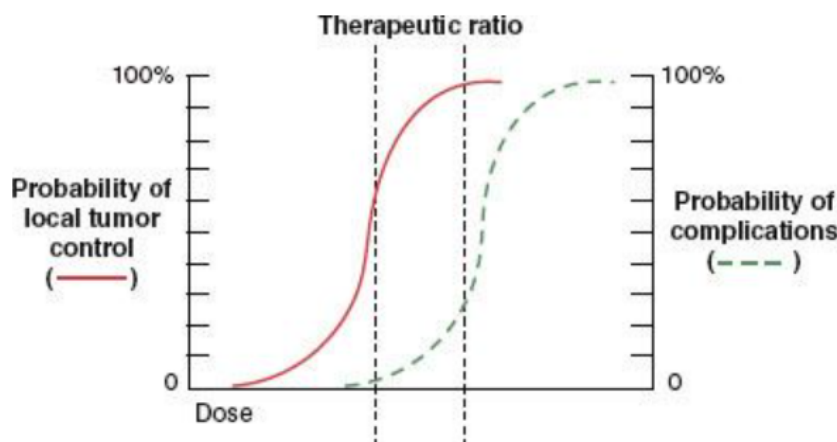


Figure 1.5: Graphical representation of therapeutic ratio.

1.5. FLASH effect and dosimetry challenges

As reviewed in F. Romano's work [5], FLASH radiotherapy (or FLASH-RT) is a promising advancement in the radiotherapy field. Discovered ten years ago through preclinical small animal experiments, it involves delivering radiation at an ultra-high dose-rate, typically exceeding 40 Gy/s, compared to the 0.1 Gy/s in conventional radiation therapy.

Both for preclinical experiments and for the development of planning and delivery tools, the dose-rate is the key parameter in FLASH. Unfortunately, in proton therapy, defining the dose-rate is not trivial. Indeed, the beam is scanned such that a voxel (volumetric pixel) receives its total dose through a series of contributions unevenly distributed over time. It is therefore not surprising that in the literature the definition used for the dose-rate varies from one publication to another [6]. The dose-rate definition should take into consideration the pulse's structure, the dose delivered per spot through pencil beam scanning and the time-related contribution to the dose seen by each voxel. Changes in these parameters can change the the dose-rate by several orders of magnitude. Even if the dose-rate is one of the key parameters for FLASH, given the current uncertainty on the time scale related to the FLASH effect itself, we cannot currently determine which dose-rate definition is the most suitable [7].

Studies ([1], [8]) suggest that FLASH radiotherapy enhances healthy tissue sparing which are also often combined with good tumor control. However, the exact mechanisms behind the so-called "FLASH effect", which provides this tissue-sparing benefit, are still not fully understood.

Several hypotheses have been proposed, linking the effect to various physical, chemical, and biological properties of tissues. These theories continue to be actively debated within the scientific community, since the study and verification of these phenomena is extremely complex: we are talking about great radiation fields and extremely small time scales.

Let us give a quick overview of FLASH biological mechanisms, as described by [9].

Early in the investigation of FLASH-RT it was suggested that a rapid depletion of oxygen within tissues occurs, leading to a temporary reduction in oxygen availability (hypoxia) that could offer sparing to normal tissues: Indeed, radiation-induced damage is dependent on oxygen and this is also known as oxygen effect. However, recent studies ([10], [11]) indicate that the magnitude of oxygen depletion induced by FLASH-RT might not be sufficient to fully justify for the biological effects observed after irradiation.

Another proposed mechanism involves the recombination and diffusion of free radicals in

tissue. The ultra-high dose-rate of FLASH-RT generates a higher density of free radicals in a very short time frame, leading to increased recombination. This process reduces the number of free radicals available to cause oxidative damage, particularly in normal tissues. To support this hypothesis, studies ([12]) have shown that the a lower concentration of oxidative markers is indeed present following FLASH compared to conventional radiotherapy.

Furthermore, in tissues such as the gut and skin, FLASH-RT has been shown to spare proliferating stem cells, which play a crucial role in tissue regeneration and repair.

Circulating blood volume may also contribute to FLASH effect: with standard dose-rates, a significant amount of blood passes through the irradiated volume over the course of treatment, leading to prolonged healthy tissue exposure and inflammation. In contrast, the ultra-fast nature of FLASH minimizes the fraction of circulating blood that is exposed, reducing the release of pro-inflammatory proteins (cytokine) and subsequent tissue damage.

Similarly, an important feature is the preservation of vascular integrity and the modulation of inflammatory responses. Conventional radiotherapy has been associated with significant damage to the endothelium (tissue that lines the interior surface of blood and lymphatic vessels). FLASH-RT, however, appears to maintain the structural integrity of blood vessels, preventing the inflammatory response that contributes to later radiation toxicity.

Recent studies have also highlighted the role of lipid peroxidation in the FLASH effect. Lipid oxidation is a process that generates damaging reactive species, and it appears to be significantly lower following FLASH-RT compared to conventional radiotherapy. Also, the regulation of iron metabolism, which influences oxidative stress through Fenton reactions, may also play a role in modulating tissue responses to FLASH.

Another factor that has emerged with FLASH-RT is an alteration of mitochondrial function in normal tissues, reducing oxidative activity and minimizing reactive oxygen species production. This metabolic shift allows normal tissues to enter a protective state. The concept of metabolic hibernation has been proposed to explain this effect: normal tissues can tolerate transient reductions in ATP (adenosine tryphosphate) production, while tumor cells struggle to maintain homeostasis under similar conditions.

A complementary hypothesis involves reverse electron flow within the mitochondrial electron transport chain. Under normal conditions, electron flow through the mitochondria results in the generation of ATP and the production of reactive oxygen species as byprod-

ucts. FLASH-RT, by delivering radiation in an extremely short time, might induce an alternative pathway for electron transport in healthy cells.

In conclusion, these mechanisms suggest that the FLASH effect has multiple causes. Further research is needed to understand the phenomena caused by FLASH delivery, to optimize the irradiation parameters for clinical applications. An overview of the possible mechanisms that account for FLASH effects can be found in Figure 1.6, reported in Limoli's study [9].

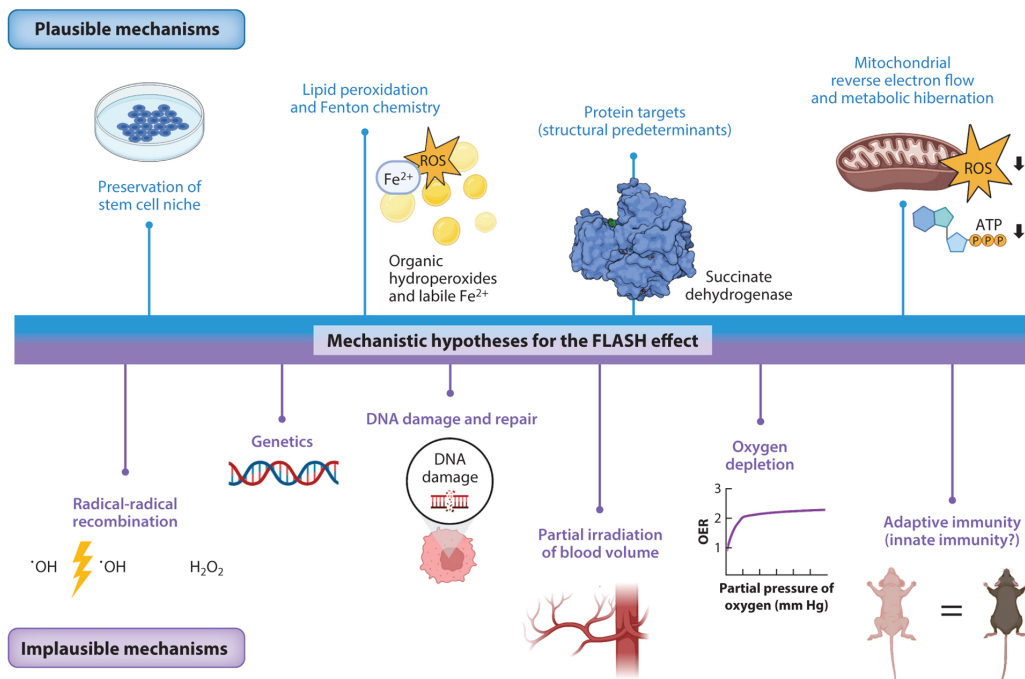


Figure 1.6: Summary of mechanistic hypothesis for the FLASH effect.

Turning now our attention towards the particle beam, many radiation sources have been explored for FLASH radiotherapy, including electrons from linear accelerators, X-rays from synchrotrons, protons from isochronous and synchrocyclotrons, and even heavier ions such as helium and carbon. Each of these sources presents unique challenges and opportunities for FLASH radiotherapy implementation. The most used particles for FLASH at the moment are electrons, since their production allow higher dose-rates.

Despite the potential advantages of FLASH radiotherapy, its clinical translation is hindered by challenges in dosimetry and beam monitoring. Traditional dosimetry techniques, designed for conventional radiation therapy, do not provide accurate measurements under ultra-high dose-rate conditions due to phenomena like saturation effects, recombination losses, etc. A crucial issue is the lack of real-time in-beam detectors (active detectors) capable of reliably monitoring dose delivery at such high dose-rates. This limitation in-

troduces uncertainties that could impact both research findings and clinical applications.

Unlike conventional radiation therapy, where dosimetry protocols are well-established (like the IAEA's TRS-398 guidelines [13]) there are no universally accepted standards for FLASH radiotherapy dosimetry. This makes it more difficult to obtain accurate and reproducible dose measurements.

Furthermore, as we have already said, FLASH and ultra-high dose-rate (UHDR) beams can come from different types of accelerating systems (see in Figure 1.7). This means that the deliverable treatment dose range, dose-rate per pulse, and repetition frequency, pulse duration etc. are characteristic of each individual irradiation facility, depending on the specific accelerator utilized. This non uniformity in beam structure for the study of FLASH further hinders dosimetry studies.

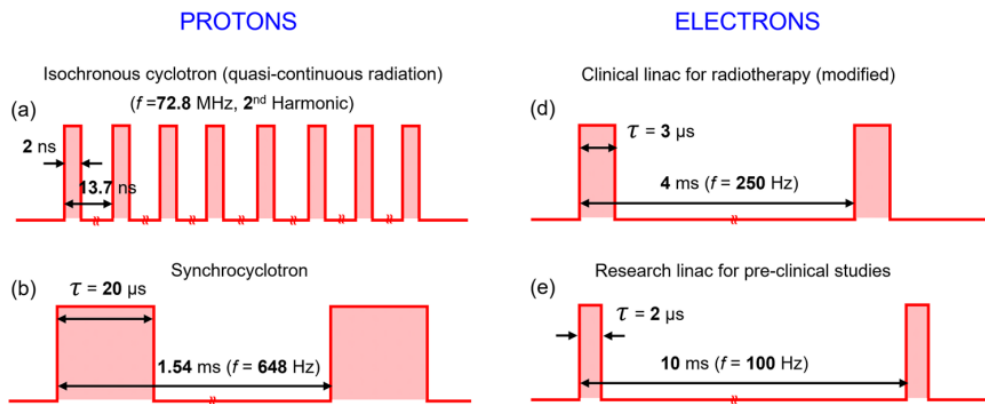


Figure 1.7: Typical temporal characteristics of different accelerators.

1.6. Radiation detection and dosimetry

1.6.1. Dosimetric quantities

Dose is the measure of the amount of exposure to radiation. There are three kinds of dose: absorbed dose is a measurable, physical quantity, while equivalent dose and effective dose are designed specifically for radiological protection purposes.

Given a volume element of mass dm , the absorbed dose is defined as

$$D = \frac{d\bar{\epsilon}}{dm} = \left[\frac{J}{kg} \right] = [\text{Gy}] \quad (1.13)$$

Where $\epsilon = R_{in} - R_{out} + \Sigma Q(J)$ is the imparted energy. R_{in} is the radiant energy incoming

into the volume, meaning the sum of energies (minus the at rest energy) of all particles, ionizing or not, entering the volume.

R_{out} is the radiant energy of all charged and uncharged ionizing particles that leave the volume (the equivalent of R_{in} , but exiting the volume).

ΣQ accounts for the conversion of mass in energy ($Q > 0$ i.e. radioactive decay) or energy in mass ($Q < 0$ i.e. pair production).

The absorbed dose is a stochastic quantity and might be subjected to large fluctuations, especially if we take into account very small volumes, in which the specific energy Z is preferred as a fundamental quantity. Thus, the absorbed dose D is the quotient of $d\bar{\epsilon}$ over dm , where $\bar{\epsilon}$ is the mean energy imparted by ionizing radiation to matter of mass dm .

Absorbed dose is not enough to describe irradiation effects on biological tissues. Indeed, for a fixed amount of absorbed dose, the effect in tissue can vary greatly. This is why we need to introduce equivalent dose as in equation 1.14.

$$H = f_q \cdot D = [Sv] \quad (1.14)$$

f_q is the quality factor and is a dimensionless multiplier related to radiation type. The equivalent dose is not a physical quantity and also it does not take into account different exposure conditions. To solve this we will use the effective dose 1.15.

$$E = \sum_T w_T \cdot H_T = [Sv] \quad (1.15)$$

Where w_T is the tissue weighting factor for tissue or organ T and H_T is the equivalent dose for tissue or organ T .

Where we expressed the equivalent dose as

$$H_T = \sum_R w_R \cdot D_{T,R} \quad (1.16)$$

w_R is the radiation weighting factor for radiation type R (dimensionless), $D_{T,R}$ is the absorbed dose in tissue or organ T due to radiation type R .

ICRP 119 [14] identifies 16 different tissues and organs, each with its own relative weight.

1.7. Important concepts of dosimetry

Dosimetry is a practice that deals with measuring and assessing ionizing radiation doses. Overall, it can ensure safety conditions in living, working, research and therapeutical environments.

Indeed, the cornerstones of radioprotection are:

- Justification: any decision that alters the radiation exposure situation should do more good than harm;
- Optimization: doses should all be kept as low as reasonably achievable, taking into account economic and societal factors;
- Dose limitation: the total dose to any individual should not exceed the appropriate limits.

Usually, as documented in publications by the International Commission of Radiological Protection [15] (ICRP), members of the public and workers can be subjected to only a very limited amount of radiation, as we can see in 1.2.

Table 1.2: These limits apply only to doses received above the normal local natural background radiation.

Type of limit	Occupational exposure	Public exposure
Effective dose	20 mSv/year	1 mSv/year
Equivalent dose to eye	20 mSv/year	15 mSv/year
Equivalent dose to skin	500 mSv/year	50 mSv/year

Limits on effective dose are designed to avoid a risk of stochastic effects. Limits on equivalent dose to an organ (eye, skin, etc.) are designed to prevent the occurrence of deterministic effects.

Stochastic effects describe probabilistic effects of radiation, occurring by chance, with their likelihood increasing with the radiation dose. Some examples could be damages to the DNA and their severity is independent of the dose. Deterministic effects occur when the radiation dose exceeds a certain threshold, causing a predictable and dose-dependent severity of damage. Some examples are burns, cataracts and sterility.

There are a few exceptions to the rules, and the reason is the justification principle: for people in need of diagnosis and cancer patients, the discovery of an underlying anatomical or functional condition or the treatment of cancer clearly justifies a greater radiation exposure.

Dose limits do not apply to medical procedures. If they did, the effectiveness of diagnosis or treatment might be reduced, doing more harm than good for the patient. This does not mean that we should deliver dose mindlessly, since we still need to follow the optimization and dose limitation principles, thus limiting damage (deterministic and stochastic effects) to healthy tissue.

The importance of dosimetry in radiotherapy, indeed, is ensuring accurate and safe delivery of therapeutic radiation, which should be as low as reasonably achievable (ALARA).

In addition to patient-specific dose measurements, dosimetry is also crucial for the verification of the radiation beam from the accelerator, or to evaluate the accuracy of other dosimeters, serving as benchmarks to ensure the treatment accuracy and consistency.

2 | Materials and methods

2.1. Dosimeters

In the next sections we will give a brief overview of the different detectors and dosimeters that we used in our experiments, following descriptions found in Knoll's book [16].

2.1.1. Ion chamber detector

Ion chambers are based on the ionization provided by charged particles moving through a gas. The ionized charges (electron/ion couples) will thus be collected thanks to an electric field and the signal will be analyzed most of the time in current mode, although pulse mode applications are common.

To make this possible, a gas whose ionization potential is lower than the incoming particle's energy is used (usually this potential is around 10-25 eV). Not all of the particles will succeed into creating pairs (some of them will just excite the medium with no ionization): the Fano factor is usually lower than 1, denoting that the statistical fluctuation correlated to the number of charges created per unit energy is lower than what predicted by a Poisson statistic.

Thus, once ions and electrons have formed, they will take part in thermal motion along with all other particles, resulting in a tendency to diffuse toward regions of lower density (a much more pronounced effect for electrons, as they have higher thermal velocities). Many types of interactions can therefore take place between electrons, ions, and neutral gas molecules. For example, there may be processes of recombination of free electrons with positive ions, meaning that the charges originally formed are lost and do not contribute to detection. This recombination phenomena (which can also happen with other particle-ion combinations) can happen either through columnar recombination (more localized and typical of high LET) or volumetric recombination.

To collect the available charges, in the region where the couples are formed, an external electric field is applied, which will catch and drag the charges towards the cathode (pos-

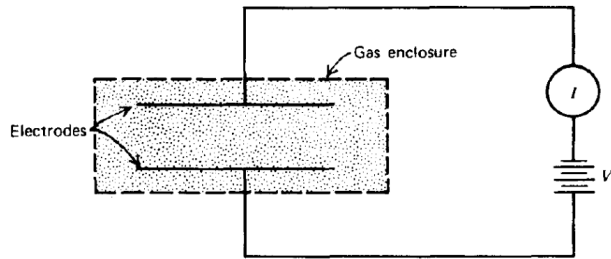


Figure 2.1: Scheme of the ion chamber.

itively charged particles) and anode (negatively charged particles), with a certain drift velocity v_d .

$$v_d = \frac{\mu \cdot \epsilon}{p} \quad (2.1)$$

where μ is the charge's mobility factor (higher for smaller particles), ϵ the electric field intensity and p is the pressure of the gas. This velocity shows a saturation behavior, as we can see in Figure 2.2.

The drift of charges will create a so called ionization current which reflects the rate of formation of electron/ion couples.

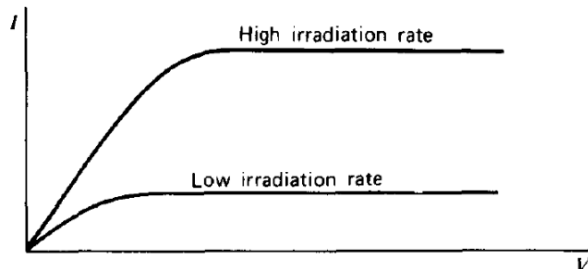


Figure 2.2: Saturation behavior of current (I) with increasing voltage (V).

By increasing the applied voltage, the resulting electric field begins to separate the ion/-electron pairs more quickly and they will move towards the electrodes with higher drift velocity, also increasing the current. At a sufficiently high applied voltage, recombination and diffusion are reduced and all charges are collected by the electrodes, reaching a saturation voltage beyond which it is no longer necessary to increase the voltage since all charges are already collected. This is precisely the voltage at which the system must operate.

Ionization chambers are the most commonly used detectors in radiotherapy for a variety of reasons: energy independence, real time measurements, ease of calibration and handling, tissue equivalence, wide measuring range and accuracy/precision. They align with international dosimetry protocols, such as those outlined by organizations like the International Atomic Energy Agency (IAEA). However, their suitability is challenged in the context of FLASH radiotherapy.

For high irradiation rates, a higher voltage will be required. Indeed, if the chamber saturates a portion of the charges recombine instead of being collected and this leads to an underestimation of the dose-rate or total dose. Furthermore, FLASH involves delivering a massive dose of radiation in a very short time (milliseconds). This causes an extremely high local density of ion pairs in the chamber, enhancing recombination and furthering the risk of dose underestimation. Indeed, in our experiments we irradiated ion chambers only in conventional mode, using them as a benchmark to compare the results of dosimeters more suited for FLASH.

In particular, the ion chambers we irradiated in our experiments were plane-parallel ionization chambers, specifically the PPC05 (by IBA Dosimetry company) and Advanced Markus (by PTW Dosimetry company) models. Their use is exclusively for conventional irradiation. Unlike cylindrical ionization chambers, plane-parallel chambers feature two parallel electrodes, one serving as the collecting electrode and the other as the guard electrode, which help ensure uniform electric fields and stable charge collection. These chambers serve as benchmarks to compare the performance of dosimeters more suited for FLASH applications.

Overall, the ion chamber is a standard detector in conventional radiation therapy but FLASH amplifies the ion recombination effect in ionization chambers by 10–40 times [17], thereby exceeding international dosimetry protocol recommendations for accurate ionization chamber application. Hence, the existing conventional ionization chamber cannot meet the measurement conditions for FLASH radiotherapy.

New models of ion chamber, like the one using ultra-thin parallel plates proposed by Gómez et al. [18], are being developed for dosimetry in FLASH-RT.

2.1.2. Diamond detector

Diamond detectors (with Ge and Si) are one of the most commonly used solid state semiconductor detectors. Semiconductor materials have a larger number of information carriers for a given incident radiation, leading to good energy resolution. In this case, the information carriers are the electron-hole pairs created along the path of a charged particle

(whether it is primary radiation or a secondary particle), analogous to the ion-electron pairs in gas detectors (see section 2.1.1), whose motion induced by the application of an electric field generates the output signal, as we can see in Figure 2.3.

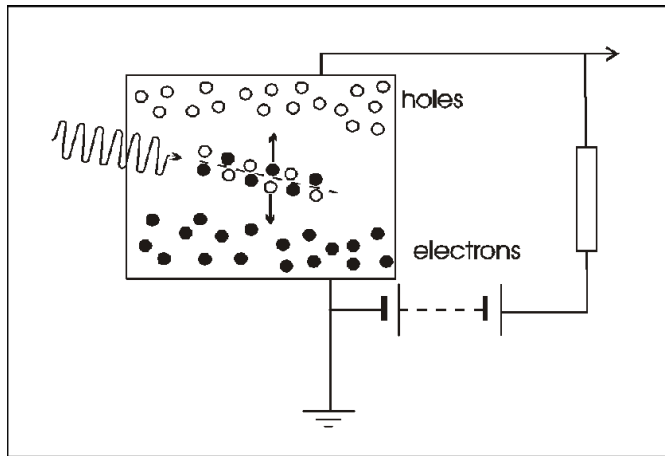


Figure 2.3: Scheme of the semiconductor detector.

The possibility of using semiconductors as detectors is based on their physical properties. In fact, the periodic crystal lattice of these materials allows for the existence of some energy bands, and the energy of each electron in the material is confined within one of these bands (figure 2.4).

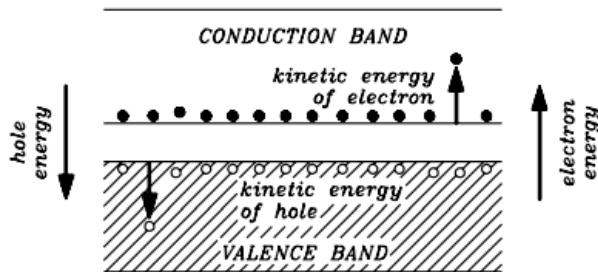


Figure 2.4: Semiconductor's band structure.

The lower-energy band, called the valence band, corresponds to electron shells bound to specific points in the lattice. The upper band, called the conduction band, contains free electrons that can move through the lattice. The two bands are separated by a gap in energy that determines whether the material is classified as an insulator (a very large energy gap) or a semiconductor (a smaller gap, on the order of electron volts).

As we have already said, after the passing of a particle through the solid state detector's active volume, electron-hole pairs are formed as the medium is ionized: the electrons gain

enough energy to overcome the gap and are promoted to the conduction band. When this happens, it will leave a hole in the valence band.

The electron is then made to move under the influence of an applied electric field, with its direction following its negative charge, while the hole moves in the opposite direction, due to its positive charge. The electron and the hole will undergo motion resulting from a combination of thermal (random) velocities and drift velocities (parallel to the direction of the field). The latter velocity is proportional to the electric field's intensity. Unlike in gas, where the mobility of electrons is higher, in a semiconductor holes and electrons have very similar mobility.

Another parallel we can trace between gas detectors (ion chamber) and semiconductors is the saturation behavior.

Indeed, at higher values of the applied field, the drift velocity reaches a saturation value. At this point, any further increase in the applied field intensity will no longer have an effect.

Thus, many semiconductors are designed to operate at field values high enough to result in saturated drift velocities. Since these velocities are on the order of 10^7 cm/s, the time required to collect charge carriers over typical detector's dimensions (fractions of a centimeter) will be on the order of nanoseconds. This makes semiconductor detectors the fastest radiation detectors in terms of response time.

The key quantity of practical interest for detectors is the average energy required by the primary charged particle to produce an electron-hole pair, known as the ionization energy, which is independent of both the energy and type of the incident radiation. This allows the number of produced electron-hole pairs to be interpreted as proportional to the energy of the incident radiation.

The most significant advantage of semiconductor detectors is their lower ionization energy compared to gas detectors. For diamond, the ionization energy is about 13 eV per electron-hole pair created, whereas the gases commonly used in ionization chamber detectors are around 30 eV per ion-electron pair.

As a result, for the same amount of energy deposited in the semiconductor volume, the released charge is greater than in gas detectors (e.g. 10 times higher), leading to lower statistical fluctuations in the number of charge carriers per pulse. This, in turn, enhances the energy resolution of the output signal.

Diamond as dosimeters are also tissue equivalent. On the other hand, the sensitivity of the diamond is strongly affected by the size of their active volume (direct proportionality).

Regardless, some prototypes of diamond Schottky diode detectors have been investigated for FLASH (as overviewed in Marinelli et al. paper [19]) and the results show dose linearity up to 20 Gy/pulse, demonstrating feasibility of diamond detector for FLASH applications.

Diamond detectors are extremely interesting for FLASH, owing to their high radiation hardness, tissue equivalence, fast response, and high volume sensitivity. Marinelli et al. study [19] shows an investigation on the properties of diamond-based detectors as dosimeter for FLASH therapy applications. Furthermore, some solid state detectors, like silicon carbide (SiC), are also candidates for FLASH dosimetry as demonstrated by Romano in his work [5].

2.1.3. Dosimetry protocol: Technical Reports Series N° 398

Ion chamber and diamond detectors can be used as dosimeters through the usage of some guidelines that help convert the detector's signal into dose. This is most often seen in everyday radiotherapy centers with ion chambers, that are the standard for radiation therapy dose calibration, as underlined in the TRS 398. In this report, ion chambers outputs are linked to the measured current or charge to some correction parameters to obtain the absorbed dose.

This protocol was used to estimate the dose measured by the various ionization chambers used throughout our work (either conventional proton or electron beams, as we will see in the result section).

The IAEA's Technical report series N°398 [13] wants to give an international code for dosimetry and can help us to convert the charge to dose in our experiments, so that ion chambers can serve as benchmark for alanine dosimetry.

Given a reference radiation quality, for example Co-60 gamma rays for proton dosimetry, we can express

$$D_{w,Q_0} = M_Q \cdot N_{D,w,Q_0} \quad (2.2)$$

Where D_{w,Q_0} is the absorbed dose to water, M_Q is the reading of the dosimeter at the quality Q (it can also be expressed in a pulse-dependent way, $M_{Q,pul}$), N_{D,w,Q_0} is a calibration factor in $\frac{Gy}{C}$ in terms of absorbed dose to water for a certain dosimeter at a reference beam quality Q_0 (see some examples in Table 2.1, as we can see in 2.1).

D_{w,Q_0} is an uncorrected dose that needs to be corrected, in the case for example of an ion

Table 2.1: Values of N_{D,w,Q_0} for different types of dosimeters.

Detector	N_{D,w,Q_0} [Gy/C]
ppc05	$1.42 \cdot 10^9$
AMn°879	$1.42 \cdot 10^8$
Diamond	$7.18 \cdot 10^9$

chamber, by some parameters depending on physical and environmental characteristics.

$$D_{corrected} = D_{w,Q_0} \cdot k_{tp} \cdot k_{s,conv} \cdot k_{pol} \cdot k_{Q,Q_0} \cdot k_{tp} \cdot k_{elec} \quad (2.3)$$

Where k_{tp} is a coefficient that takes into account the possible difference in temperature and pressure from reference conditions. $k_{s,conv}$ instead takes into account the factor to correct the response of an ionization chamber for the lack of complete charge correction. $k_{s,conv}$ in particular is tailored for conventional irradiation and it is different from $k_{s,FLASH}$. k_{pol} corrects the response of the ion chamber for a change in polarity. k_{tp} corrects for temperature and pressure and k_{elec} corrects for the electrometer reading, which we can set as one.

Up to this point, we have discussed the protocol for proton dosimetry. However, for electron beams, a different calibration approach is required. The following section outlines the specific corrections applied in electron dosimetry, particularly in determining k_{Q,Q_0} based on R_{50} , the beam quality index for electrons.

To determinate k_{Q,Q_0} , we need to find R_{50} , the half-value depth in water used as the beam quality index for electron beams. This is the depth in water at which the absorbed dose is 50% of its value at the absorbed dose maximum. If $R_{50,ion} \leq 10 \frac{g}{cm^2}$,

$$R_{50} = 1.029 \cdot R_{50,ion} - 0.06 \frac{g}{cm^2} \quad (2.4)$$

Where $R_{50,ion}$ is the half-value of the depth ionization distribution in water and is equal to

$$R_{50,ion} = R_{50,ion,pl} \cdot h_{pl} \cdot c_{pl} \quad (2.5)$$

Where $R_{50,ion,pl}$ is the half-value of the depth ionization distribution in water before the corrections given by c_{pl} , that is a material-dependent depth scaling factor for a plastic phantom, and h_{pl} , that represents the water to plastic fluence correction factor.

Another parameter to find k_{Q,Q_0} is the reference depth z_{ref} for in-phantom measurements.

It can be found by using the following equation:

$$z_{ref} = 0.6 \cdot R_{50} - 0.1 \quad (2.6)$$

From this we can obtain $z_{ref,pl}$

$$z_{ref,pl} = \frac{z_{ref}}{c_{pl} \cdot \rho} \quad (2.7)$$

where ρ is the density of the phantom.

K_{Q,Q_0} is obtained through the equation

$$K_{Q,Q_0} = a + b \cdot \exp\left(\frac{-R_{50}}{C}\right) \cdot K_{Q,e_{cal}} \quad (2.8)$$

Where, in equation 2.1.3, R_{50} comes from the percent depth dose measurement, which was performed in the solid water slabs (usually around 2 and 2.5 cm depending on the electron energy). Coefficients a, b and c come from reference[20].

2.1.4. Film dosimetry

The basis of a film dosimeter seems simple: radiation interacts with film and darkens the interaction area. The degree of darkening can be correlated with dose. However, there are many different methods used to obtain this relationship, and the accuracy of film dosimetry is sometimes slightly limited.

Let us start by describing a traditional film dosimeter, the silver bromide (AgBr) crystal. The film is made up of an emulsion ($20 \mu m$ thick) where grains of a certain compound, mainly AgBr with some AgI or AgCl, are suspended (usually over a thickness of $5 \mu m$). The base, intended to give structure to the dosimeter, is made of cellulose. The geometry is variable since it is virtually impossible to obtain uniform distribution both spatially and in size of the grains.

The effect of radiation is to transform silver from an ion to a metal, during the formation of a latent image, according to Gurney and Mott mechanism (figure 2.5): incident particles ionize AgBr, creating free electrons and holes. Electrons migrate to sensitivity specks, reducing silver ions to metallic silver, forming the latent image. Bromine atoms are released into the gelatin matrix, stabilizing the process.

Looking at the process more in detail, AgBr has a face centered cubic structure (FCC) and

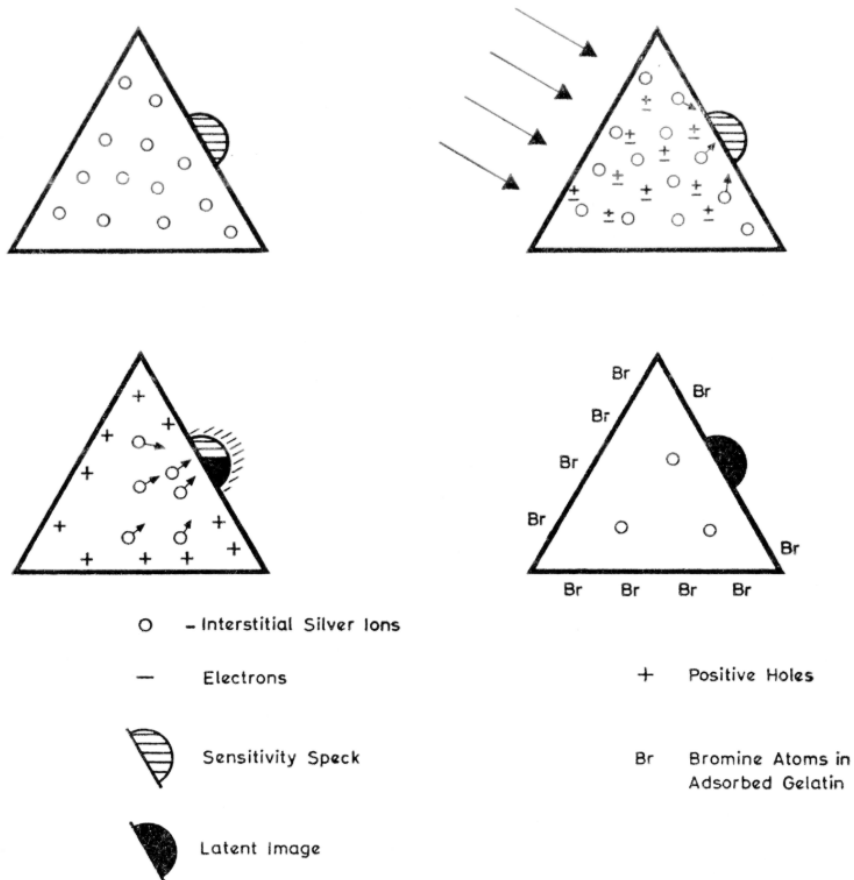


Figure 2.5: Gurney-Mott mechanism for latent-image formation.

some electrons, after interaction with radiation, get promoted to the conduction band and they are thus free to move. Defects and impurities inside the crystal act as electron traps: Ag^+ ions (which are present interstitially) combine with these electrons and they become metallic Ag. The latent image is now formed. The electrons can be de-trapped again, for example because of high temperatures or light exposure, with a fading phenomenon.

AgBr dosimeters require to be developed with a chemical bath and to be read with an optical densitometer, while more recent dosimeters, like the EBT Gafchromic, can be directly read with a computer scanner. Indeed, they do not need to be developed as darkening of the film is produced directly after irradiation. The chemical composition in the EBT is in fact different and made mainly with C, H, O, N, Li and Cl (see Figure 2.6).

Another advantage of EBT with respect to AgBr is that the latter slightly overestimated dose. Regardless, for both EBT and AgBr dosimeters, the main features of film dosimetry remain in common. Firstly, the optical density (OD), as defined in equation 2.9, slightly increases with time post exposure, as we can see in picture 2.6 taken from Dunn's article [21]. Therefore users generally wait for a fixed amount of time before scanning the

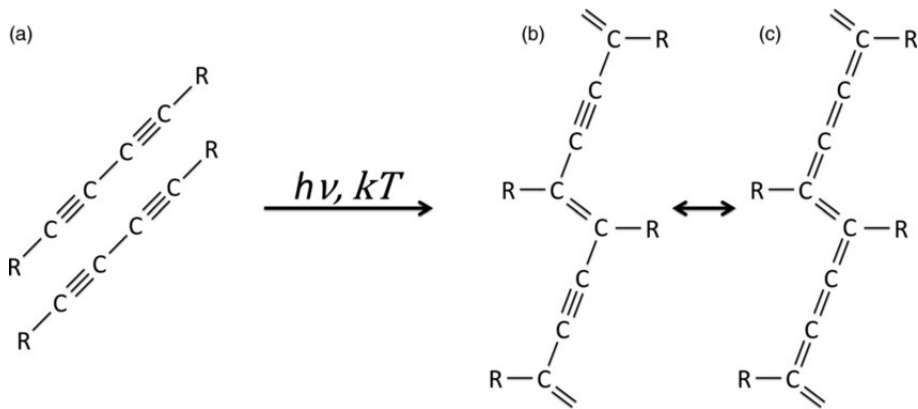


Figure 2.6: EBT active component polymerization: upon exposure to photon energy or thermal energy, the linear structure (a) undergoes polymerization, leading to the formation of cross-linked structures (b) and (c) through a resonance-stabilized process.

irradiated films (generally 24 hours).

$$OD = \log_{10} \left(\frac{I_0}{I} \right) \quad (2.9)$$

Where I_0 is the mean pixel value of the zero-dose region of interest (ROI) and I is the mean pixel value for each nonzero calibrated ROI.

Furthermore, there is a well define active range for the dosimeter, meaning a range of doses or exposure for which we can have a variable response for the dosimeter. For film dosimeters, being below the active range means dealing with an underdeveloped film, while being above means having overexposed film (the optical density is no longer changing with dose). in Figure 2.8 we can see the sensitometric curve, representing the concept we just described. In particular, the optimal condition should remain as much as possible within in the linear portion.

There are several models for EBT films: EBT4, EBT-XD with different dose ranges, in particular from 0.1-1 Gy up to 40 Gy. We used them in FLASH irradiations because of their dose-rate independence.

Radiochromic films can be used to evaluate two-dimensional dose distributions with excellent spatial resolution. Over time, the color rendering of radiochromic films changes, which significantly impacts the dose readout accuracy. All of this aside, film dosimeters have an intrinsic uncertainty that in most cases can be taken as roughly 5% [22].

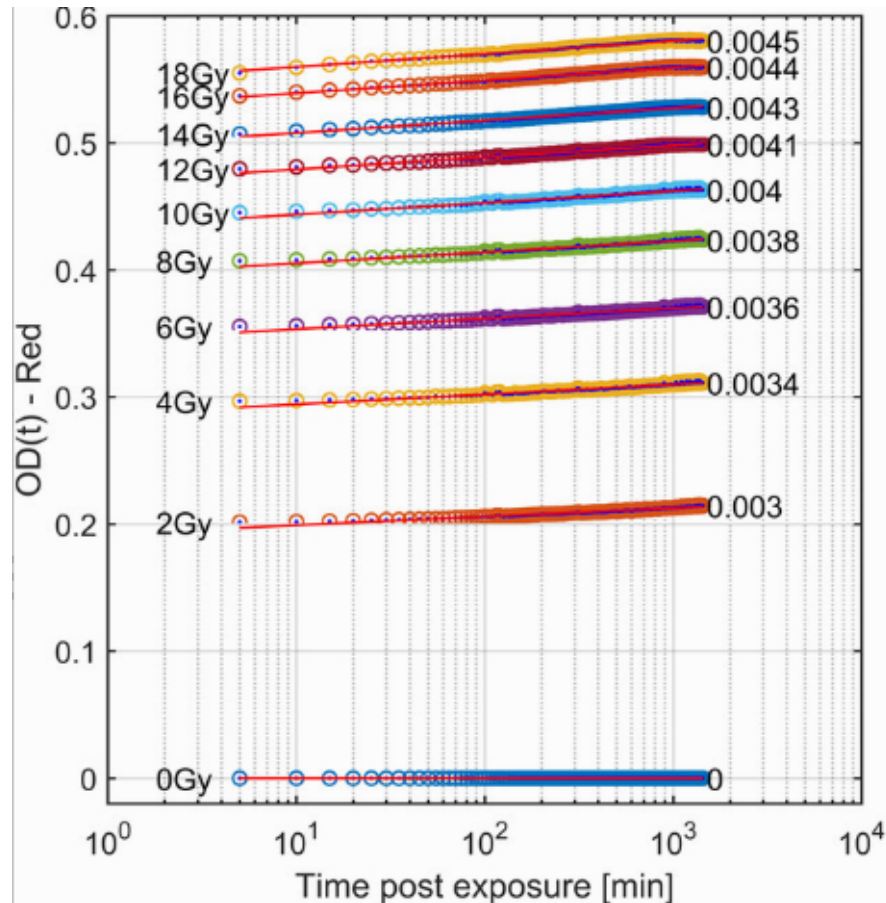


Figure 2.7: OD as a function of $\log(\text{time})$ for a period of 24 H post irradiation for doses between 0 to 18 Gy.

2.1.5. Film dosimetry protocols

The film dosimeter was used for dose verification during our study, in particular for ultra-high dose-rate electron beams.

As we have already mentioned the film, after irradiation, has a developing time. Indeed, one of our experiments focused on checking the variation of the information stored in the film with time, and different readings were taken of the film, at hours and days after irradiation. The result of this study can be seen in Figure 2.12.

IRSN has a reliable good practice for film reading, coming from Santo et al. publication [23].

Here are some of the crucial steps for film reading we have followed during our experiments.

Firstly, it is fundamental to correctly store and prepare films for irradiations. Mishandling (eg: touching the film with no gloves) and cutting the film samples with the wrong

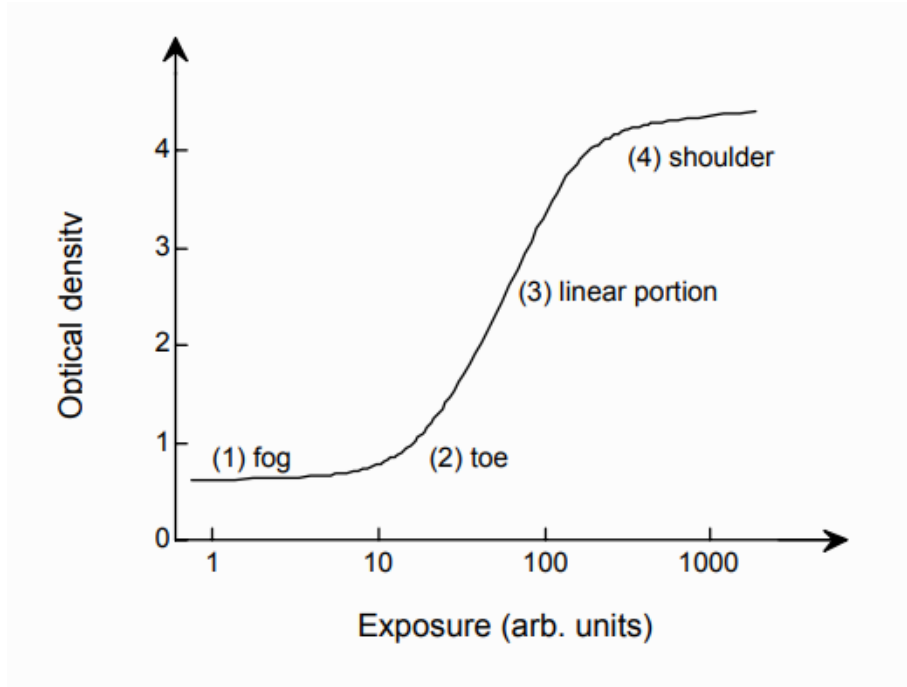


Figure 2.8: Example of a sensitometric curve for film.

technique can result in anisotropies in the dose reading. Ideally, the films should be stored for at least 24 hours before reading. Then, it is important to obtain a stable scanner. The stabilization and warm-up are obtained by doing many numerizations of a test film fixed with tape to the scanner. Each numerization is made to last 30 seconds and in between them there will be 90 seconds of waiting time. For each numerization, the mean value of red pixels is measured in a same region of interest or ROI, and the stability of this value will showcase the stability of the scanner. Usually, stabilization is obtained after around 20 numerizations, and after that we can start to analyze the films.

To read the film, the EPSON Scanner 10000XL was used to create an image of the film, and the dose information in [Gy] was obtained with the Matlab routine seen in Appendix A.1.

Here we will show, in order, the image from the scanner (Figure 2.10), the image from Matlab before the selection of the center, the image from Matlab before the selection of the range, and the resulting dose profile (Figure 2.11).

On Wednesday, April 10 2024 we irradiated films and alanine to estimate signal evolution over time. In fact, in both of the dosimeters, the stable reading of the detector comes a couple of days after irradiation. The study with alanine did not show meaningful results, but we will show here an example of the outcome of film reading taken from that experiment.

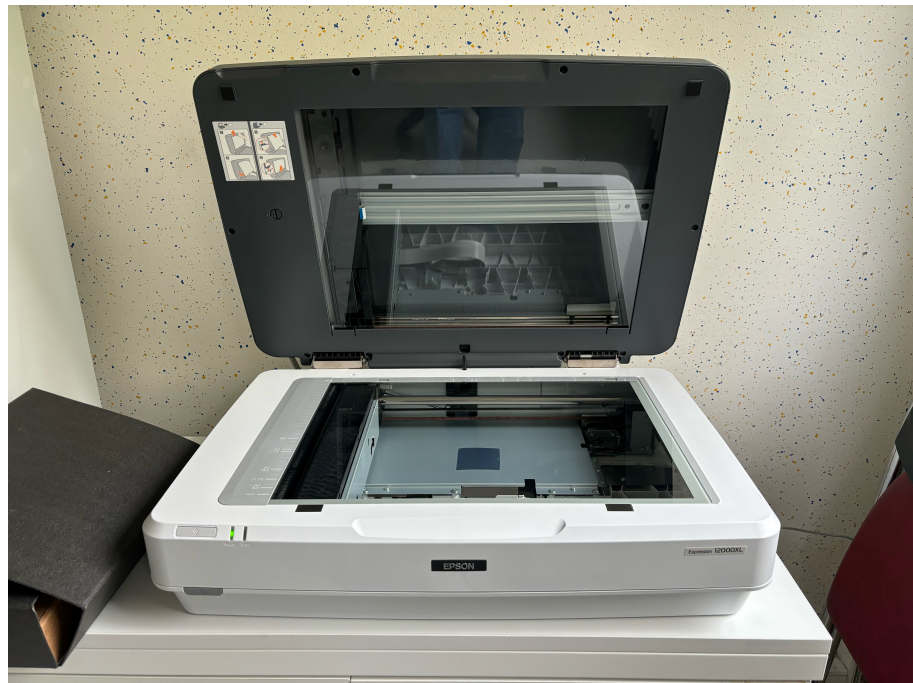


Figure 2.9: The film dosimeter placed in the EPSON scanner.



Figure 2.10: An example of what the EPSON scanner gives as a numerized result.

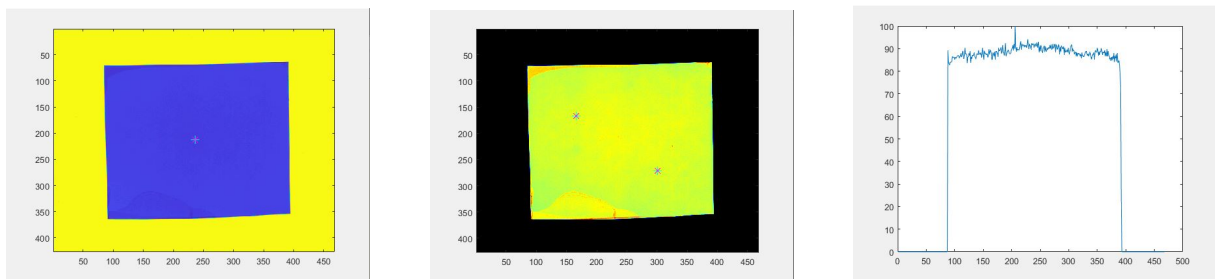


Figure 2.11: Elaboration of the film using the Matlab code.

Where in this case the dose at the selected point is 19.93 Gy and the mean dose at the plateau is 19.60 Gy.

In Figure 2.12 we can see the dose evolution over a span of six days, showing no stabilization of the films optical density. We assume the reading was not done properly, in particular subtraction by a non-irradiated film should have compensated for this effect or helped to understand the problem.

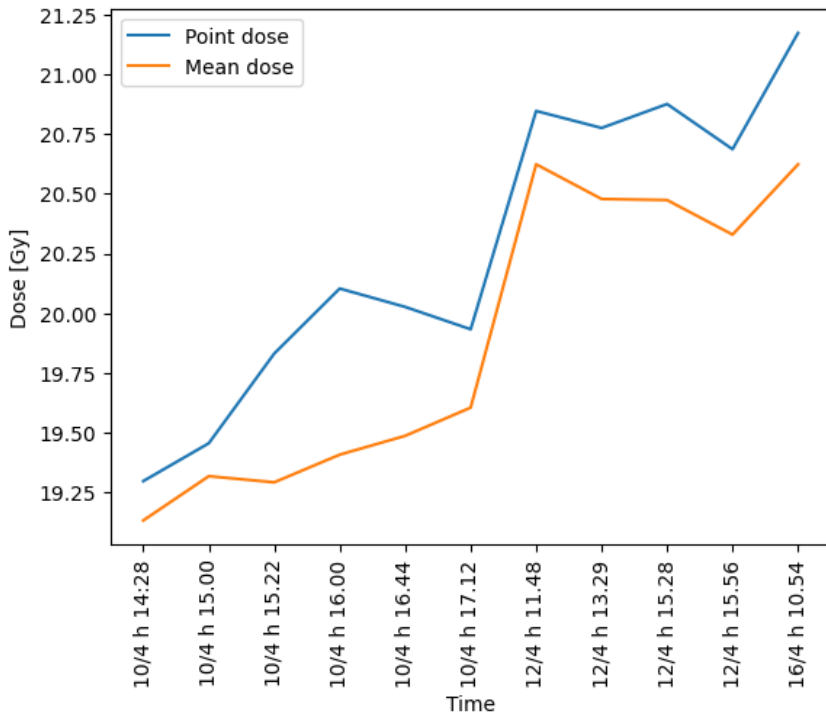


Figure 2.12: Evolution of dose over time for the film dosimeter.

Overall, the dosimeter reading of the dose can fluctuate because of different positioning of the film, of the selection of different pixels for the evaluation of point and mean dose, and because of imprecision in following the reading protocol.

2.1.6. Alanine

Alanine, also known as L- α -alanine, is a naturally occurring non-essential amino acid with the molecular formula $C_3H_7NO_2$. The notation of an α -amino acid is due to the amino group ($-NH_2$) being attached to the carbon atom adjacent to the carboxyl group ($-COOH$). Its chemical name would be 2-aminopropanoic acid and its simplicity, along with its stability under irradiation, makes alanine an excellent candidate for radiation dosimetry.

The composition of alanine dosimeters involves the mixing of a fine alanine powder with binders and stabilizing agents to form solid shapes. Binders, such as polyethylene or polystyrene, are chosen to provide mechanical integrity without hindering its response.

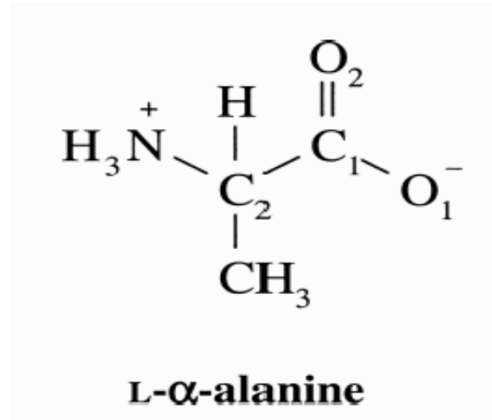


Figure 2.13: The molecular structure of alanine.

Stabilizing additives can also be included to provide further long-term stability and prevent degradation due to environmental factors.

When an alanine pellet is irradiated, the formation of stable free radicals due to the breaking of chemical bonds in the original molecule is obtained. Three main radicals are created: R1, R2 and R3, as we can see in Figure 2.14. For example, the first type of radical (R1) is formed by deamination of the alanine molecule and is the most stable and thus easily detectable radical by electron paramagnetic resonance (EPR) spectroscopy. The second type of radical (R2) is formed by deprotonation from the central carbon. For the third radical (R3), an unambiguous assignment has not been made, as it is stated in Heydari et al. paper [24].

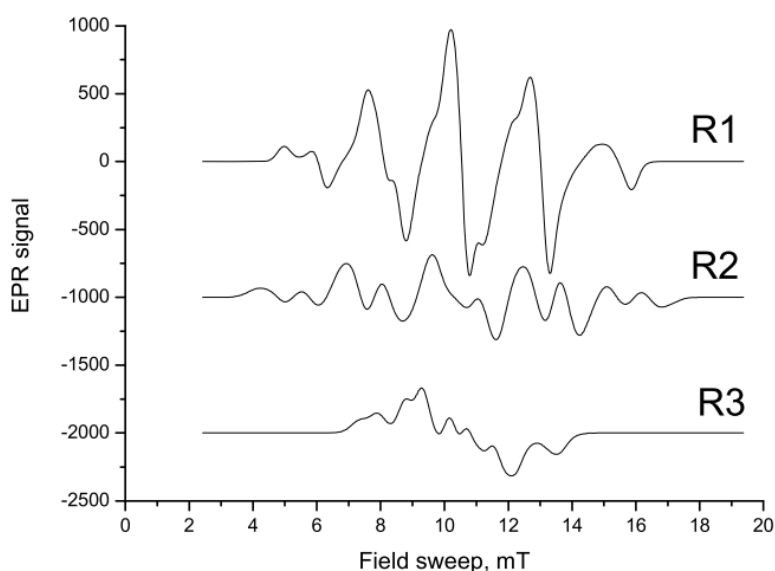


Figure 2.14: Signal of each one of the alanine radicals.

Overall, the concentration of the radicals makes quantifying the absorbed dose to the medium possible since their quantification is linearly correlated to the absorbed dose itself.

Alanine dosimeters are available in several shapes, the most common being small cylindrical pellets which are easy to handle and position, and offer good spatial discretization. To protect the dosimeters from environmental factors such as moisture, light, or oxygen, they are coated or enclosed in sealed containers. This, together with their inherent radical stability, ensures stability over time and consistent readings even after prolonged storage. The radicals formed in alanine are highly stable, showing little fading over time, which allows for delayed analysis without compromising accuracy. Furthermore, alanine exhibits minimal dependence on radiation energy across a wide range, from keV to MeV, making them suitable for both photon and electron beams in radiotherapy and industrial processes [25]. Recent studies have also highlighted the potential of alanine dosimeters in ultra-high dose-rate radiation fields, such as those encountered in FLASH radiotherapy.

As we have already said, there are large differences in the dose-rate and irradiation time between conventional and FLASH radiation therapy (for electrons, e.g., 10^2 versus 10^6 Gy/s, 0.05 Gy/s versus > 40 Gy/s, or 4 min versus < 100 ms, respectively). Existing commercial detectors barely meet the specific dosimetric requirements of the ultra-high dose-rates used in FLASH radiotherapy [17].

Alanine/electron paramagnetic resonance (EPR) is a recognized dosimetry method, with applications ranging from food irradiation, sterilization, and radiation therapy. Alanine is tissue equivalent at therapeutic beam energies, and its response is linear over a broad dose range (up to 10^5 Gy [5]), and showcases only minimal sensitivity to variations in beam energy. Furthermore, for ultra-high dose-rates like in FLASH, alanine's response is reported to be stable across dose-rates from 0.03 Gy/s up to 28 Gy/s and even as high as 3×10^{10} Gy/s [26], although a dose-rate dependency was highlighted for doses above 5 kGy [5].

Also with alanine the accuracy for low doses decreases as the signal-to-noise ratio decreases too, leading to uncertainties of several percents. In that context, reading procedures have been optimized in this low dose range to provide fast and accurate measurement. In particular, in an investigation for FLASH dosimetry Gondré et al. [27] already created and optimized measurement protocols for alanine by reducing reading time and preserving a maximum deviation to the reference of maximum 2%. Furthermore, alanine has already been used as a dosimeter for dose confirmation (together with Gafchromic film) in the first FLASH irradiation, as described in Bourhis et al. paper [8], where it correctly verified

the delivered dose.

2.2. Electron Paramagnetic Resonance

Electron paramagnetic resonance (EPR) dosimetry refers to the estimation of the dose delivered to a medium through the evaluation of relative concentrations of certain radical species created by the interaction of ionizing radiation. Radicals are molecules with unpaired electrons, giving rise to a magnetic moment, making the molecule paramagnetic and detectable through EPR.

Indeed, given an external magnetic field, these unpaired electrons will absorb an amount of energy under resonance conditions, and we will be able to see an absorption spectrum from which we can draw conclusions. The detected signal corresponds to the transition of the electron spin from its lower energy state to its higher energy state.

For more comprehensive discussions on these principles, fundamental texts such as Eaton's work [28] provide detailed explanations. In the next sections, we will outline the main physical and technological principles of EPR and EPR dosimetry.

2.2.1. The Zeeman Effect

The Zeeman effect describes the splitting of energy levels of paramagnetic species in the presence of an external magnetic field. When placed in a magnetic field, the degenerate spin states of unpaired electrons are split into different energy levels based on their magnetic moment. This splitting forms the basis for EPR measurements, as the absorption of microwave energy occurs when the energy difference between these split levels matches the energy of the applied radiation. The strength of the magnetic field influences the energy gap, allowing for resonance detection and signal analysis.

The Zeeman effect is due to the interaction of an unpaired electron in the sample with a magnetic field, B_0 . Since energies are quantized, a single unpaired electron has only two allowed energy states. It has a state of lower energy when the moment of the electron, μ , is aligned with the magnetic field and a higher energy state when μ is aligned against the magnetic field. The two states are identified by the projection of the electron spin, m_s , on the direction of the magnetic field. Because the electron is a spin 1/2 particle, the parallel state has $m_s=-1/2$ and the antiparallel state has $m_s=1/2$.

$$\Delta E = g\mu_B B_0 \Delta m_s = g\mu_B B_0 \quad (2.10)$$

Where g is the g-factor and μ_B is Bohr's magneton.

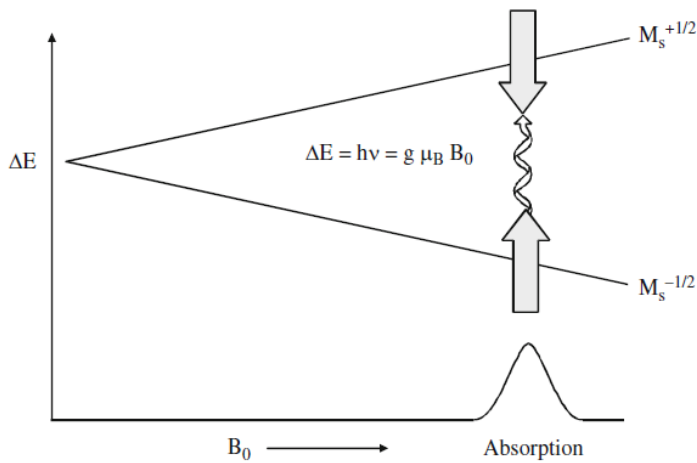


Figure 2.15: When the magnetic field is scanned, the energies of the two spin states of an unpaired electron diverge. At the magnetic field for which the energy difference between the two electron spin states is equal to $h\nu$ for the spectrometer, there is absorption of energy by the spins, which is called resonance.

The energy required to cause a transition between the two spin states is equal to the ΔE in equation 2.10. Because the energy difference between the two spin states can be varied by changing the magnetic field strength, there are two approaches:

- The magnetic field B_0 is constant while the frequency of the electromagnetic radiation is scanned;
- The electromagnetic radiation frequency ν is held constant while the magnetic field is scanned like in Figure 2.15.

Because of difficulties in scanning microwave frequencies and because of the use of a resonant cavity for signal detection, most EPR spectrometers operate at constant microwave frequency and scan the magnetic field.

The field for resonance is the magnetic field that “tunes” the two spin states such that the energy difference matches the energy of the applied radiation. It is not a unique “fingerprint” for identification of a compound because spectra can be acquired at different microwave frequencies. Compound because spectra can be acquired at different microwave frequencies. Indeed the g-factor, described in equation 2.11 is a better way to characterize

signals since it is independent from the microwave frequency.

$$g = \frac{h\nu}{\mu_B B_0} \quad (2.11)$$

The g-factor helps to distinguish and identify types of samples. For example, carbon-centered radicals have g close to the “free electron value,” which is 2.0023.

2.2.2. Hyperfine Interactions

Hyperfine interactions refer to the coupling between the magnetic moment of the electron and the nuclear magnetic moment of nearby nuclei. This interaction causes further splitting of the EPR signal into multiple sub-levels, producing a complex pattern that reflects the local magnetic environment around the unpaired electron. The number and intensity of hyperfine lines provide detailed information about the electronic structure and surrounding atoms, making it a crucial factor in EPR interpretation.

The nuclei of the atoms in a molecule or complex often have magnetic moments, which produce a local magnetic field, B_I : this magnetic field opposes or adds to the magnetic field from the laboratory magnet. The interaction between the electron and the nuclei is called the hyperfine interaction. When B_I adds to the magnetic field, less magnetic field is needed from the laboratory magnet and therefore the field for resonance is lowered by an amount equal to B_I ’s intensity. The opposite is true when B_I opposes the laboratory field.

For an electron spin interacting with a spin 1/2 nucleus (such as hydrogen), the EPR absorption signal splits into two signals that are each B_I away from the original signal. The hyperfine splitting constant, a_H , is equal to the spacing between the two lines, which is $2B_I$ (see Figure 2.16).

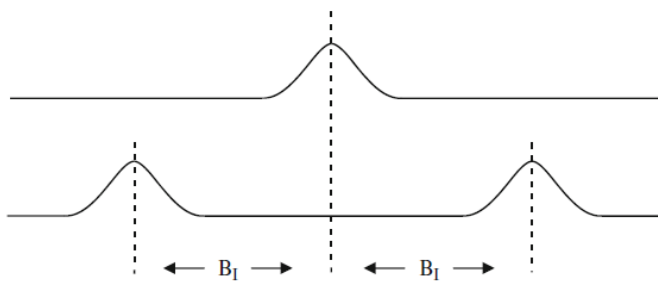


Figure 2.16: Splitting of an EPR signal due to the local field of a neighboring spin = 1/2 nucleus

For a number n of nuclei with spin $1/2$, there are 2^n EPR signals, provided that the splitting is large relative to the line width.

The general rule is that the number of hyperfine lines is equal to $2nI + 1$ where n is the number of nuclei and I is the nuclear spin.

Hyperfine splittings can be very useful in identifying radical species: ^{14}N has $I = 1$, so coupling to one nitrogen gives three lines with equal intensity. Mn has $I = 5/2$, so coupling to one manganese ion gives six hyperfine lines.

The magnitude of B_I , and hence the splitting, depends on the type of nucleus, as well as the electron spin density at that nucleus.

2.2.3. EPR spectrometer

Let us give an overview of a simplified version of an EPR spectrometer. It consists of four main components: the electromagnetic wave source, the electromagnet, the resonator, and the detection system.

The electromagnetic wave source is provided by a microwave bridge, which consists of the microwave radiation generator, the detector, the reference arm, the circulator, and the attenuator. The electromagnetic radiation can be generated by a Gunn diode, a device that can create microwave frequencies without the need to use a p-n junction. A waveguide directs the microwaves to the sample, which is located in the resonant cavity inside a glass tube. The most commonly used microwave frequency is 9.5 GHz (X-band). The microwave radiation power can be adjusted using the attenuator.

Now let us look into the electromagnet: it produces a strong, static, and stable magnetic field, which confines the sample. This is necessary for the degeneracy of the electron spin states.

Then the resonator, which is one of the most important elements of the EPR spectrometer since it contains the sample being studied. The resonator (or resonant cavity) stores the energy of the incident wave, which can be absorbed by the sample in resonance and give us the signal.

To amplify and eliminate disturbances in the measured signal, the applied magnetic field is modulated by making it oscillate with a small amplitude relative to the width of the absorption lines. This modulation, called phase-sensitive detection, is made possible by the integration of small coils (Helmholtz coils), placed on both sides of the resonant cavity.

Now that we have seen the physical components of the spectrometer, we will discuss the

acquisition parameters that can influence the shape of the spectrum as well as the signal-to-noise ratio. The optimization of these parameters is fundamental for a reproducible and accurate reading of the signal, and we analyzed them in section 3.1.

Starting off with microwave power, it directly affects the intensity of the measured EPR signals. In the absence of saturation phenomena, the intensity of the EPR signal is directly proportional to the intensity of the oscillating magnetic field, and therefore to the square root of the microwave power, as one can see in eq. 2.12.

$$\text{Intensity} = \frac{1}{\sqrt{mWPower}} \quad (2.12)$$

At higher power levels the signal does not follow the behavior described in the above equation anymore and grows more slowly or even diminishes: this behavior is called saturation (Figure 3.1) and it must be avoided.

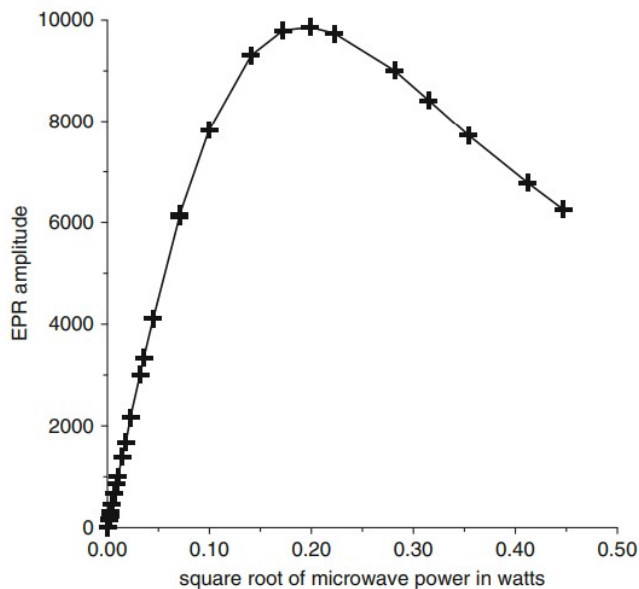


Figure 2.17: Example of saturation behavior.

It is very common to observe the saturation phenomenon of the signal when increasing the microwave radiation power. In general, for low microwave power levels, the signal amplitude increases linearly with the square root of the power. However, when relaxation processes can no longer repopulate the lower energy levels, the linear relationship no longer holds, and saturation is reached. When the electron spin-lattice relaxation time is long, the populations of the spin states equalize, and since absorption depends on the population difference between these energy levels, a decrease in this difference results in a decrease in absorption. Putting these concept into practice, to avoid operating the

spectrometer in saturation condition we created a Python script (see Appendix A.2) to check the optimization of power selection, as we see in section 3.1.2.

Another parameter to analyze is the amplitude modulation. Increasing the amplitude modulation enhances the signal intensity and therefore improves the signal-to-noise ratio. However, if the modulation amplitude exceeds the separation in magnetic field between two closely spaced spectral lines, the resulting spectrum will be distorted, making it impossible to distinguish them. This can also lead to a decrease in signal intensity.

Many EPR spectrometer's software features can help us to customize the number of acquisitions and their duration. Increasing the number of acquisitions, or the number of scans, improves the signal-to-noise ratio but requires obviously more time. The signal is directly proportional to the number of acquisitions, n , whereas noise varies as \sqrt{n} . As a result, the signal-to-noise ratio also varies as \sqrt{n} . Instead of varying the number of scans, one could change the acquisition time too.

It is also important to note that the mass, size, shape, and orientation of the sample within the cavity will influence the appearance of the obtained spectrum. We will take a look on how to estimate these effects in the section 2.2.5.

2.2.4. EPR dosimetry

EPR spectroscopy dosimetry is based on the quantification of paramagnetic species generated during irradiation by ionizing radiation. The concentration of the resulting paramagnetic entities is proportional to the dose and to the intensity of the EPR signal. This means that the number of paramagnetic entities and the dose will in turn be directly proportional. For signal we can either evaluate the area under the absorption peak curve, or the peak-to-peak amplitude of the derivative of the absorption spectrum.

Usually there are two methods for quantifying the dose received by a sample. The first and primary method, which is the one we will use in this work, involves establishing a calibration curve by irradiating samples the same characteristics (e.g: may alanine pellets) with different doses while ensuring that the same acquisition parameters are kept the same. The second method, known as the "addition method" consists of re-irradiating the sample with successive known doses while measuring it with the EPR spectrometer between each added dose. This generates a dose-response curve specific to the sample and is more precise, but it is also destructive and requires a significantly longer irradiation and analysis time.

For what concerns the EPR signal it is not the position, but the size of the signal that is

important for the measurement of the concentration of the species in the sample. The size of a signal is defined as the integrated intensity, meaning the area beneath the absorption curve, and that is proportional to the concentration of unpaired electrons in the sample, as we have already explained.

EPR spectra are typically displayed as the first derivative of the absorption signal rather than the absorption signal itself (bell-shaped). The reason for this is that we use a phase-sensitive detection, which measures how much the signal changes as the field is modulated. The larger the change in absorption across the modulation range, the stronger the resulting detected signal. Hence, what is observed and plotted is the rate of change of the absorption with respect to the magnetic field, meaning the first derivative of the absorption curve. This approach highlights transitions and spectral features more clearly than the raw absorption signal and significantly improves the ability to detect subtle features in the spectrum. This signal processing allows, on the one hand, to eliminate parasitic signals that are insensitive to the magnetic field in the cavity and, on the other hand, to improve the signal-to-noise ratio. The phase-sensitive detector, or lock-in amplifier, plays indeed a crucial role in the detection scheme by comparing the modulated EPR signal with a reference signal that shares the same frequency and phase as the modulation.

The lock-in amplifier is sensitive only to signals that match the reference signal's frequency and phase, effectively suppressing noise and interference. To further enhance sensitivity, the use of a time constant in the detector can help filter out high-frequency noise. However, we need to keep in mind that the effectiveness of phase-sensitive detection (and overall EPR spectrometer utilization) depends on careful selection of the modulation amplitude, frequency, and time constant. Poor choices in any of these parameters can distort the EPR signals, complicating the interpretation of the results or even nullifying the reading.

In particular, the measurement will be accurate if it can be thought of as free from systematic errors, while it can be defined as precise if the random errors are small. Precision (reproducibility) is a quality associated with the spread of data obtained in repetitions of an experiment and is usually stated in terms of the standard deviation. The importance of having reproducibility is evident in the creation of calibration curves. On the other hand, precision is associated with a small standard deviation (for example lower than 5%).

Usually EPR dosimeters are affected by random fluctuations in instrumental behavior and ambient conditions. Especially low doses show low reproducibility, as it was shown in alanine. This is due to the combined effect of a low signal with instrument noise, variation in background signal (the "zero dose" spectra can superimpose to meaningful), and signal

anisotropy, as underlined by Nagy's study [29]. Accuracy of a measurements expresses how close the expectation value is to the true value. In relative dosimetry, such as with EPR dosimetry, the accuracy is not determined by the single EPR experiments but by the correctness of the absolute dosimetry in the calibration routine.

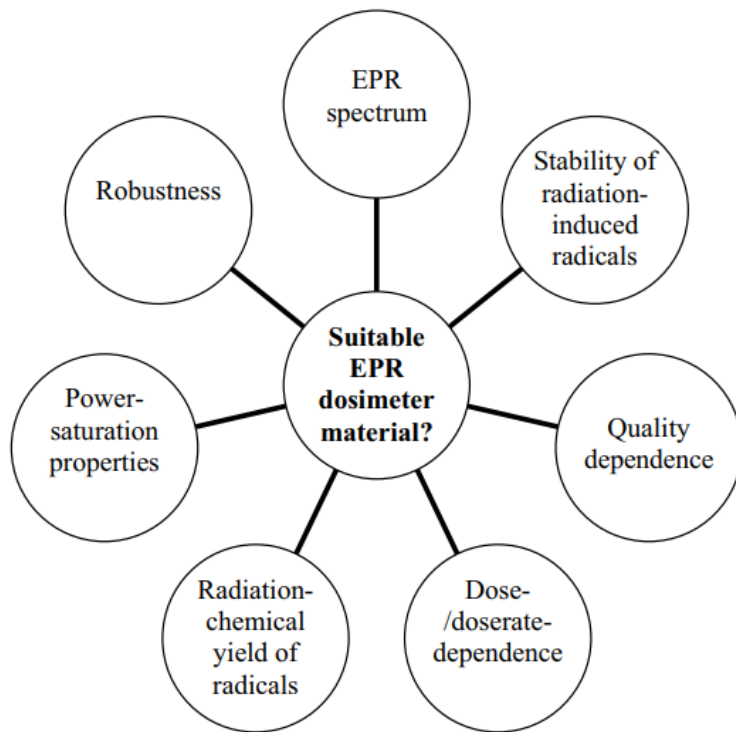


Figure 2.18: Criteria for the evaluation of an EPR dosimeter material.

EPR dosimetry is only as effective as the choice of the irradiated material is. As we can see in Figure 2.18, a lot of features are important for dosimeter material's purpose.

An EPR dosimeter must have good dose sensitivity across the range of doses it needs to measure. Ideally, the dosimeter should showcase a linear relationship between the output signal and the dose. This means that dose sensitivity remains constant and simplifies calibration and dose determination.

The sensitivity of an EPR dosimeter can be defined as the initial slope of the dose-response curve, which depends on both the radiation-chemical yield of radicals and the width of the EPR signal. The radiation-chemical yield, G , represents the number of species produced, destroyed, or altered given a quantized amount of absorbed energy, for example 100 eV.

A high radiation-chemical yield is desirable for dosimeter materials, though it is not the sole determinant of high sensitivity. Alanine has a high radiation-chemical yield, with

values of $G = 4.0$ per 100 eV. However, the signal intensity in alanine is distributed across multiple lines: multiple radicals are produced after irradiation.

The reading from an EPR dosimeter should ideally remain unaffected by the rate at which radiation is delivered. Generally, there is no specified limitation for low dose-rate measurements in EPR dosimetry, since fading is assumed to be insignificant during the relatively short exposure periods. We on the other hand are more interested in high dose-rate irradiations. Indeed, dose-rate independence might eventually reach a threshold where charged particle tracks are produced in such proximity in space and time that interactions between electron-hole pairs or free radicals from different tracks could promote reactions like radical recombination. As far as we know, no extensive studies have been conducted to investigate dose-rate effects on commonly used EPR dosimeters. To our knowledge, no comprehensive studies have systematically investigated dose-rate effects on commonly used EPR dosimeters at ultra-high dose-rates. However, some studies (e.g. Gondré et al. [27], Waligórski et al. [30]) suggest that radical recombination may influence dosimetric accuracy at extreme dose-rates.

EPR dosimeters can be ideally used over and over again, but to make this possible they must be protected from environmental factors that can alter them. Common factors that may influence this include humidity, and temperature. After irradiation, the EPR signal may be unstable over time, once again depending on the external conditions listed above. This is true also for the EPR machine itself. To minimize these uncertainties, consistent laboratory practices are crucial. Proper standardization allows for the application of corrections to compensate for signal variations.

Regardless, even if we respect the defined handling procedures, EPR readings over time may result in a reduction of concentration of the monitored radicals. This is called fading. Fading can be influenced by environmental factors, such as light exposure, temperature, and humidity during storage. Other contributing factors include radiation dose and irradiation temperature. In between our experiments, one tailored to fading was performed: an irradiated pellet was measured continuously from the moment right after irradiation up to many days later. The analysis of the results showed no meaningful variation and so we decided not to report it in this work: the time-frame of the internship was too short to see any significant fading with our configuration.

Lastly, the dosimeter is not of the same material as the medium, so the reactions happening in both media (absorption, scattering, etc.) might develop in different ways. The energy dependence of a dosimeter is defined as the dependence of the dosimeter reading per unit of dose to water on the photon or electron-beam energy.

Another dependence is that of the dosimeter reading per unit of dose deposited in the dosimeter itself, the LET dependence. This can arise from changes in the radiation-induced chemical yield depending on radiation energy, such as variations in ion or radical recombination. In EPR dosimeters, the spatial closeness of radicals may potentially affect the linewidth and alter the peak-to-peak amplitude of the first-derivative EPR spectrum due to enhanced relaxation.

To review and conclude, alanine/EPR dosimetry can offer itself as a reference dosimeter in radiotherapy, meaning a dosimeter that can be used as benchmark to calibrate other instruments. In his paper, Arias [31] gives us an interesting overview of the properties that alanine hold that could make this possible:

- Stability of the radiation induced radicals, which provides the required repeatability in the ESR signal acquisition process;
- Linear dose response over a wide range of radiation doses, which simplifies calibration;
- Small energy dependence for the measurement of absorbed dose to water (negligible from 6 to 25 MV beam qualities, but not for low energy protons);
- High radiation yield factor, representing the number of radicals generated per unit of absorbed energy. This allows the use of dosimeters with a small physical size, adequate for small field dosimetry;
- The non-destructiveness of the ESR readout process, which enables the performance of cumulative studies.

As downside, the signal to noise ratio of the alanine dosimeters drops in the therapeutic dose range (for example a few Grays), and achieving the low uncertainty allowed in radiotherapy dosimetry (for example 5% deviation from the prescribed dose, as IAEA requirements state [32]) requires to raise the sensitivity requirements of the spectrometer and hold control of every influential quantity involved in the alanine/ESR dosimetry. In our work, precisely in section 3.1, we will try to gauge some of these effects. Regardless, several metrology institutes nowadays use alanine/EPR dosimetry as secondary standard in the therapeutic dose range in National Physics Laboratory, NPL (U.K.), National Institute of Standards and Technology, NIST (U.S.A.), Physikalisch-Technische Bunde-sanstalt, PTB (Germany), and many more.

2.2.5. Alanine dosimetry protocols

In the accelerator room, for each experiment we have performed, alanine irradiation was followed by an irradiation of an ion chamber, that served as a reference for dose estimation (this is only valid for conventional dose-rates).

Let us now move from the gantry to the EPR spectrometer room, used for measuring the alanine pellet's spectra. This room must be kept at constant temperature through an air conditioning unit (check section 3.1.4 to see the effects of temperature variation).

It is good practice to weigh the alanine pellets using a precision scale to evaluate the uncertainty due to weight non uniformity.

From the weighting procedure we can infer a coefficient of variation of 0.22 % among 10 pellets randomly selected from our batch. The variation in weight is small enough that we hypothesize that it does not impact the results. Because of this we chose to not repeat this weighing procedure for all the pellets used in our experiments. On the other hand, we need to be mindful that humidity and wetting of the pellet might effect the weight of the pellet. This is why we need to use gloves while handling alanine and most importantly why we specifically developed a waterproofing technique for irradiations in water (such as in the Bragg peak experiments we did, described in section 3.3.3).

In order to measure the pellet's signal from the EPR machine the protocol we used is as follows:

- Check the cavity conditions by making sure that the height of the pellet coincides with the center of the cavity. This can be done with the support offered by Bruker which simulates the cavity itself;
- Check that the cavity is clean;
- Choose a glass tube-holder of the right size. A tube with a hole on the bottom will permit faster removal and insertion for the pellet;
- Create a recipe after checking the saturation power. In this case, the saturation power was found manually by doing measurements at different mW and seeing when the peaks stop increasing in height: that is the saturation condition. We also created a Python script (see Appendix A.2) to make the measurement quicker;
- Start the measurement and take the internal marker signal. This is needed to check the stability of the signal itself;
- Measure the temperature of the cavity during the acquisition of spectra;

- If interested in reproducibility evaluation, instead of using accumulations do 10 single measurement, each time extracting and re-inserting the alanine from the tube: this will take into account the geometrical uncertainties;
- Every time a new EPR peak is formed, note the value of the amplitude. If one or two of the measurement have too high or low values, redo them or remove the outliers. The objective is to keep the standard deviation for a single pellet lower than 2-3 % in the considered dose-range.

2.2.6. Data analysis and signal manipulation for alanine dosimetry

The precise quantification of the dose response in alanine dosimetry requires a rigorous approach to data processing, ensuring reproducibility and minimizing uncertainties. The following section details the various methodologies employed in the analysis of Electron Paramagnetic Resonance (EPR) signal data, covering aspects such as normalization, reproducibility, uncertainty propagation, baseline correction, calibration, and signal stability.

Starting from normalization of the EPR signal, this crucial step is used to correct for variations due to instrumental fluctuations, environmental conditions, and sample positioning inconsistencies. The raw intensity of the alanine signal is normalized against a stable reference signal to ensure the comparability of different measurements. The normalization factor is defined as:

$$I_{norm} = \frac{I_{meas}}{I_{ref}} \quad (2.13)$$

where I_{meas} is the measured EPR signal intensity and I_{ref} is the reference signal obtained from a standard alanine sample irradiated under well-characterized conditions. The signal intensities are measured in [amp]. This normalization ensures the elimination of systematic errors arising from detector sensitivity fluctuations, humidity effects, and spectrometer drift over time. Additionally, to further refine normalization, a background correction step is incorporated. Indeed, EPR spectra often contain background signals due to environmental noise, spectrometer imperfections, or contamination in alanine samples. To enhance signal clarity, a multi-step baseline correction algorithm is applied. The raw signal intensity is adjusted using:

$$I_{corr} = I_{raw} - I_{bg} \quad (2.14)$$

where I_{raw} is the uncorrected signal intensity and I_{bg} is the estimated baseline noise. Baseline subtraction is performed using polynomial fitting techniques to account for slowly varying background trends in the spectrum. In the normalization procedure, the background signal is subtracted before as follows and the corrected intensity is calculated as:

$$I_{norm} = \frac{I_{meas} - I_{bg}}{I_{ref} - I_{bg}} \quad (2.15)$$

where I_{bg} is the baseline noise measured from non-irradiated alanine samples. This method improves signal clarity and ensures high reproducibility of dose-response relationships. Another uncertainty to estimate is the reproducibility of alanine dosimetry, and it is evaluated through multiple irradiations and independent signal acquisitions under identical conditions. The consistency of the measured EPR signals is quantified using the standard deviation (σ) of repeated measurements:

$$\sigma = \sqrt{\frac{1}{N} \sum_{i=1}^N (I_i - \bar{I})^2} \quad (2.16)$$

where N is the number of independent measurements, I_i is the signal intensity of the i -th sample, and \bar{I} is the mean intensity. A low σ value indicates high measurement consistency and precision, which is crucial for robust dose determination. In addition to standard deviation, the coefficient of variation (CV) is computed to assess relative dispersion:

$$CV = \frac{\sigma}{\bar{I}} \times 100\% \quad (2.17)$$

This metric provides a percentage-based measure of reproducibility and allows direct comparison between different experimental setups and dose levels. In this thesis, CV is mostly used to check the stability of the internal marker and acceptable CV results usually lay under 1%.

Since uncertainties in dose estimation arise from multiple sources, including measurement noise, calibration factors, and environmental variations. The total uncertainty δD in dose estimation is determined using standard error propagation techniques:

$$\delta D = \sqrt{\left(\frac{\partial D}{\partial I} \delta I\right)^2 + \left(\frac{\partial D}{\partial k} \delta k\right)^2} \quad (2.18)$$

where δI is the uncertainty in the measured EPR signal intensity and δk is the uncertainty

in the calibration factor. The impact of these uncertainties on final dose calculations is systematically evaluated to ensure accurate uncertainty quantification.

Other interesting insight can be given by the relative standard deviation (RSD), an important measure for assessing the variability of the EPR signal in relation to its mean value. It provides a normalized measure of dispersion and is especially useful for comparing the precision of different data sets. The RSD is defined as:

$$RSD = \frac{\sigma}{\bar{I}} \times 100\% \quad (2.19)$$

where σ is the standard deviation of the signal intensity, and \bar{I} is the mean intensity. A low RSD value indicates high precision in the EPR signal measurements, confirming that fluctuations in the measured signal are minimal. To further assess errors, Monte Carlo simulations are employed to model potential variations in measurement conditions and estimate the confidence intervals of the dose-response curve.

Using the have background corrected and normalized data, the relationship between the alanine EPR signal intensity and absorbed dose is established through calibration using known irradiation doses. A linear regression model, $y = ax + b$, is applied to the calibration data, and the fit becomes $I = aD + b$, where D is the absorbed dose, and a and b are fitting parameters obtained via least-squares regression. The goodness of fit is evaluated using the coefficient of determination (R^2), and deviations from linearity are examined to ensure reliable dose calibration. The calibration curve is validated by comparing measured signals from test samples against predicted values. Systematic deviations from linearity, if observed, are corrected by introducing polynomial terms in the regression model.

These data analysis techniques ensure robust and reliable dosimetric measurements for ultra-high dose-rate radiation therapy applications, contributing to the standardization of alanine/EPR dosimetry in FLASH radiotherapy.

2.2.7. Statistical analysis and Monte Carlo method

For sections like 3.2, where we need to compare different calibration curves, it was fundamental to develop a method to provide an estimate of statistical compatibility of the curves analyses. For this reason, we developed an ad-hoc Monte Carlo boot-strap method, that will be described below.

To compare the data to the linear model we use the R^2 factor. The calibration curve for phantom irradiation shows a $R^2=0.9999$, while the calibration curve for water irradiation

is $R^2=0.9999$. To compare the two previous calibration curves, we have created ad-hoc a Monte Carlo method to compute the distributions of the parameters of the two fit functions of the two curves. As mentioned before, the calibration curve has the form of the first degree polynomial $y = ax + b$, giving two parameters to evaluate for each curve. During the Monte Carlo simulation we extract 1000 mock data points from a normal distribution, where the mean μ is the experimental data point (normalized amplitude) and the σ its uncertainty (σ_{rep}). Then we have fit each set of these mock data points with a first degree polynomial of their own, using the `curve_fit` function of the SciPy package [33]. Each fit yields a different set of parameters a and b . For each pair of mock calibration curves (e.g. one for phantom data points and one from water) we subtract the correspondent slope and intercept parameters, creating the bootstrap distributions Δa^* and Δb^* . These differences are normally distributed random variables, and will be used to construct confidence intervals for the differences in slope and intercept. In practice, given a confidence level that we will set to $\alpha = 0.95$ (the higher is α , the more strict will be the evaluation), the confidence interval of each distribution corresponds to the $\frac{\alpha}{2} \cdot 100th$ and the $(1 - \frac{\alpha}{2}) \cdot 100th$ percentiles. If the confidence interval built in this way includes the zero, there is no significant difference between the slopes (or the intercepts at the chosen confidence level). For our analysis the confidence level is 0.95.

2.3. Irradiation facilities

In this section, we present the various experimental conditions used to benchmark conventional dosimeters (ionization chambers and radiochromic films) with alanine dosimetry. We first used a proton therapy clinical beam (100 or 226 MeV), and then a 5-7 MeV electron beam, allowing conventional and FLASH dose-rates irradiation.

2.3.1. Proton accelerator and gantry

At Institut Curie we mainly operated a 230 MeV C235 IBA proton cyclotron, able to produce proton pencil beam scanning (PBS) at conventional and ultra-high dose rate (i.e. around 1000 Gy/s for the instantaneous dose rate).

The cyclotron consists of two large, semicircular metallic hollow structures called dees. These elements are placed in a strong magnetic field generated by large electromagnets. Protons are introduced at the center of the dees structure by a source and are subjected to a high-frequency alternating electric field. This electric field grants acceleration as particles pass in between the dees, while the magnetic field constrains them into a spiral trajectory. With each pass through the accelerating gap, the protons gain energy, spiraling

2 | Materials and methods

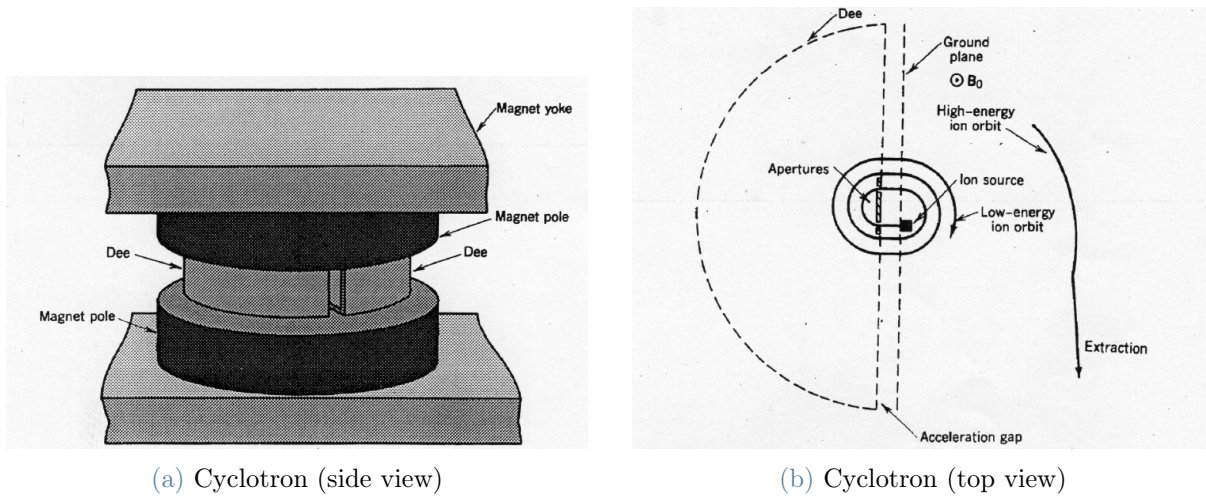


Figure 2.19: The cyclotron and its top view.

outward until they reach the desired energy. At this point a deflector is used to extract the particles and directed towards the treatment rooms.

The proton beam that is extracted is directed to two different types of treatment rooms at Institut Curie. The former room (called Y1) is equipped with passive scattering systems, which shape and modulate the beam by using physical absorbers and scatterers to achieve the needed dose distribution. The latter treatment room hosts a gantry: a large rotating structure that allows the beam to be delivered from multiple angles around the patient or the experimental target (Figure 2.20).

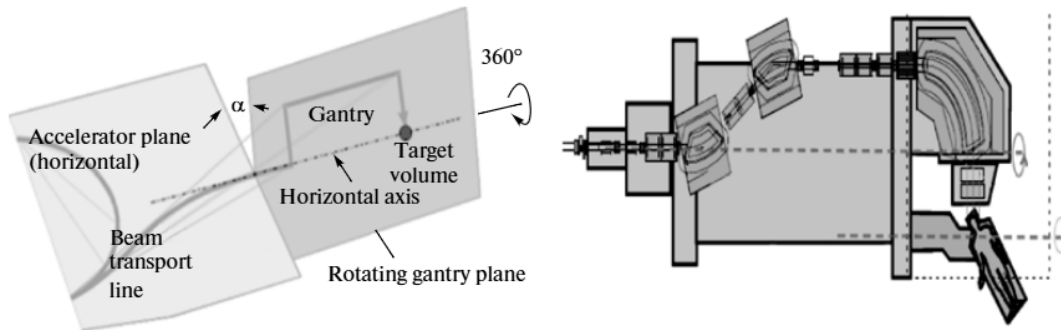


Figure 2.20: Scheme of a beam rotating system gantry.

The nozzle of the gantry can deliver the beam in three delivery modes: double scattering, uniform scanning, and pencil beam scanning. In double scattering mode (DS), the proton beam is spread out using scattering foils and collimators to create a uniform radiation field. Uniform scanning (US) delivers the beam by scanning a broader area using magnets to deflect the particles towards the target. Pencil beam scanning (PBS), on the other hand,

scans the target spot-by-spot to deposit dose in the most spatially precise way possible while magnetic fields are used control the spot's position and depth. Today, only the pencil beam scanning is used at Institute Curie Orsay.

2.3.2. How to irradiate dosimeters at the proton gantry

In the majority of the proton gantry experiments, the setup was the same: on the patient's bed, we placed a water equivalent (RW3 solid water plates, or a small liquid water tank) phantom, as we can see in Figure 2.21.

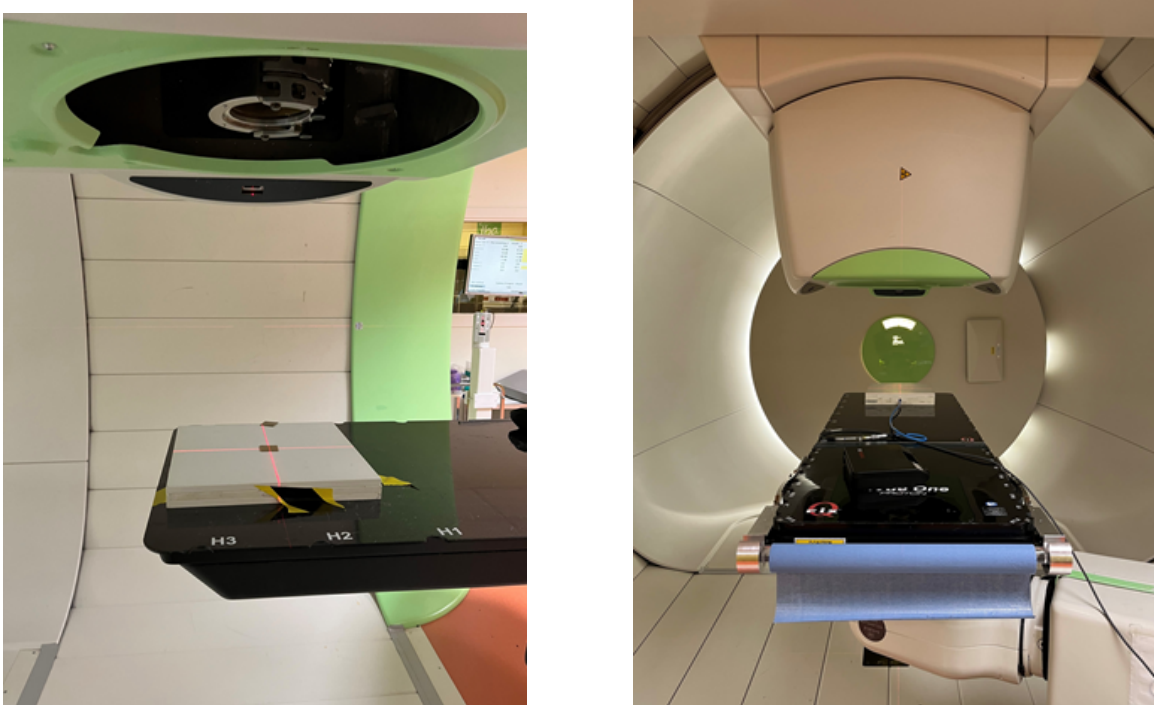


Figure 2.21: Irradiation setup at the proton gantry. Lasers are used to verify the dosimeter's alignment.

For the ion chamber's calibration (that we need to use as benchmark for the alanine's dose), it is advisable to use an hygrometer, barometer and thermometer to gather the environmental parameters of temperature, pressure and humidity.

The experimental setup for ion chamber irradiation consists of a gantry angle set to 0 degrees, with the ionization chamber positioned at the center of the field. The accelerator's head snout is almost fully retracted, and no collimator is used, resulting in an open field. A square field of $72 \times 72 \text{ mm}^2$ is used with an energy of 100 MeV. The slab phantom is placed directly on the treatment table and consists of a 2 cm slab positioned closest to the snout, with its surface aligned at isocenter. This is followed by a 2 cm slab that contains

the ionization chamber and a final 1 cm slab, completing the setup. This setup was used to estimate the dose in a broad beam scanned proton field with a reference dosimetical chain (chamber calibrated in absorbed dose to water).

For alanine and film irradiations, the same experimental setup was used as described above, with the only modification being the slab solid water thicknesses, adapted in order to have the different detectors at an equivalent depth in water. The ionization chamber was therefore removed and replaced with either films or alanine. In these cases, the phantom consisted of a 2 cm slab followed by an additional 1 mm slab to compensate for the thickness of the ionization chamber window. The films were then placed at the center of the field on a 3 cm slab, or in the case of alanine, a specially designed slab with a hole in the middle, precisely matching the size of the pellet.

This slab was prepared ad-hoc in the mechanic atelier by screwing a hole in the RW3 (opaque) water equivalent phantom with an area of 30 x 30 mm and 1 cm thickness, while the diameter of the hole was about 4 mm, same as the pellet.

The alanine needs to be handled with care, using gloves and being mindful of temperature and humidity jumps: the former can effect radical recombination, while the latter can effect mass [34].

2.3.3. Electron FLASH LINAC

The FLASH electron linear accelerator present at Orsay's protontherapy facilities is designed to deliver ultra-high dose-rate irradiation for pre-clinical studies. This state-of-the-art linear accelerator (LINAC), designed by the Italian company (S.I.T. Sordina IORT Technologies S.p.A) helps in the development and evaluation of FLASH radiotherapy by delivering doses of radiation in fractions of a second with mean dose-rates far exceeding 40 Gy/s, allowing to extensively study the biological response of the FLASH effect or to study the beam characteristics or new kinds of dosimeters.

This flash accelerator has the ability to produce electron beams with energies ranging between 4 and 7 MeV.

More in general, the linear accelerator has a structure made out of waveguides, which are excited in the microwave range by oscillating electric fields. The electrons are injected and accelerated in pulses as they pass through each consecutive cavity. Indeed, electrons are generated through thermo-ionic effect by the electron gun, as a continuous beam to be injected in the buncher: the electron continuous is accelerated and focused in bunches, to be phased with the acceleration electric field along the waveguide (producing

a pulsed output). The electrons gain energy as they travel: radiofrequency (RF) creates an electromagnetic field that boosts the electrons' speed (thus energy) with each pass through the RF cavities. The irradiation setup included a PMMA electron applicator on the head of the LINAC to improve dose profile uniformity, while its low Z minimizes bremsstrahlung radiation.

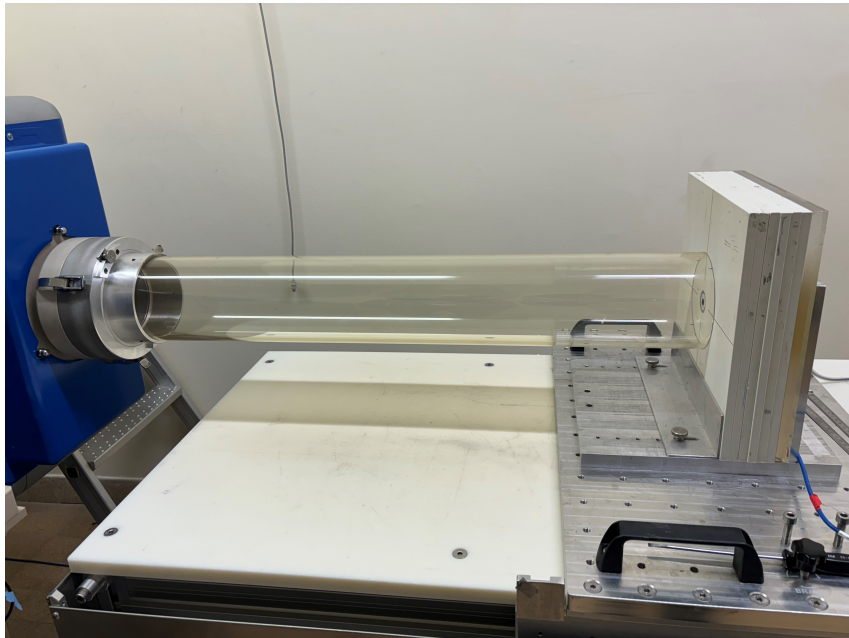


Figure 2.22: The electron FLASH LINAC head with the applicator.

The slabs used are solid water opaque phantoms and they were used to create a depth-dose profile and evaluate the maximum. It is to be noted that the usage of transparent slabs instead of opaque ones changes the results.

This machine was previously described in different papers, in particular a Monte Carlo model of the accelerator was published in Giuliano et al. [35] and in Bonfrate et al. [36].

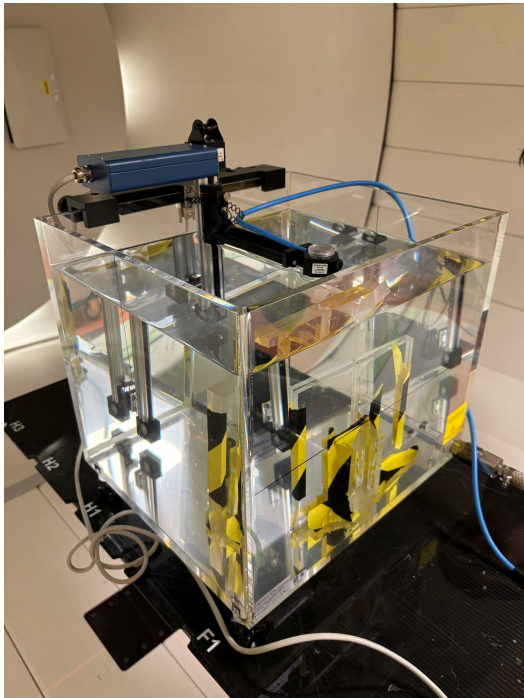
2.3.4. How to irradiate dosimeters at LINAC

Water tank irradiation

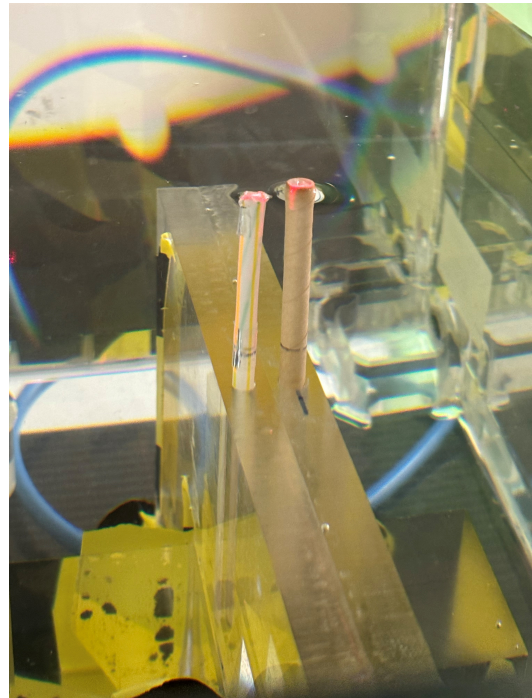
Since alanine is greatly impacted by humidity, it was of vital importance to create a support for alanine that protects it completely from water. Alanine was in fact submerged completely in water in the water tank system (see Figure 2.23a) so a water-tight system needed to be created. There is still no standard way to waterproof alanine so we tried to create our own new method.

The first idea was to use plastic drinking straws, cut in half, filled with a stack of alanine

pellets and then sealed back up with adhesive tape.



(a) The water tank.



(b) Straws at water level.

Figure 2.23: Experimental setup showing the water tank and straw alignment before irradiation.

in Figure 2.23b we can see the straws immersed in water. Although the waterproofing was successful, the system was not air-tight and secondary a peak showed after the Bragg peak, as we can see in Figure 2.24.

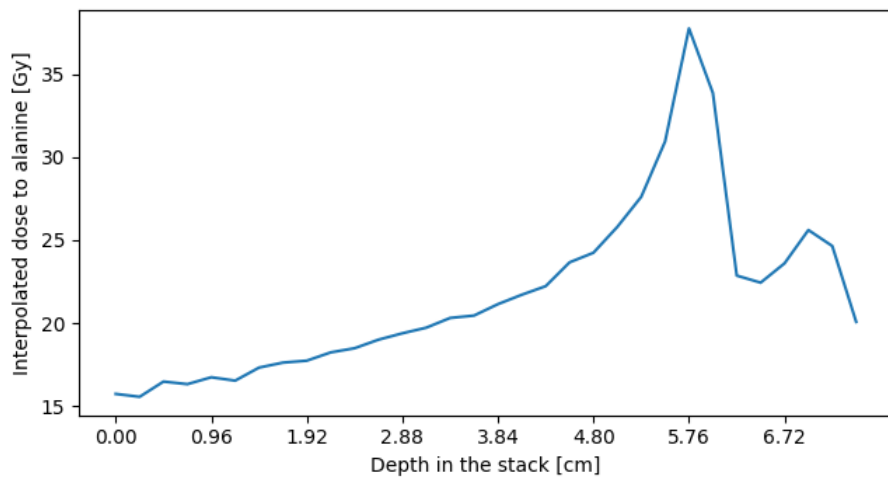


Figure 2.24: The peak-to-peak signal variation of EPR in function of the depth.

So, we not only need to respect water-tightness in our waterproofing system, but also

air-tightness. Furthermore, the in-straw stack irradiation brought the problem of labeling each pellet relative to its position in the stack. This tells us that the waterproofing method should be quick.

We crafted a new (and final) method for waterproofing which saw the usage of an ion chamber. The chamber was no longer working and its central cavity fit alanine perfectly so we secured the pellet in the cavity with some adhesive tape (like we can see in Figure 2.25).



Figure 2.25: Ion chamber with the alanine and the tape: the final waterproofing setup.

This new setup was placed on the mechanical arm of the water tank that was moved in precise steps (while the positioning of the straws in the other experiment was more error prone due to the varying geometry and buoyancy of the straws themselves). There still is an uncertainty due to the need of removing and re-setting in place the chamber after changing the pellet, but the system proved to be the most effective for obtaining a reproducible and accurate set-up for studying percent depth-dose profiles with alanine in water. The results (as we can see in section 3.3.3) showed a clear Bragg peak with no secondary peaks following it.

3 | Results

The results presented in this section focus on the characterization and validation of alanine dosimetry under both conventional and ultra-high dose-rate irradiation conditions. The findings include the optimization of EPR parameters, statistical analysis of dose calibration curves, evaluation of signal stability, and inter-comparison with alternative dosimeters such as ionization chambers and radiochromic films. Furthermore, the influence of Linear Energy Transfer (LET) effects on alanine response was assessed and the variation in dose-response due to LET differences, particularly in proton irradiation, was analyzed. The investigation was performed both experimentally and with Monte Carlo simulations

The standard methods used for data manipulation and analysis are described in section 2.2.6.

3.1. EPR parameter optimization

In this section, we describe the different steps and results concerning the optimization of the EPR signal measurement recipes, as well as the study of the various parameters (temperature, power, etc.) that can modify the signal. A first experiment was performed to better understand the effects of the electron paramagnetic resonance (EPR) spectrometer parameters on the pellet reading. The pellet used was always the same one, irradiated with 100 MeV protons at 40 Gy, coming from the calibration of Wednesday 28 February 2024 (see section 3.2.1).

The basis recipe for the EPR spectrometer is called "ICPO" and it can be found in Appendix B, as Figure B.1. It was crafted for low (therapeutic) doses. Different parameters were optimized in order to see their effects separately, and in particular in order to reduce the total acquisition duration while keeping minimal uncertainty.

Figure B.1 shows the recipe that we used for basically all of the subsequent EPR readings. Its parameters have been optimized by trial and error during different readings, and have since been kept constant to assure uniformity and comparability between different

measurements.

On the other hand, we need a more in-depth study to prove if the chosen values of these parameters are really the best option. We will investigate this in the following sections.

3.1.1. Modulation amplitude optimization

In this section, we describe the effects of modulation amplitude variations on the EPR signal.

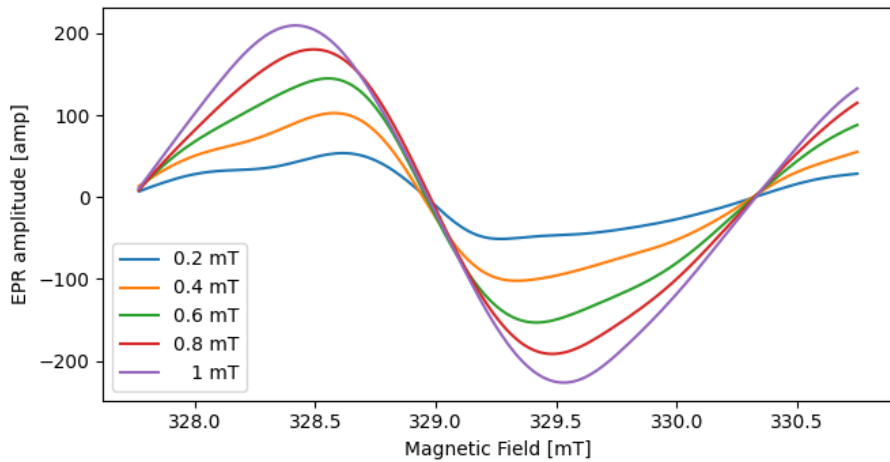


Figure 3.1: EPR peak-to-peak (PTP) signal for a 40 Gy pellet irradiated with 100 MeV protons in phantom. The legend shows the different modulation amplitudes of the study.

Data is reported in Table C.1, where RSD represents the relative standard deviation, and the estimated dose is shown to illustrate the dose variation (for a same calibration curve) when the modulation is modified. We can also see that the higher the modulation, the greater the amplitude of the signal and the smaller the uncertainty. Also, amplitudes will be referred to have an arbitrary and dimensionless unit of measure called [amp]. During the analysis, the overall uncertainty on the pellet signal has been calculated using the standard deviation σ , to take into account the uncertainty related to reproducibility. We will call it $\sigma_{reproducibility}$, sometimes abbreviated to $\sigma_{rep.}$. Ten measurements performed for the same pellet to calculate this standard deviation, following the protocol in section 2.2.5.

In Table C.1, the normalized amplitude value represents the mean over the 10 different measurements, from which we can infer $\sigma_{reproducibility}$.

On the other hand, signal stability was monitored using internal marker (IM) reference signal, whose amplitude was used to normalize the electron paramagnetic resonance (EPR)

signal's amplitude. More in-depth explanation of this normalization method can be found in section 2.2.6.

The interpolated dose for a certain value of amplitude difference (peak-to-peak or PTP) has a corresponding standard deviation in [Gy] that has been interpolated from $\sigma_{reproducibility}$ after being normalized to the IM amplitude. To also take into account the uncertainty of the calibration curve we used to interpolate, we used the error propagation method that is better explained in section 2.2.6.

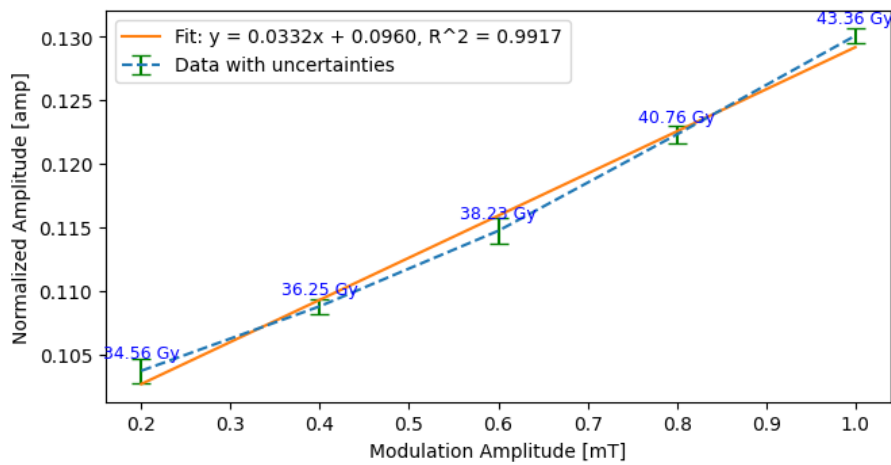


Figure 3.2: Correlation between normalized amplitude and modulation amplitude. Each label represents the dose interpolated from the calibration in section 3.2.1.

The fit performed in Figure 3.2 lays on a linear curve $y = ax + b$, where the coefficients of the fitted polynomial $a = 0.003119$ and $b = 0.096014$, with $\sigma_a = 0.001747$ and $\sigma_b = 0.001159$. On the other hand, the R^2 value is equal to 0.9917.

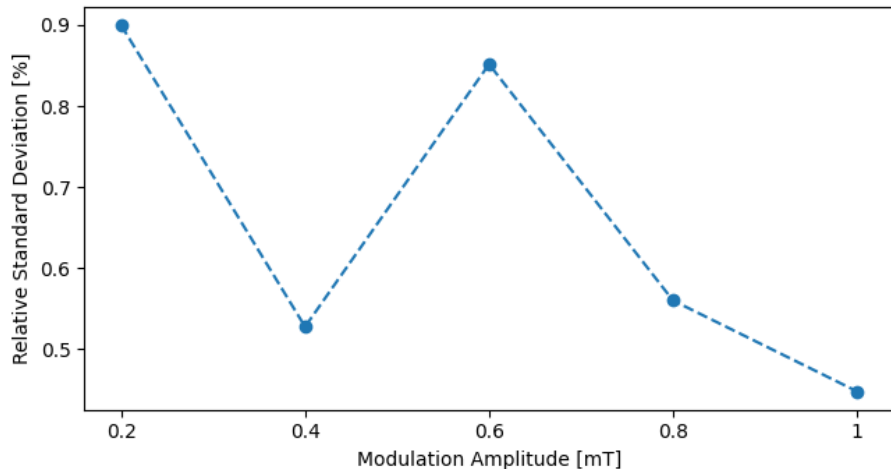


Figure 3.3: The relative standard deviation over different modulation amplitudes.

Figure 3.3, derived from table C.1, we can see that the minimum RSD (relative standard deviation) is around 1 mT, but at that value of modulation amplitude, slight heating might start to affect the alanine pellet. Indeed, since the cavity's walls are metal, an increased modulation amplitude means increased currents running on the walls of the cavity. An outcome would be slightly increasing the volume of the pellet, and a subsequent decrease of reproducibility. The longer we use the spectrometer while under these conditions, the more these side effects will influence the outcome. An intermediate choice will therefore be to use 0.8 mT.

3.1.2. Microwave power optimization

In this section, we describe the effects of microwave power variations on the EPR signal.

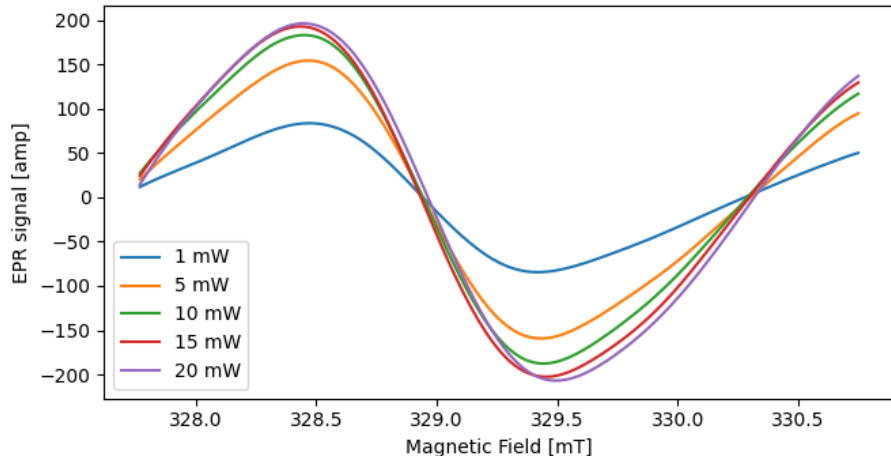


Figure 3.4: EPR PTP signal for a 40 Gy pellet irradiated with 100 MeV protons in phantom. The legend shows the different microwave powers analyzed.

In Figure 3.4, the variation of the EPR signal is shown as a function of the microwave power.

Data is reported in Table C.2. Like explained above, the amplitude of the peak to peak signal was normalized to the internal marker's amplitude, that can be seen in Figure 3.5.

To show the saturation behavior with varying of the microwave power, we will use the relation in equation 3.1, as suggested in [37].

$$A(P) = A_0 \cdot P \cdot \left(1 + \frac{P^2}{P_{\text{sat}}} \right)^{-\text{exp}} \quad (3.1)$$

Where $A(P)$ represents the saturation dependencies of the magnitudes of components, P is the microwave power in mW and A_0 , P_{sat} and exp are fitted parameters characterizing saturation behavior. In Figure 3.6, we can see that the fitted parameters are $A_0 = 49$, $P_{\text{sat}} = 2.80$ mW, $\text{exp} = 0.52$ and $R^2 = 0.96$. The script used to perform this estimation can be found in Appendix A.2. But as we know alanine creates three different radicals, R1, R2 and R3, and as Ivannikov et al. suggest [37], for the component R1 and for the total magnitude considering the spectrum which integrates all three components, the power dependence is well fitted by the equation 3.1, using the total magnitude of the peak to peak signal which integrates all three components. If we would like to separate all of the three components R1, R2 and R3, we would need to use a different method

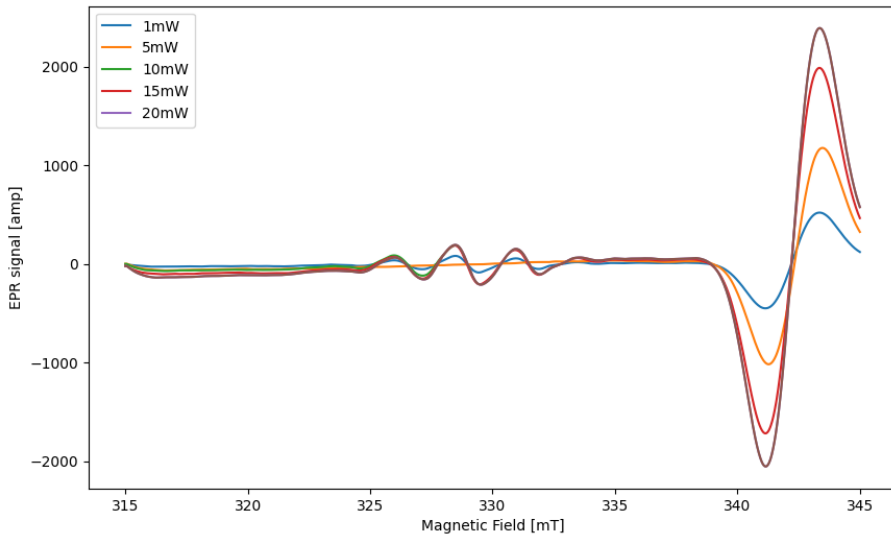


Figure 3.5: Internal marker variation (the signal between 340 mT to 345 mT) following a change of microwave power. The EPR signal we are interested in for the dose lays between 328 and 330 mT.

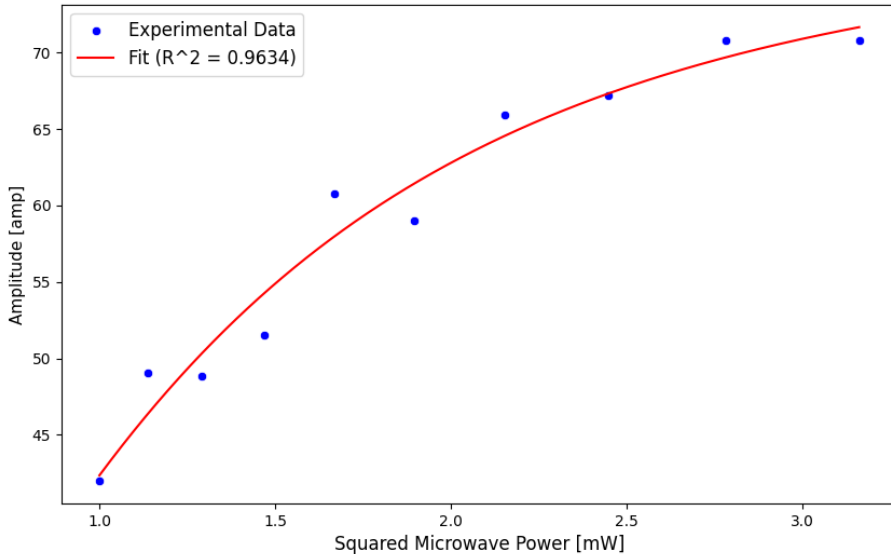


Figure 3.6: The squared microwave power is linked to amplitude with a squared function behavior.

and equation allowing a separation and deconvolution of the R1, R2 and R3 components. This is because of for these components the saturation power parameter P_{sat} is too high to be fitted together with the exponential parameter b in the measured power range.

Fitting the amplitude variation and dose variation, shown in Figure 3.7, with a linear curve, the result is $y = -0.004139x + 0.171420$, with R^2 equal to 0.97. The uncertainties

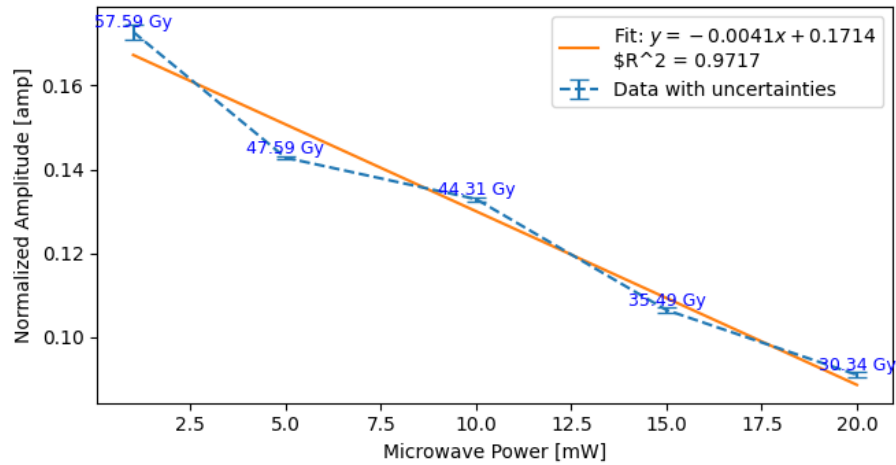


Figure 3.7: Fit of squared microwave power values against normalized amplitude. Each label represents the dose interpolated from the calibration in section 3.2.1.

on the y axis for each point are $\sigma_a = 0.000408$ and $\sigma_b = 0.005002$. Figure 3.7 shows that the decreasing trend of the fit curve, given by decreasing microwave power, yields to a decrease in the interpolated dose. Thus, if we do not chose the optimal microwave power, we could have underestimation of the dose.

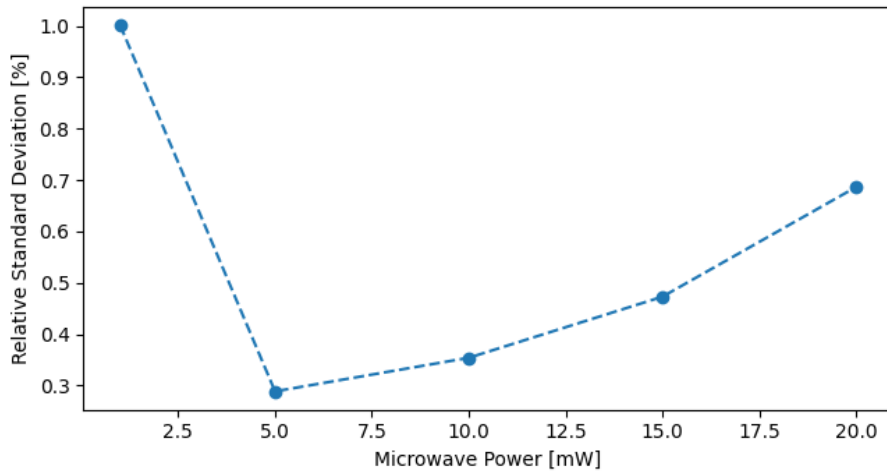


Figure 3.8: Behavior of the RSD with microwave power variation.

Ideally, the best choice of microwave power would be the one with minimum RSD. In Figure 3.8, derived from table C.2, we can see that 5 mW and 10 mW have the minimum RSD, with a value of 0.29 %.

3.1.3. Field sweep time optimization

For this test, we measured the EPR signal for different field sweep times, as shown in Figure 3.9.

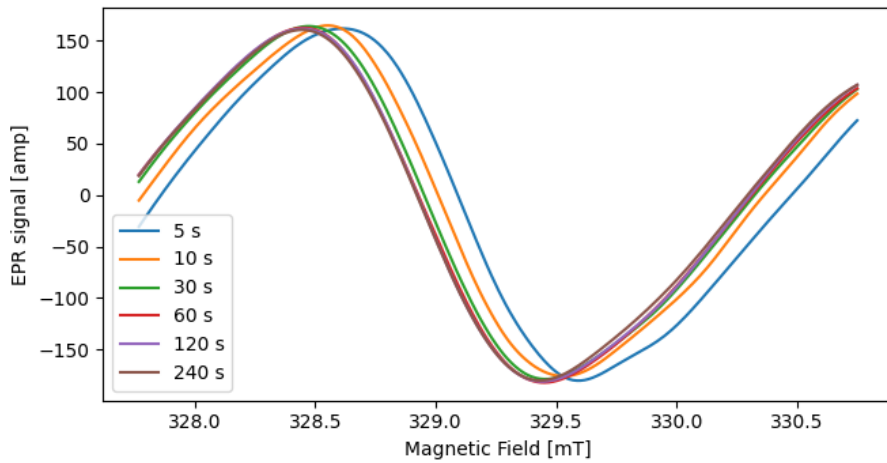


Figure 3.9: EPR signal for a 40 Gy pellet irradiated with 100 MeV protons in phantom. The times in the legend are relative to the EPR time sweeps.

Data is also reported in Table C.3, where we treated and normalized the data as described in the above sections, following the methods in section 2.2.6. We can see that increasing the sweep time leads to a decrease in the peak amplitude of the EPR signal.

ing the time sweep slightly does not modify the PTP amplitude, nor the uncertainty, significantly. Finally, by selecting what we consider as best parameters for the

To switch between $\sigma_{\text{reproducibility}}$ in [amp] to [Gy], we used the results obtained in 3.2.1, only this time we used non-normalized amplitudes to that they can appear consistent with the amplitudes in this experiment. We estimate the final $\sigma_{\text{reproducibility}}$ in [Gy] with error propagation as seen in section 3.2.3.

As we have seen in the former sections the best choice of parameter, in this case the time sweep, is the one which minimizes RSD. A lower RSD indeed means higher signal to noise ratio (SNR). We can better see the variation of $\sigma_{\text{reproducibility}}$ with sweep time in Figure 3.10, where we can also infer that there is no substantial gain in SNR after 30 s. The ideal behavior in the figure should be that of a function monotonically decreasing, but we would better chose a value of sweep time that optimizes our time management when we have a large number of samples to measure: a one minute sweep time would fit our goal while maintaining good SNR.

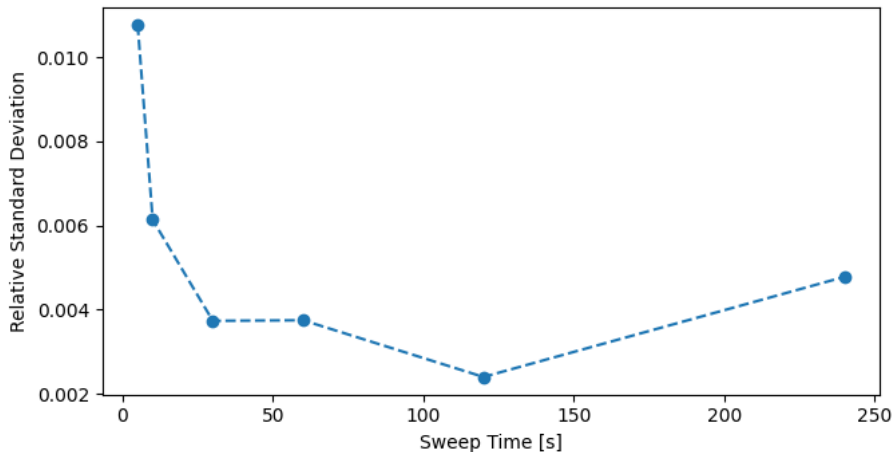


Figure 3.10: The relative standard deviation for different sweep times.

3.1.4. Cavity temperature

Cavity temperature can change through the air conditioning of the room. In our experiment, the room temperature was changed between 17 °C to 30 °C with a subsequent cavity temperature variation between around 28 °C to 38 °C.

Data is reported in Table C.4, the standard deviation relative to reproducibility is not shown for simplicity's sake, but is similar to the one obtained with similar parameter settings.

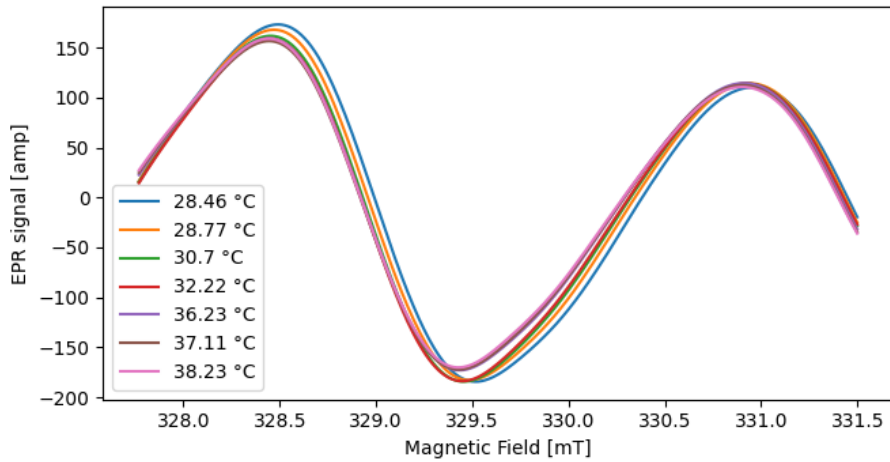


Figure 3.11: EPR signal for a 40 Gy pellet irradiated with 100 MeV protons in phantom. The legend shows the EPR cavity temperatures.

Much like in the other sections, the conversion between [amp] and [Gy] in σ_{amp} was done with the error propagation method. In this case the non-normalized calibration curve in needed, which can be found in Figure ??.

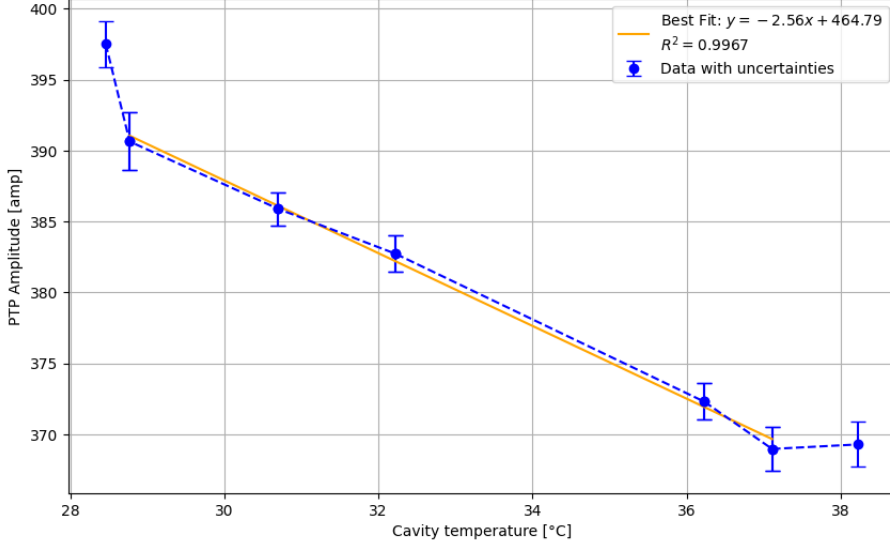


Figure 3.12: The variation of the amplitude as a function of the temperature, which shows a decreasing trend.

PTP amplitude and temperature are linearly correlated in between 28.77°C and 37.11°C, as shown in Figure 3.12. The linear correlation of shape $y = a x + b$ has $a = -2.56$, $b = 464.79$ and $\sigma_a = 0.09$, $\sigma_b = 3.01$. The R^2 value is 0.99.

In Figure 3.13 we reported the effect of using different room temperatures on the estimated

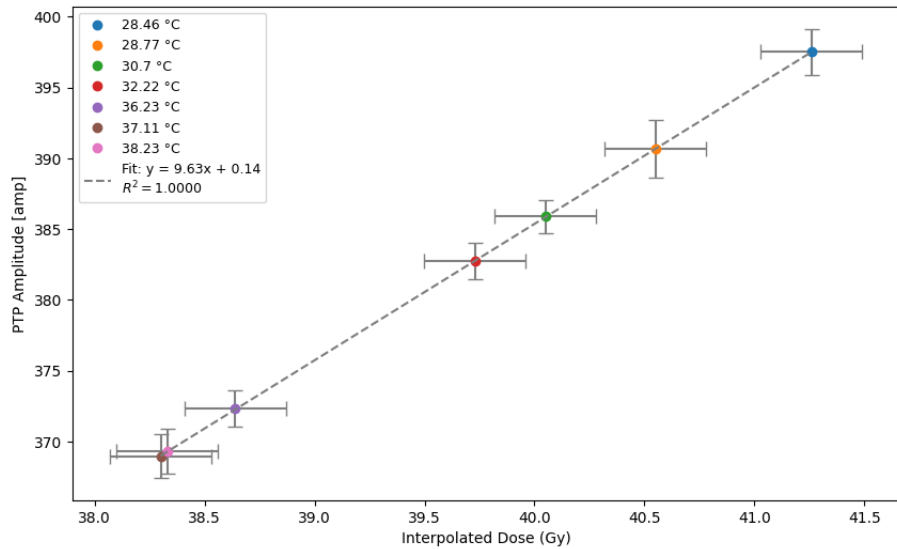


Figure 3.13: The linear correlation between amplitude and temperature.

dose: we can see that a 2°C increase will modify the estimated dose by 0.5 Gy, which corresponds to an uncertainty of 0.6 % every degree. In particular, in Figure 3.13, the result in dose is obtained through interpolation with the calibration curve from 3.2.1, which is valid for 100 MeV protons irradiated in radiometric phantom, much like the pellets in this parameter optimization study. The pellet of this benchmark calibration were all read after the spectrometer's warm-up procedure, which brings the internal cavity to around 32°.

The fit function is $y = 9.63 x + 0.14$ with $\sigma_a=0.01$ and $\sigma_b= 0.45$, where $R^2 = 1$.

3.2. Estimation of a dose calibration curve for proton irradiation

This section presents the methodology and results for the determination of a dose calibration curve for proton irradiation using alanine dosimetry. Irradiations were performed in different conditions (solid phantom or water, varying energy, etc.) to isolate noable effects. The calibration curve is essential for accurately relating EPR signal intensity to absorbed dose, ensuring the reliability of alanine as a dosimeter for high-energy proton beams. The study involves systematic irradiations at different dose levels, followed by statistical analysis to evaluate the linearity and robustness of the calibration model.

3.2.1. Irradiation in solid water phantom

On Wednesday 28 February, 2024 we performed the first experiment at the proton gantry using 100 MeV protons to irradiate four alanine pellets at doses 10 Gy, 20 Gy, 30 Gy, 40 Gy inside a radiometric phantom created by opaque PMMA slabs. The procedure of irradiation follows the outline for in-phantom irradiation, explained in section 2.3.2. The data was analyzed with the Python script found in Appendix A.3, that yields the results of the calibration. This script is the baseline to various subsequent scripts that will entail the creation of a calibration curve from any EPR raw data. Indeed, it has been used (with the necessary modifications) in most of the experiments. Like explained in section 2.2.6, the evaluation of the signal stability is done by checking the internal marker (IM). Data is reported in Table C.5, and the coefficient of variation is 0.02%.. Like suggested in section 2.2.6, in Table C.5, the averaging of the peak to peak (PTP) signal was performed over 10 readings, so that we can also compute the standard deviation due to reproducibility issues. Subsequently, the average amplitude for each dose was divided by the corresponding IM amplitude to normalize it. The same thing was done for $\sigma_{reproducibility}$.

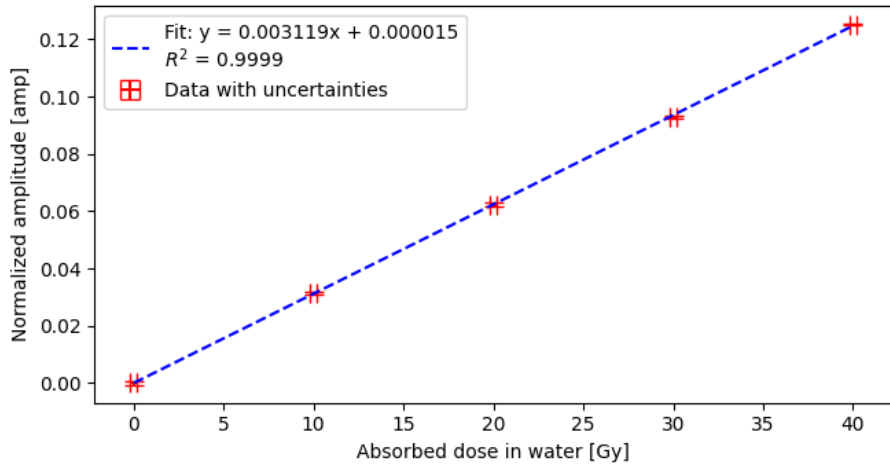


Figure 3.14: Calibration curve for 100 MeV protons in solid phantom, obtained with EPR signal amplitude analysis from alanine pellets.

Fitting the obtained and normalized amplitudes to the corresponding irradiated doses, we obtain a linear function $y = ax + b$ where the coefficients of the fitted polynomial are $a = 0.003119$ and $b = 0.000015$, with $\sigma_a = 0.000015$ and $\sigma_b = 0.000366$. We can also see that the correlation factor R^2 is close to 1.

3.2.2. Irradiation in water

In the next experiment, the aim was to evaluate whether the calibration curves relative to an irradiation in a water tank would differ from the ones obtained from irradiation in phantom (see section 3.2.1). The method of water irradiation and waterproofing of the pellet is the one described in 2.3.2. Data is reported in Table C.6, the coefficient of variation relative to the IM is 0.24%. The amplitudes and standard deviations were treated like in the above sections (see 3.2.1 and 3.1.1) to obtain the mean and normalized values.

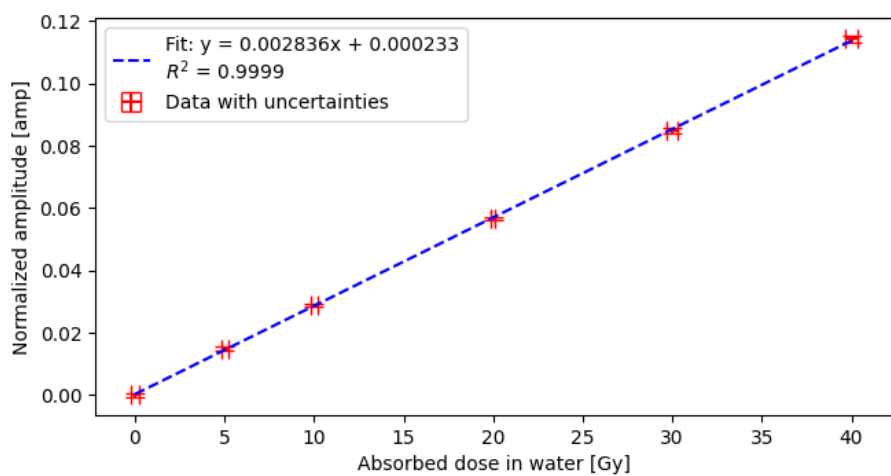


Figure 3.15: Calibration curve for 100 MeV protons in water, obtained with EPR signal amplitude analysis from alanine pellets.

The fit was performed like in 3.2.1 and it also shows a linear function $y = ax + b$ where the coefficients of the fitted polynomial are $a = 0.002836$ and $b = 0.000233$, with $\sigma_a = 0.000016$ and $\sigma_b = 0.000356$. Indeed, we can see that the coefficients are almost identical for both calibrations.

The calibration curve for phantom irradiation shows a $R^2=0.9999$, while the calibration curve for water irradiation is $R^2=0.9999$. Applying the Monte Carlo bootstrap method described in section 2.2.7, the result of this analysis is:

- The slope difference between the two curves is statistically significant at 95% confidence level. This means we can confidently reject the null hypothesis that the two slopes are identical at a 95% confidence level. Thus, the relationship between the variables differs between the phantom and water irradiations;
- The intercept difference between the two curves is not statistically significant at 95% confidence level. This implies that the null hypothesis (that the two intercepts are

identical) cannot be rejected at the 95% confidence level. Any observed difference in intercepts is likely due to random variability.

The most important feature of this calibration curve is the slope, since the intercept could be influenced as easily as by varying the number of data points. The slope on the other hand, holds information tied for example by the linear energy transfer of the radiation. Indeed, with water and phantom irradiations the surrounding environment of the pellet might change in a way that introduces a different amount and type of secondary radiation, as well as the density of the material.

3.2.3. Blind test

To test the calibration curve resulting from the experiment of February 28th, we tried to scan a pellet irradiated with an independent (i.e. not used for the calibration) amount of dose using the calibration curve obtained in 3.2.1. This serves as a so called "blind test". The environmental characteristics and geometry of the irradiation are based on a similar setup (the pellet was put in solid water, in a 100 MeV proton beam). We used the same recipe (B.1) to read the signal and the same Python script (see Appendix A.3) to try and minimize inconsistencies between the calibration curve obtained above and the result of the test. The mean (non normalized) amplitude of the EPR signal obtained is 71.27 [amp] with a $\sigma_{reproducibility}$ of 1.78 [amp]. This amplitude was confronted with the non normalized amplitudes for the given doses, and was found to be in the range of 0 Gy to 10 Gy. The normalization was thus performed by dividing the non normalized amplitude by the mean of the IM signal of 0 Gy and 10 Gy. The result of the unknown pellet is 0.02 [amp] of PTP signal, with standard deviation 0.0005 [amp].

To switch in between [amp] and [Gy] for $\sigma_{reproducibility}$, one needs to plug the [amp] value in the linear correlation (as the y-value, let us call it $y_{unknown}$), and obtain the relative [Gy] (as the x-value). Since the calibration curve has some uncertainty σ_a and σ_b for the a and b parameters of the curve, we need to perform the error propagation method and find σ_{total} , as showed in equation 3.2. The method for error estimation is better described in section 2.2.6.

$$\sigma_{total}^2 = \left(\frac{\partial x}{\partial y_{unknown}} \right)^2 \sigma_{reproducibility}^2 + \left(\frac{\partial x}{\partial a} \right)^2 \sigma_a^2 + \left(\frac{\partial x}{\partial b} \right)^2 \sigma_b^2 \quad (3.2)$$

Error propagation translates to an unknown dose of 7.34 Gy with uncertainty $\sigma_{total} = 0.22$ Gy, as seen in Figure 3.16. In reality, the irradiated dose for the pellet was of 7 Gy, which turns in a 4% error, compatible with uncertainties for this dose level. The Relative

Standard Deviation (RSD) for this single irradiated pellet, between the values 7 and 7.34 Gy, was found to be approximately 2.37%.

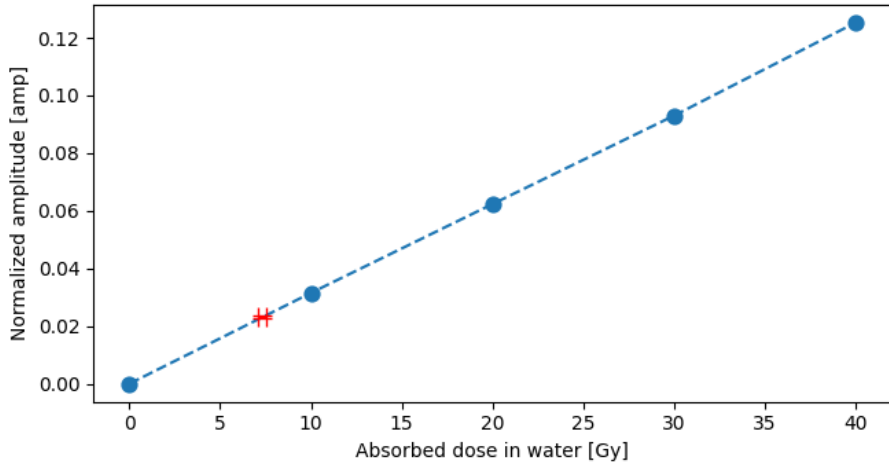


Figure 3.16: Evaluation of the dose delivered to a pellet irradiated with an unknown (or independent) amount of dose, using the calibration curve for 100 MeV protons in a solid water phantom.

3.3. LET effects in a proton beam

3.3.1. Irradiation at different initial beam energies

In this section we create and analyze the calibration curve relative to the experiment performed on Tuesday 24 April, 2024, where we irradiated several pellets in the proton gantry at 100 MeV and at 226 MeV at doses of 10 Gy, 20 Gy, 30 Gy, 40 Gy. The irradiation was performed in phantom like described in section 2.3.2. The aim of this experiment was to see the effect of irradiation at 100 MeV and 226 MeV (both energies are used in therapeutic irradiation) on the calibration curve. Like we did in section 3.2.2, we want to see if there would be any difference in calibration curves relative to different proton energies, using the method described in section 2.2.7.

Starting from the 100 MeV irradiation, data from this experiment can be found in Table C.10, where it was treated and normalized as explained in section 2.2.6. The coefficient of variation of the IM is 0.02 %. The same procedure was followed for the 226 MeV irradiation. Data from this experiment can be found in Table C.7, where it was treated and normalized as usual. The IM's coefficient of variation is 0.05%.

In both cases (100 and 226 MeV), we used a linear function $y = ax + b$. In particular, the 100 MeV calibration curve gives a $R^2=0.9995$, while the 226 MeV calibration curve

fives a $R^2=0.9998$.

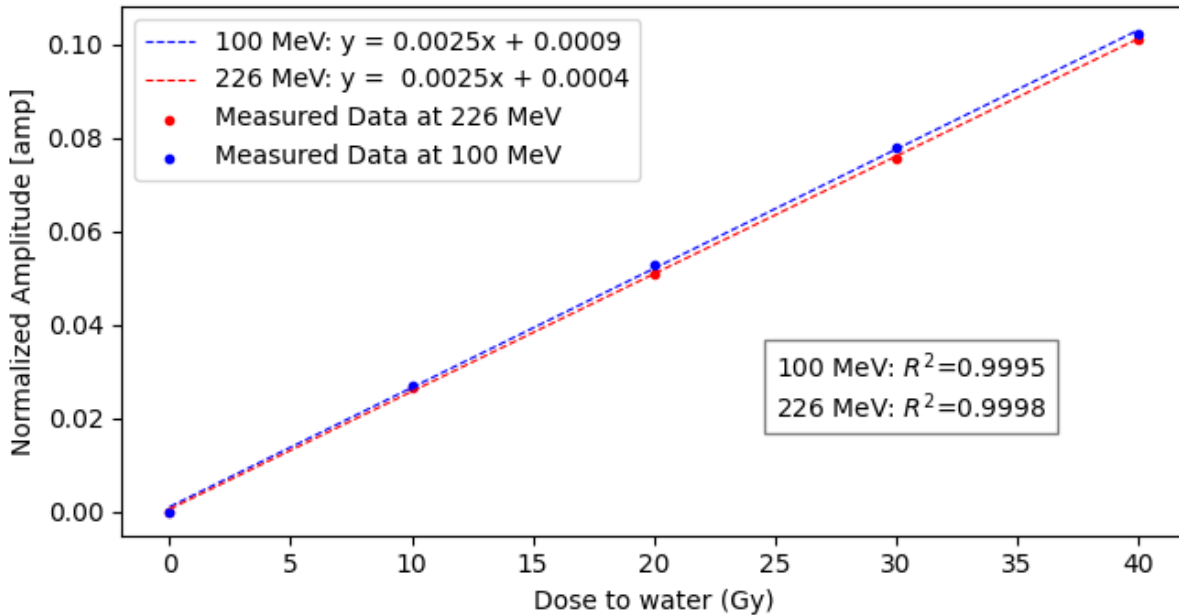


Figure 3.17: The two different calibration curves for 100 MeV and 226 MeV proton energy irradiation in alanine. Error bars were not reported to improve readability but are presented in Table C.10 and C.7.

3.3.2. Statistical analysis for different energies irradiation

Since the results shown in the section above are qualitatively very close for the two energies. In order to compare the fits, we used the Monte Carlo bootstrap method described in section 2.2.7 . The result of the analysis shows that:

- The slope difference between the two curves is not statistically significant at 95% confidence level. This implies that the null hypothesis (that the two intercepts are identical) cannot be rejected at the 95% confidence level. Any observed difference in intercepts is likely due to random variability rather than a true difference;
- The intercept difference between the two curves is not statistically significant at 95% confidence level, see the above point for the interpretation.

The result might suggest that LET (or energy) differences in the 100 MeV and 226 MeV beam do not have significant effect on the calibration curve. Note that for this test, the alanine pellets were placed at the entrance of the proton beam (where the beam has 100 and 226 MeV energy) so LET differences might be small between the beams.

3.3.3. Bragg peak measurement

On Wednesday 3 July, 2024, we irradiated alanine pellets inside of a modified ion chamber, using transparent tape to waterproof it. The ion chamber was lowered into the water tank with the aim of estimating the Bragg Peak shape by reading the PTP amplitudes coming from the pellets. The irradiation setup and waterproofing method are better described in 2.3.2. The results from this experiment were obtained using the script that can be found in Appendix A.4.

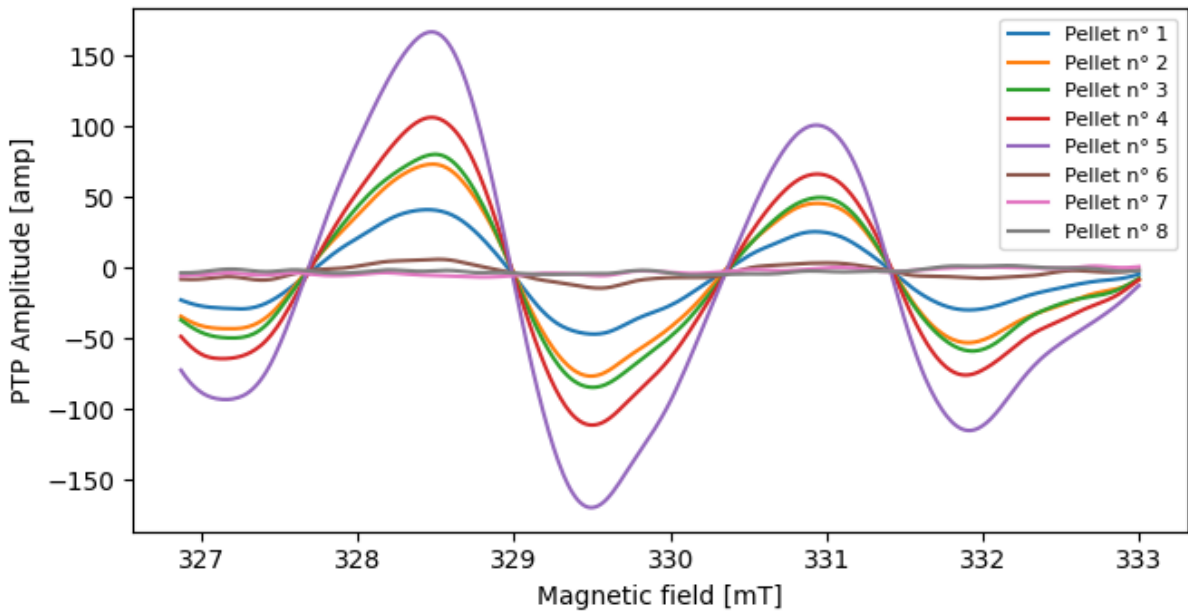


Figure 3.18: EPR signal for alanine pellets irradiated with 100 MeV protons in water inside of a ion chamber "shell". The numbers in the legend are relative to the pellet number, and with its increase the depth also increases.

Data is reported in Table C.11. As per standard procedure, the amplitude was normalized to IM amplitude and this time also to the thickness of the alanine pellet, which is 2.4 mm. Indeed, alanine cannot give a point-like response and so its response needs to take into account the thickness (since in this case irradiation was performed along its axis). We remind that alanine's dimensions are 2.4 mm thickness and 4 mm diameter. To speed up the measurement, and since the aim of this experiment was not to create a calibration curve, we skipped the evaluation of $\sigma_{reproducibility}$ for every pellet, opting to just evaluate the one at the maximum measured amplitude. Indeed, $\sigma_{rep.,max} = 0.0002$ [amp], with a relative $\sigma_{rep.,max} = 0.14$ Gy, found through error propagation . On the other hand, the coefficient of variation of IM is 0.12%.

In Figure 3.19, the alanine data has been shifted of +0.125 cm, to take into account the

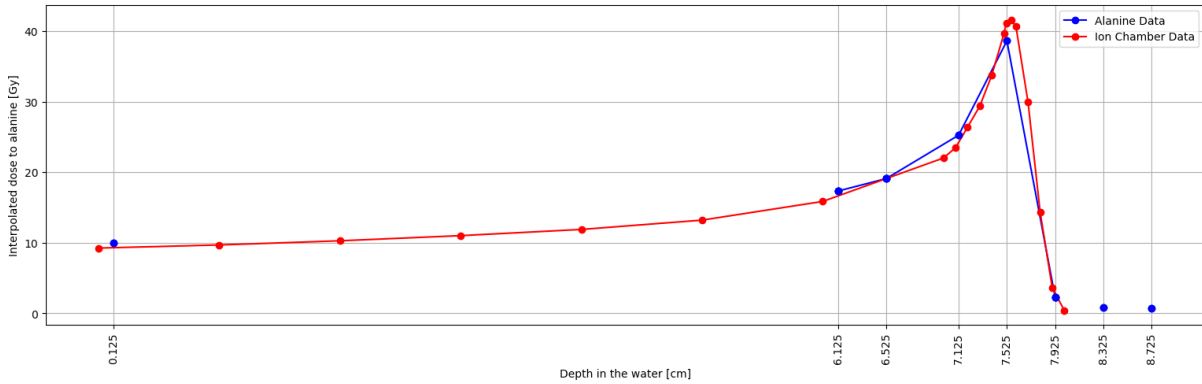


Figure 3.19: Bragg peak depth-dose profiles obtained for alanine dosimeter and ion chamber.

different geometric setup between the ion chamber and the alanine. The sampling within the peak appears quite low, thus to try and increase it we will add one data point to the Bragg peak area.

We will use data obtained from the experiment of Wednesday 22 May, 2024, where we irradiated a stack of pellets in a straw for waterproofing. Before this experiment, we tried to irradiate alanine in a stack-formation inside of some drinking straws as waterproofing. The results showed a secondary peak other than the Bragg peak and were thus discarded, but in the data we found a maximum amplitude of about 421.37 at 7.5 cm depth, translating to a dose of 40 Gy. Let's re-propose this value in the dataset of this new experiment. We can see the result in Figure 3.20. Indeed, this result suggests that

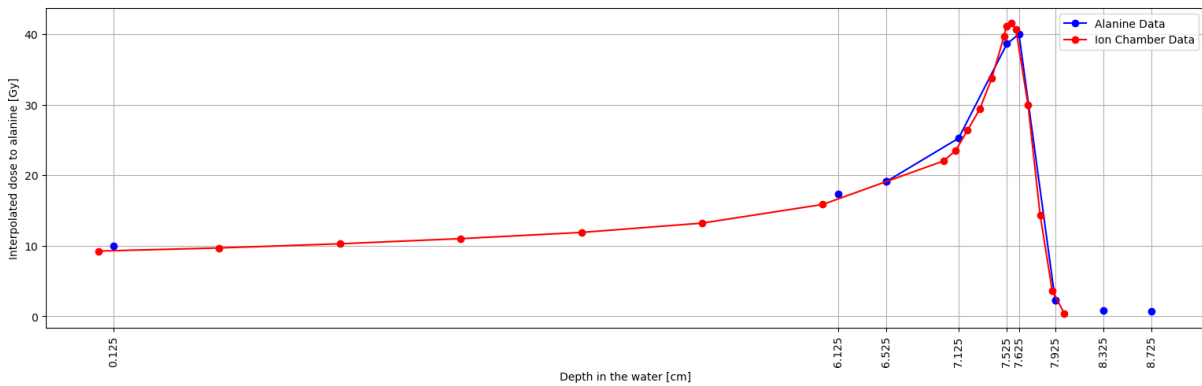


Figure 3.20: Bragg peak shapes for alanine dosimeter and ion chamber with the new data point relative to the old experiment in the area of the Bragg peak.

the number of sample points around the peak needs to be chosen carefully and, at least for this experiment, was too low to the point that we could not see the full development of the peak.

To try and correct the sampling problem underlined above, on Friday 2 August 2024, we irradiated alanine pellets inside of the modified ion chamber to waterproof it, now increasing the sampling to one pellet every 0.25 cm in the Bragg peak region, while in the proximal and distal part sampling is kept low so not to waste time in both irradiation and measurement.

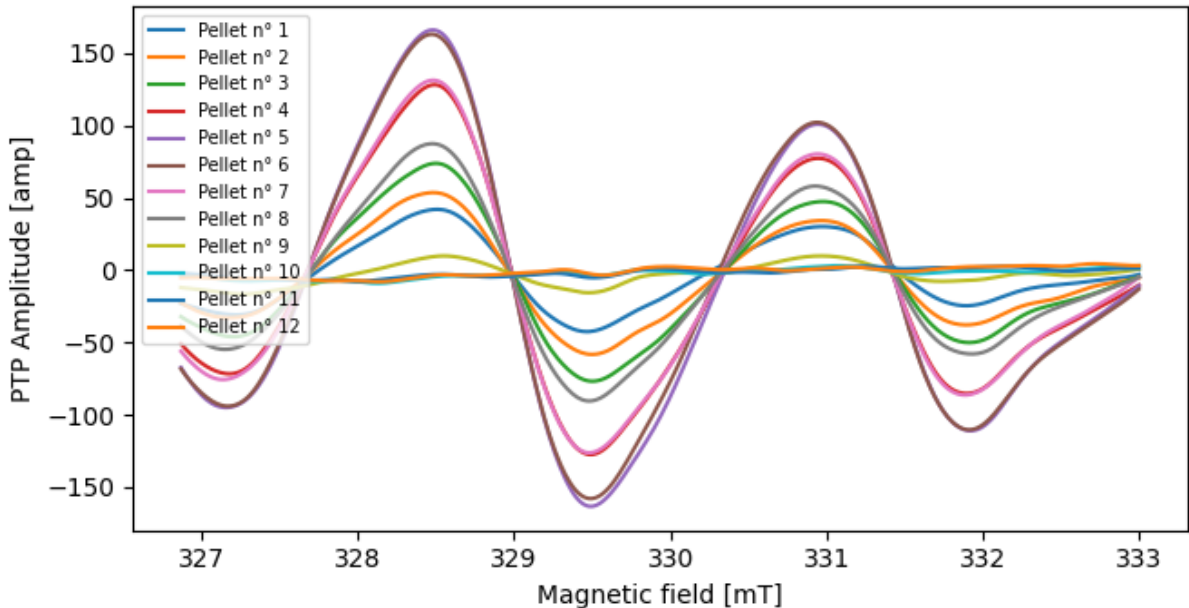


Figure 3.21: EPR signal for alanine pellets irradiated with 100 MeV protons in water inside of a ion chamber "shell". The numbers in the legend are relative to the pellet number, and with its increase the depth also increases.

In this experiment we increased the sampling to every 0.25 cm, thus increasing also the number of pellets, as it can be seen in Figure 3.21, as opposed to 3.19. In Table C.12 we can find the data, where the conversion between [amp] to [Gy] used a calibration curve has been crafted specifically for this experiment, whose behavior is linear, with coefficients $a=0.001194$, $b=0.000279$ with $\sigma_a=0.000009$ and $\sigma_b=0.000191$.

In Figure 3.22, the alanine spectrum has been shifted by +0.25 cm to align with the shape of the ion chamber profile. This differs from figure 3.3.3, where a shift of 0.125 cm was applied, a value that also holds for figure 3.3.4. Another result from this experiment is that the agreement between alanine and ion chamber is good at the entrance of the Bragg Peak, but seems to deteriorate in the final part of the Bragg Peak, in agreement with a possible dependence on the LET of protons.

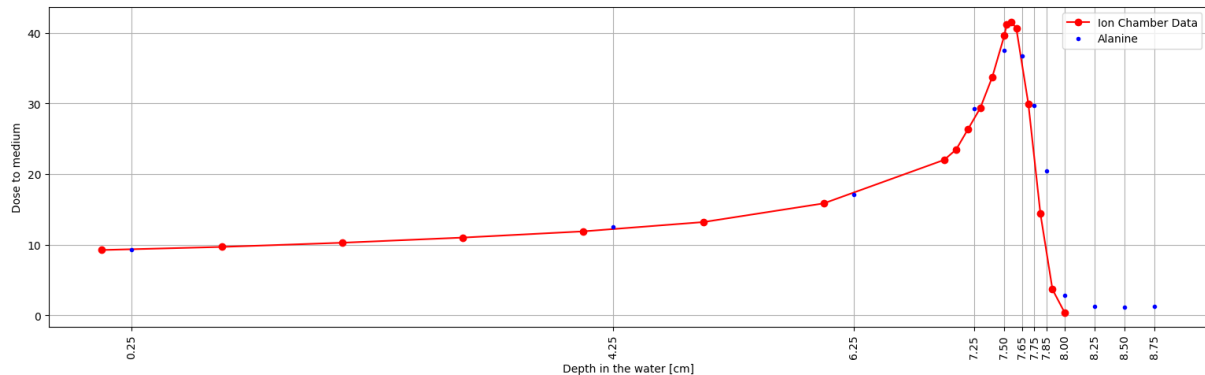


Figure 3.22: Bragg peak shapes for alanine dosimeter and ion chamber, with increased sampling within the Bragg peak.

3.3.4. Monte Carlo simulations

In this section our aim is to simulate the Bragg Peak behavior and LET (also referred to as TEL) possible dependence in alanine. Furthermore, on the same plot, we added the experimental points coming from our experiments to see how they compare. The simulation used 100 MeV protons, like in the experiments from sections 3.3.3.

The MC simulation code TOPAS (TOolkit for PArticle Simulation v3.8 based on Geant4.11) was parameterized and updated in this study to perform simulation of the irradiation set-up with our proton pencil beam scanning system. The TOPAS simulations were run with a physics list composed of seven modules: "tsem-standard opt3 WVI", "g4h-phy QGSP BIC HP", "g4decay", "g4ion-binarycascade", "g4h-elastic HP", "g4stopping", "g4radioactivedecay". A total of 10^8 proton histories were simulated for each setup to obtain a level of relative statistical uncertainty of less than 1% at each voxel throughout the distribution. The simulations were run on a multiprocessor Linux cluster. In this simulation, the beam was precisely modeled and simulated, in particular the shape of the field used to irradiate the pellets. The results will also show good agreement between simulation and measurement by the ionization chamber. The interest of this simulation is then to use the possibilities of the Monte Carlo code to represent the alanine material in the simulation as well as its effect on the dose (and the volume effects due to its non-negligible dimensions). The LET values are also accessible thanks to these simulations in water and in pellet.

The first thing we had to do was create the alanine dosimeter in TOPAS. To do that, we needed to investigate alanine composition, which can change according to its brand. In our case, for an AERIAL pellet, the result of the composition investigation was 91,63 % pure alanine (L-alpha alanine) with H 7,91%, C 40,44%, N 15,72 %, O 35,91%. The binders are

6,37% EUDRAGIT NE 30D (compound with 2:1 molar ratio of Ethyl Acrylate and Methyl methacrylate) and 2% MYVATEX (90% ethylene and 10% vinyl acetate copolymer). The overall alanine density was 1.3789 g/cm^3 .

For the geometry, we have a 4 mm diameter and a 1.5 mm axial length. A more in-depth description of the TOPAS scripts that describe the dosimetry of the simulation can be found in Appendix A.8.

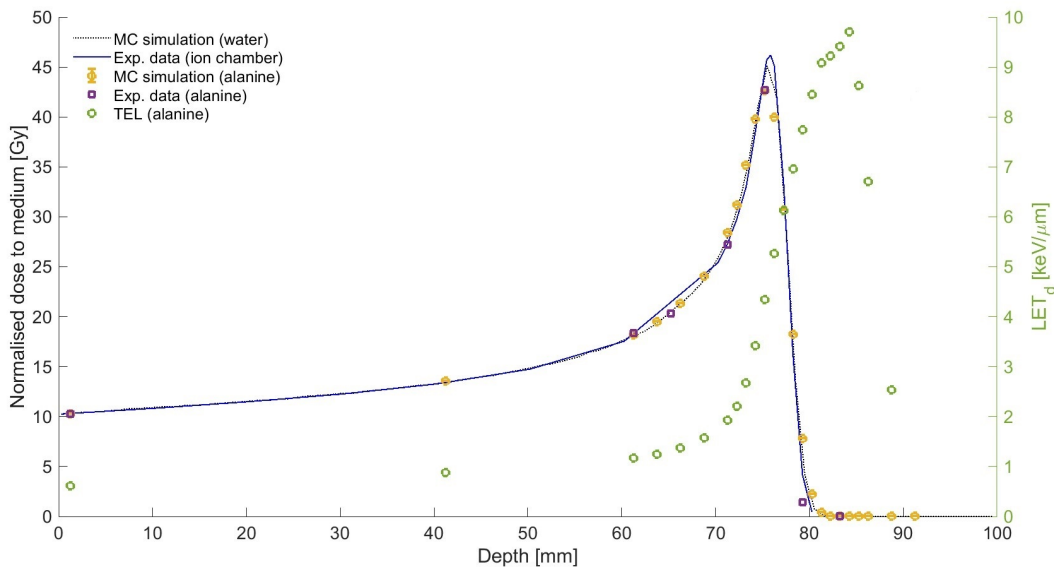


Figure 3.23: Bragg Peak shape for ion chamber, alanine and water, with LET (TEL) distribution in alanine and water.

In Figure 3.23, we can see the agreement between experimental and simulated data for both ion chamber, alanine and water. This analysis between dose measurement and LET distribution along the depth-dose curve illustrates the fact that the pellet dose is underestimated in the Bragg peak region, where the LET is increased. This underestimation is significant (more than 10%). LET (that in our simulation was dose-averaged) also behaves as expected, with an increase towards the end of the Bragg Peak, where energy deposition of the particle is at maximum, and a subsequent decrease in the distal part. Note that the LET distribution was averaged and estimated within the alanine pellet. The results are obtained with the script that can be found in Appendix A.7.

In order to correct for the energy (or LET) dependence of the alanine response, we then use data from Palmans et al. article [38], where the response of alanine is shown to be dependent on the type of radiation. To this end a relative effectiveness (RE) function for protons is introduced, defined as the ratio of the detector signals for the same amounts of absorbed dose by protons and by Co-60 gamma radiation. This function can be used to

correct the dose to the alanine obtained in our setup, especially in the Bragg peak's area. The function is the following:

$$RE(E_{\text{eff}}) = RE_0 + \frac{\Delta RE}{1 + e^{-C \cdot (\log(E_{\text{eff}}) - \log(E_m))}} \quad (3.3)$$

where RE_0 , ΔRE , C and E_m are tabulated parameters from experimental fits.

E_{eff} is the effective energy and was estimated as the average of the entrance and exit energies. It can be considered as a measure for the average LET of the protons in alanine. For example, if we can approximate total energy deposition inside alanine, the average LET was calculated as the incident energy, divided by the range in the continuous slowing down approximation (CSDA) and the energy of mono-energetic protons having the same LET was taken as effective energy. As seen in Palmans et al. paper, RE decreases with decreasing proton energy, or increasing LET. The Bragg peak is the region where protons slow down significantly and experience maximum LET. Indeed, Palmans [38] demonstrated that at proton energies below 20 MeV, RE drops significantly and the Bragg peak occurs at low proton energies (typically few MeV), where the RE of alanine decreases and this is in accordance to Monte Carlo simulations. The RE values corresponding to our setup are plotted in Figure 3.24.

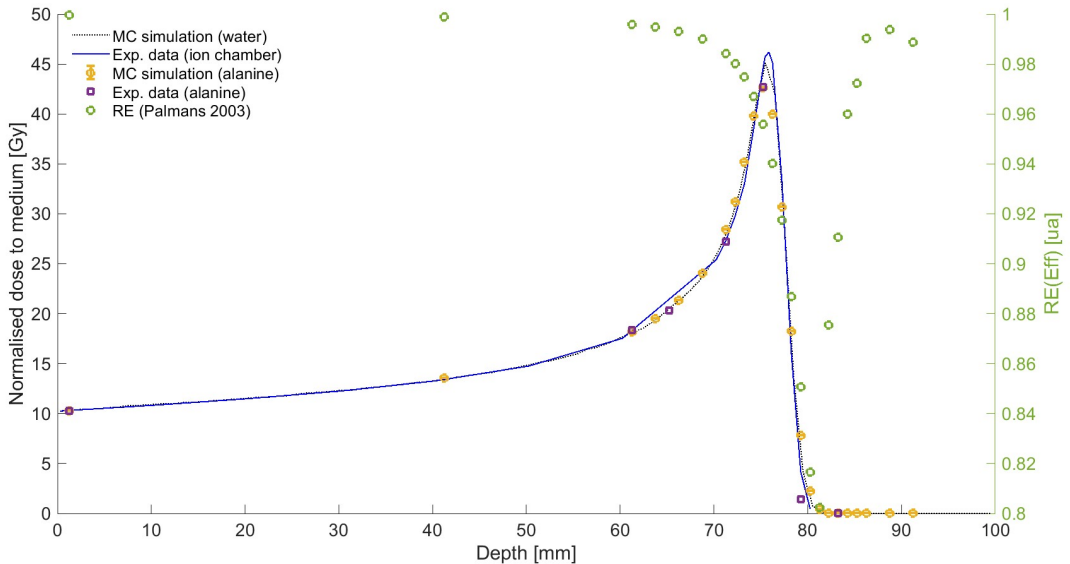


Figure 3.24: Bragg peak from experimental data and simulation with RE estimation.

3.3.5. Discussion and radical investigation

In this section we will try to interpret the data of the we obtained using already published work. After that, we will look into some new discussion topics, focusing on the production of radical species in alanine and what information they can give.

To start, Waligorski et al. [30] predicted that at high LET, radical formation in alanine becomes less efficient due to increased radical recombination before stabilization and more complex damage that doesn't contribute to ESR signals. Since protons at the Bragg peak have higher LET than at entrance, alanine's efficiency in detecting dose decreases, causing a reduction in RE. The paper notes that ionization chambers do not exhibit the same RE drop because their response is based on direct charge collection in air, which remains relatively independent of LET effects. This is in agreement with the fact that alanine dosimetry shows a lower dose at the Bragg peak than ion chambers. More generally, the underestimation of the dose at the Bragg peak as the LET increases is fairly common in solid detectors (scintillators, films, alanine, etc.), sometimes called quenching. This phenomena is yet not fully understood or explained. Indeed, there is no general-purpose model for taking this into account.

Monte Carlo simulations have also been implemented in studies to determine LET variations in proton fields using the X/Y ratio, like in the study by [39]. The X/Y describes the relative intensity of the main and satellite lines in the central peak of the irradiated alanine. This parameter reflects the degree of saturation of the spin system in the sample. X/Y ratios do not provide absolute LET values, so Monte Carlo codes can be useful to offer a comparison. The results of this study are still being investigated, although it was shown that X/Y is reduced at irradiation with higher LET relatively to a gamma-irradiation (e.g: Cobalt 60) and increased with increasing EPR power [37]. In the following figures we are able to see what we just described in a more intuitive way.

As Ivannikov et al. described [37], the most difference is observed in the central part of the spectra at 40 mW power, where the maxima of the two central lines for γ and α irradiated alanine dosimeter inverted by their amplitudes. Such inversion occurs between 10 and 20 mW for γ , and between 40 and 64 mW for α . This effect of the reduction of the mW power value, at which such inversion of the central lines amplitudes relatively to the spectra of γ irradiated alanine occurs, may serve as indicator of the exposure to alpha radiation. In the mixed radiation field, in which both α and γ radiation is presented, spectra induced by α and γ radiation are superimposed, and such shift will be observed, however at lower mw field values than for the pure alpha radiation. The similar effect also is expected at presence of other kinds of radiation with LET higher than that for γ .

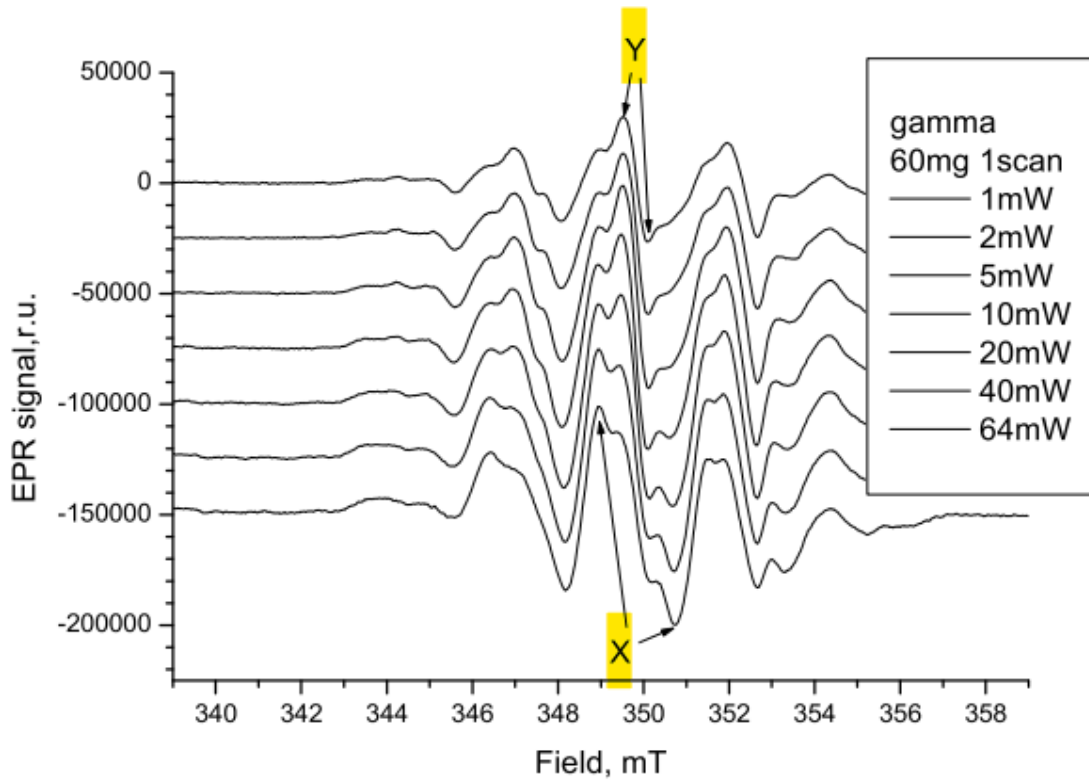


Figure 3.25: EPR spectra of γ irradiated alanine (low LET). The central narrow line is denoted by Y, the central wider line is denoted by X.

radiation. By the point of inversion of the amplitudes of X and Y components obtained from the measurements at different mW power, the presence of radiation exposure with increased LET can be qualitatively determined. The greater the power corresponding to the inversion point then the greater the contribution of the densely ionizing radiation.

In the paper by Ivannikov [37], it is proposed that different LET is linked to the creation of different radical concentrations. As we have already discussed, there can be three main species of radicals formed by irradiated alanine: R1, R2 and R3 (see section 2.1.6 and figure 3.28).

For an experimental investigation, we decided to take the pellets from our Bragg peak study 3.3.3, more in particular pellet number 1 (the entrance pellet) and pellet 25 (the pellet where the maximum resides) and to evaluate their radical spectra through the manipulation of the EPR parameters, as shown in Figure 3.28. Indeed, the radical EPR spectrum obtained from the alanine pellets depends on the applied microwave power. Thus, a new EPR recipe was created and it is reported in Appendix B, as Figure B.2.

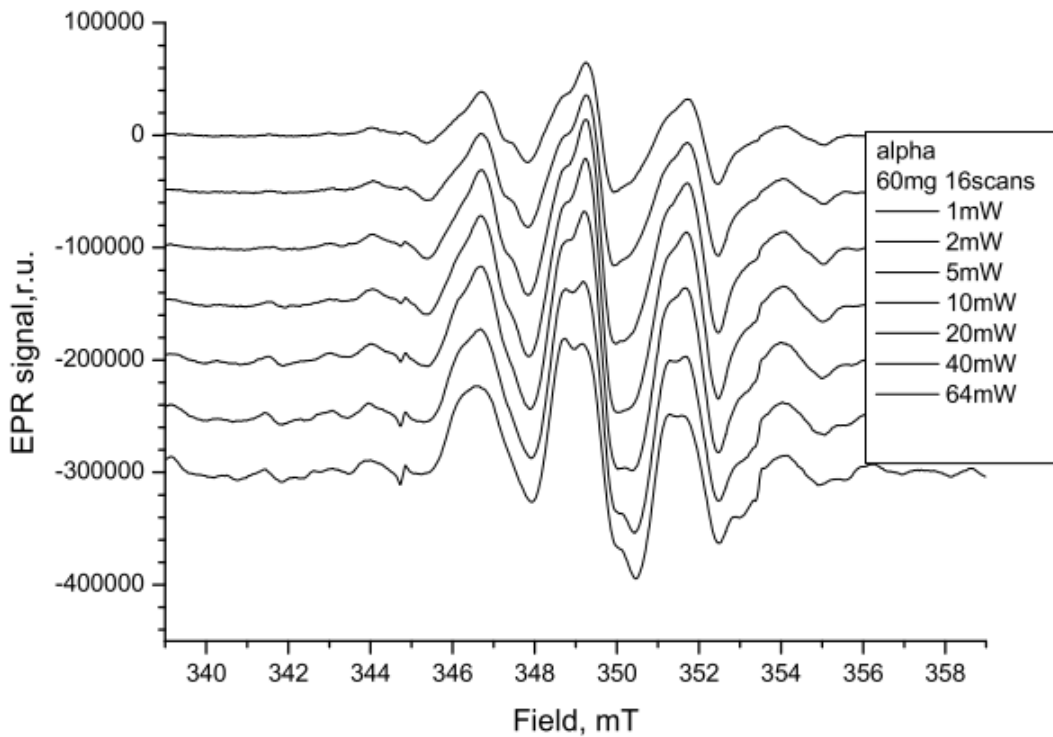


Figure 3.26: EPR spectra of α irradiated alanine (high LET).

The shape changes, as we can see in Figure 3.27, reflecting differences in radical concentration and possible variations in particle LET. We can see this with EPR because higher microwave power levels result in more pronounced spectral profile and potential saturation effects of the paramagnetic centers. The evaluation of LET with alanine radicals relies on the relationship between radical formation and radiation quality. Low LET radiation predominantly produces R1 radicals, characterized by a distinct peak in the EPR spectrum. High LET radiation, results in an increased presence of R2 and R3 radicals. The relative difference in concentrations will alter the shape of the spectra, keeping in mind that the overall spectra is a convolution of the one due to each radical. To get an idea of the different spectral shapes of different radicals, one could refer back to figure 2.14.

The ratio of the amplitudes (X/Y, already overviewed in the section 3.3.4) gives an indicator of LET, with high values corresponding to low linear energy transfer radiation and lower values indicating the presence of high linear energy transfer components. The saturation behavior of the spectrum with increasing microwave power also provides insights into radiation quality, as high linear energy transfer radiation induces a stronger saturation effect. Spectral decomposition (using for example the software EasySpin) can be used to quantify the contributions of different radical types to the overall signal. The fraction

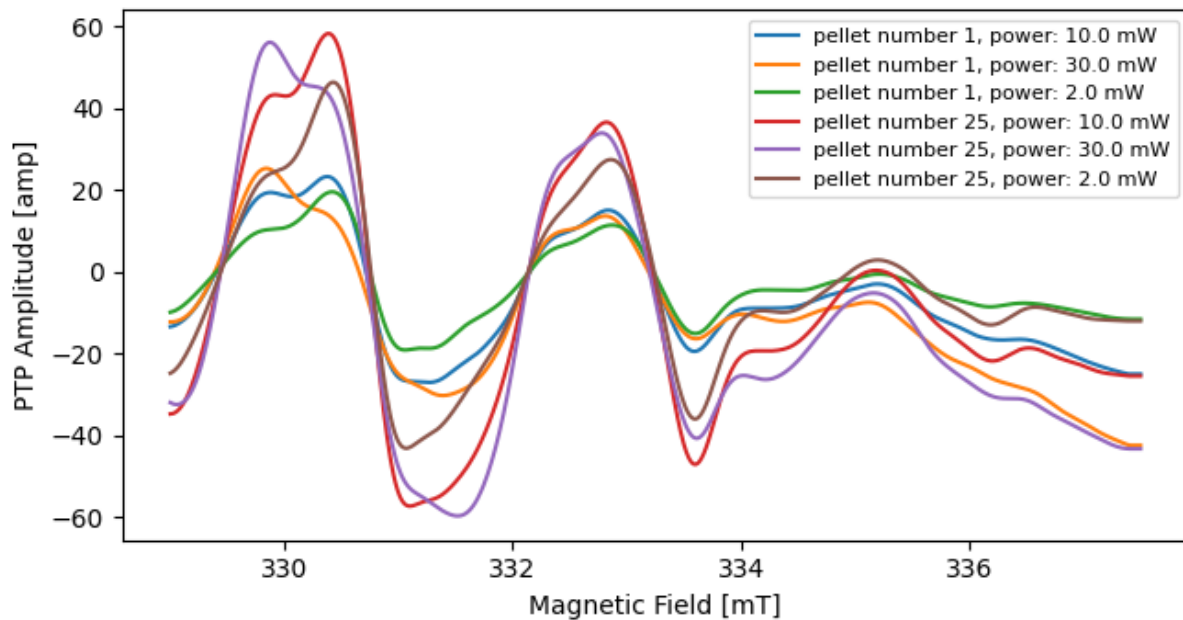


Figure 3.27: EPR spectra of alanine irradiated at different microwave power: 2 mW, 10 mW and 30 mW. Pellet 1 corresponds to entrance and pellet 25 to the peak. The spectra display signals related to different radicals.

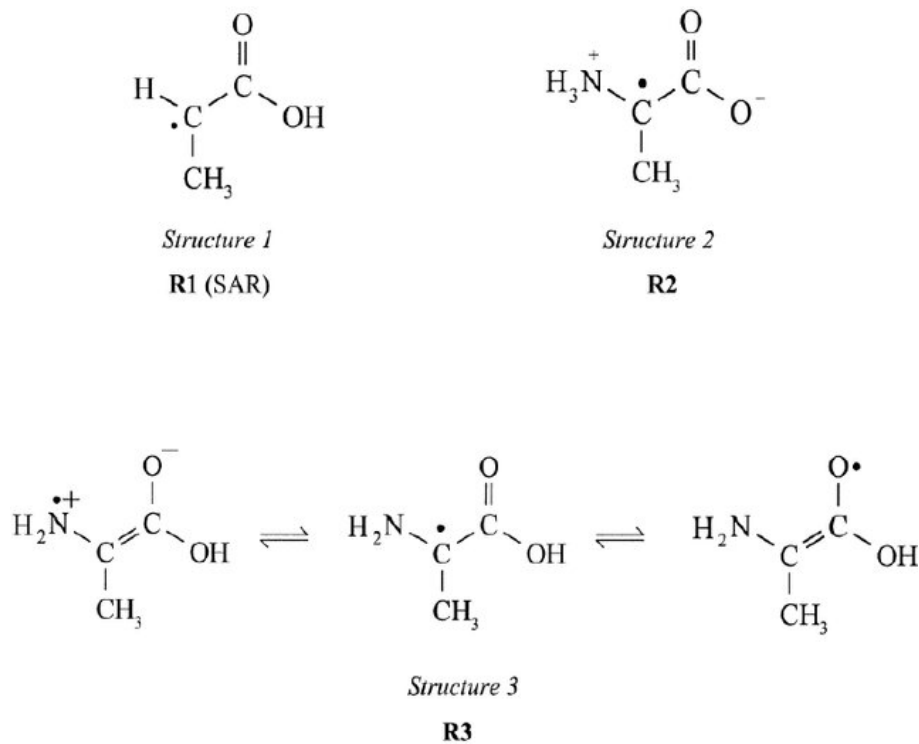


Figure 3.28: The structures of alanine radicals.

of R2 and R3 radicals increases with increasing LET, making it possible to establish a calibration curve by irradiating alanine with reference radiation sources of known LET. Comparing experimental spectra against this calibration allows for the estimation of linear energy transfer in unknown radiation fields. Similarly, we could monitor the evolution of LET of the particle while it travels in the medium: this is because Bragg peak region exhibits high LET that quickly drops in the distal part. Future experiments still need to prove this method. Ideally, the method could also be applied to neutron boron capture therapy or carbon ion therapy, where different radicals can help distinguish between γ induced and neutron induced radiolysis.

3.4. Conventional and FLASH electron beam irradiation

The aim of this section is to benchmark experimental data obtained in a FLASH electron beam, in particular using film and alanine dosimetry, known for their independence to dose rates.

3.4.1. Alanine and film dosimetry

An experiment performed Tuesday 14 May, 2024 provided pellets irradiated in FLASH and conventional conditions with 7 MeV electrons, using the FLASH electron LINAC at Institut Curie. An important element of dosimetry in FLASH conditions is that (for now) no absolute dosimeter exists for FLASH, except calorimetry which cannot be used easily in such an experimental setup. For example ion chambers, that are the standard for conventional irradiation, cannot function in FLASH conditions because of recombination effects and saturation issues. Indeed, we used radiochromic films (passive detector, just like alanine) and diamonds (active detectors, just like ion chambers) as references to estimate the dose delivered during the FLASH irradiation. We will still irradiate in conventional the detectors to compare and contrast the result to the ones obtained FLASH. We irradiated in a phantom slab the following dosimeters:

- PPC05 Ion chamber (small gap chamber, by IBA Dosimetry company);
- Diamond detector (FLASH diamond by PTW Dosimetry company);
- Markus chamber (small gap chamber by PTW Dosimetry company);
- Alanine pellet;
- Gafchromic film (EBT-XD type).

Films, ion chambers and diamonds were cross calibrated in the conventional dose-rate electron beam. Then, films and diamond detector were used to estimate the dose delivered with the FLASH beam. The alanine measurement was compared with the other detectors in the FLASH beam.

We will start by discussing the results of the last two. In conventional we repeated three times the irradiation of the alanine and film at 7 Gy. Results are reported in Table C.8, where err_{total} is the absolute error and it was found by taking into account both the uncertainty of the film (whose reading we will use as benchmark since conventional ion chambers cannot be used in FLASH) and the uncertainty related to reproducibility of the measurement. This helps us to calculate the σ_{total} , which was then multiplied by the normalized amplitude. A better explanation of the methods for data analysis is provided in section 2.2.6.

In particular, σ_{total} was obtained by $\sigma_{reproducibility}$ and σ_{film} , where the latter was found in Marroquin et al. paper [22], which states the dose ranges between 0 - 120 Gy, the overall uncertainty over different color channels is lower than 5.2%, so we will take this value for a conservative estimate of the uncertainty. During this measurement, the mean of the IM amplitude was 5446.71 [amplitude units], the standard deviation 53.82 [amplitude units], making the coefficient of variation equal to 0.98%.

In FLASH we repeated two times the irradiation of the alanine and film at 7 Gy, and two times the irradiation of alanine and film at 18 Gy. The data can be found in Table C.9.

The accelerator set-up dose (target dose), the film reading, and the normalized amplitudes figure are compared in 3.29, where the error bars represent the absolute uncertainty errors deriving from σ_{total} . The temperature of the cavity was 32°C for all of the measurement so we can exclude the variation of amplitude given by temperature which exists as shown in 3.1.4. All of the data was analyzed using the script that can be found in Appendix A.5.

In the next section, we will further compare these results to more dosimeters, in particular ion chambers and diamond.

3.4.2. Detectors inter-comparison

With respect to the experiment in section 3.4.1, the results of the inter-comparison of the different detectors that have been irradiated in conventional and FLASH are now presented. Like before, we irradiate the dosimeters with 7 MeV electrons.

In Figure 3.30 we can see the depth-dose profile comparison performed with the ion

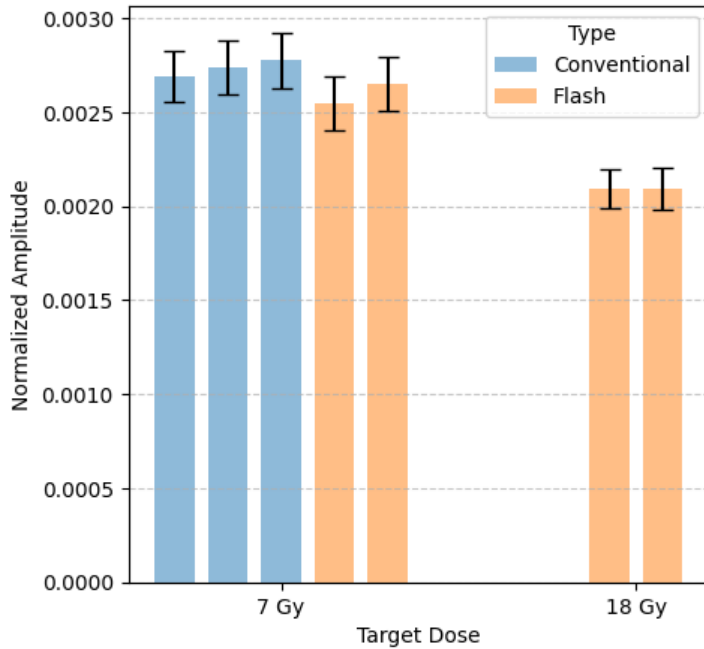


Figure 3.29: In this bar plot we see the comparison of conventional and FLASH irradiations on alanine, grouped in 7 Gy and 18 Gy of dose delivered by the beam.

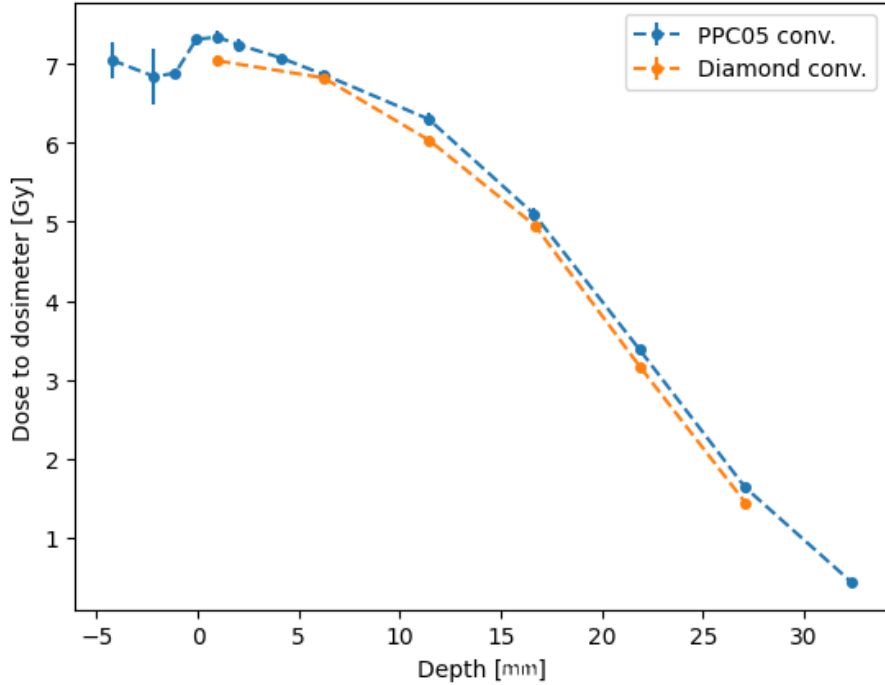


Figure 3.30: The diamond and ion chamber dose profiles.

chamber's and diamond detectors for a 7 Gy conventional irradiation, showing rather good agreement. Note the beam instabilities have a significant impact on the measurements

with ion chambers, causing a misalignment of points in the profile. This does not seem to occur for diamond. The data relative to this can be found in Table 3.1.

Table 3.1: Results of conventional irradiation on the active dosimeters.

Detector type	Measurement [Gy]	Uncertainty [%]
PPC05	7.73	0.15
Markus	7.67	0.70
Diamond	7.55	0.14

Where we remind that the doses and uncertainties in Table 3.1 are obtained thanks to the TRS2.1.3 standard method. We remind that the irradiation of the above dosimeters was performed at 6.295 mm water equivalent depth, and that some corrections were added (not detailed here), to correct for different equivalent thicknesses between the detectors, in particular the entrance window and different densities for the ionization chambers and diamond detectors, as well as their positioning in the solid water phantom plates.

Table 3.2: Results of conventional irradiation on passive dosimeters, with each film dosimeter paired with the alanine dosimeter it was irradiated with.

Film Dosimeter		Alanine Dosimeter	
Measurement [Gy]	Uncertainty (%)	Measurement [amp]	Uncertainty (%)
7.39	5.2	0.0026	0.9
7.50	5.2	0.0027	1.2
7.49	5.2	0.0027	1.7

In Table 3.2 are presented the doses obtained for the different detectors and beam conditions (in this case conventional dose rates). We used the film dosimeter EBT to have a benchmark for the alanine: since no calibration curve for 7 MeV electron was created in other experiments, it is not possible for us to interpolate a dose from the normalized amplitude measurement in the table (normalization was given with respect of film dose and internal marker measurement). The normalization procedure is performed also for the percentage error of alanine, while the percentage error for film is obtained from literature [22]. The irradiation of alanine and film was obtained at 5.68 cm water equivalent depth.

Let us now look at the results for FLASH. The 7 MeV electrons will first deliver 7 Gy (table 3.3) then 18 Gy (table 3.4).

The uncertainty for the diamond detector was considered to be the same as in conventional irradiation. In all cases the irradiation was performed at the before mentioned water equivalent depths. The results shown above were obtained with the script that can be

Table 3.3: Results of FLASH 7 Gy irradiation.

Detector type	Measurement	Uncertainty [%]
Diamond	7.44 Gy	0.14
Film	7.17 Gy	5.2
	7.15 Gy	5.2
Alanine	0.0025 [amp]	2.6
	0.0026 [amp]	2.2 %

Table 3.4: Results of FLASH for 18 Gy irradiation.

Detector type	Measurement	Uncertainty [%]
Diamond	18.56 Gy	0.14
Film	19.94 Gy	5.2
	19.92 Gy	5.2
Alanine	0.0020 [amp]	0.5
	0.0020 [amp]	1.4

found in Appendix A.6. Overall, the agreement is correct between the detectors with less than 5 % maximum difference for all conditions. The difference between diamond and films is larger than for alanine, maybe because the larger uncertainty of the film that can be due to calibration or improper corrections for the film material to water equivalence. We remind, on the other hand, that the value for the uncertainty of film is found from literature [22], where we chose the highest value, thus more conservative. Our results are in agreement with what is reported in Ashraf et al. paper [40] reports, which gives an interesting visualization of detector's inter-comparison. We can find such visualization in Appendix B, in Figure B.3.

4 | Conclusion

The results presented in this thesis provide a general characterization of alanine as a dosimeter for conventional and FLASH radiotherapy. A comparison with other dosimeters, mainly ion chambers, films and diamond detectors was offered to evaluate alanine's relative performance.

We began by understanding the complex operation of the equipment used for EPR (for which the many parameters can modify the read signal) and, above all, all the uncertainties obtained during the measurements. We thus characterized the evolution and dependence of the EPR signal on temperature, microwave power, number of scans, etc. used during acquisition. Our findings demonstrated the feasibility of the specifically optimized recipe for the EPR system that we used during our research, while also offering prospects on how to further refine it for future applications.

During our research, we also developed a standardized protocol for alanine irradiation, storage, and waterproofing. We tested it across multiple experiments and irradiations to ensure reproducibility, accuracy and convenience. Several experiments (albeit limited due to access to complex and/or clinical irradiation machines) have been carried out using high-energy protons (100 and 226 MeV), and electrons between 5 and 7 MeV. An electron beam in FLASH mode (ultra-high dose-rate) was also used to begin comparing detector responses.

To facilitate data analysis, Python and Matlab scripts were developed to provide a streamlined workflow for future research.

The reproducibility of alanine dosimetry was evaluated and confirmed in each experiment, and calibration curves obtained from different beam energies and in water and plastic phantoms were compared using statistical methods to assess their consistency.

An inter-comparison of alanine, films, ion chambers, and diamond detectors was performed in conventional and FLASH irradiation (where applicable). This highlighting differences in response at different dose and dose-rates, but also showing promising results in quite different beams and conditions.

Lastly, LET (Linear Energy Transfer) behavior for alanine was demonstrated using a proton beam in a Bragg Peak experiment to characterize its response. The result showed significant underestimation of the dose, aligning with literature findings. This was obtained both using experimental data and Monte Carlo simulations in order to interpret the results of the experiment. For this aim, we modeled the alanine dosimeter and setup accurately in TOPAS/Geant4 toolkit.

4.1. Future developments

Alanine dosimetry for FLASH-RT is still in its developing stages, with ongoing research exploring its advantages and limitations.

In the close future, projects such as FRATHEA (Flash Radiation Therapy Electron Acceleration) using very high energy electron (VHEE) technology, a collaboration between Institut Curie and CEA (Commissariat à l'Énergie Atomique), aim to advance FLASH to preclinical studies. This project, among many others, will offer plenty of occasions for the further characterization of alanine as a useful ultra-high dose-rate dosimeter.

In addition, efforts are being made to make alanine dosimetry more versatile. The IRSN, now called ASNR, has developed patents for the waterproofing of alanine and the production of alanine pellets in different shapes and sizes, facilitating its use in in-vivo experimentation.

Alanine dosimetry is not limited to the particles explored in this study. Indeed, research is also investigating its application as a neutron dosimeter, or for applications in proton-boron capture therapy, a new approach in radiation oncology that wants to bring the characteristics of neutron-boron capture without the need of reactors.

Another exciting avenue for alanine dosimetry is MRI-guided radiotherapy (for example MRI-LINACs), as magnetic fields are known to modify the response of some detectors.

These future developments will contribute to the continued advancement of alanine dosimetry, widening its applications and strengthening its role as a reliable tool in emerging radiation technologies.

Bibliography

- [1] V. Favaudon, L. Caplier, V. Monceau, et al. Ultrahigh dose-rate flash irradiation increases the differential response between normal and tumor tissue in mice. *Science Translational Medicine*, 6(245):245ra93, 2014. Published correction appears in Sci Transl Med. 2019 Dec 18;11(523):eaba4525. doi: 10.1126/scitranslmed.aba4525.
- [2] ICRP. 1970 recommendations of the international commission on radiological protection. *ICRP Publication 16*, 1970.
- [3] ICRP. 1990 recommendations of the international commission on radiological protection. *ICRP Publication 60*, 1991.
- [4] Fredrik Kalholm, Leszek Grzanka, Erik Traneus, and Niels Bassler. A systematic review on the usage of averaged let in radiation biology for particle therapy. *Radiotherapy and Oncology*, 161:211–221, 2021.
- [5] Francesco Romano, Claude Bailat, Patrik Gonçalves Jorge, Michael Lloyd Franz Lerch, and Arash Darafsheh. Ultra-high dose rate dosimetry: Challenges and opportunities for flash radiation therapy. *Medical Physics*, 49(7):4912–4932, 2022.
- [6] B. Rothwell, M. Lowe, E. Traneus, M. Krieger, and J. Schuemann. Treatment planning considerations for the development of flash proton therapy. *Radiotherapy and Oncology*, 175:222–230, 2022.
- [7] S. Deffet, V. Hamaide, and E. Sterpin. Definition of dose rate for flash pencil-beam scanning proton therapy: A comparative study. *Medical Physics*, 50(9):5784–5792, 2023.
- [8] Jean Bourhis, Wendy Jeanneret Sozzi, Patrik Gonçalves Jorge, Olivier Gaide, Claude Bailat, Frédéric Duclos, David Patin, Mahmut Ozsahin, François Bochud, Jean-François Germond, Raphaël Moeckli, and Marie-Catherine Vozenin. Treatment of a first patient with flash-radiotherapy. *Radiotherapy and Oncology*, 139:18–22, 2019. FLASH radiotherapy International Workshop.

- [9] Charles L. Limoli and Marie-Catherine Vozenin. Reinventing radiobiology in the light of flash radiotherapy. *Annual Review of Cancer Biology*, 7:1–21, 2023.
- [10] Xu Cao et al. Quantification of oxygen depletion during flash irradiation in vitro and in vivo. *International Journal of Radiation Oncology, Biology, Physics*, 111(1):240–248, 2021.
- [11] Daria Boscolo, Emanuele Scifoni, Marco Durante, Michael Krämer, and Martina C. Fuss. May oxygen depletion explain the flash effect? a chemical track structure analysis. *Radiotherapy and Oncology*, 162:68–75, 2021.
- [12] Ramin Abolfath, David Grosshans, and Radhe Mohan. Oxygen depletion in flash ultra-high-dose-rate radiotherapy: A molecular dynamics simulation. *Medical Physics*, 47(12):6551–6561, November 2020.
- [13] *Absorbed Dose Determination in External Beam Radiotherapy*. Number 398 (Rev. 1) in Technical Reports Series. INTERNATIONAL ATOMIC ENERGY AGENCY, Vienna, 2024.
- [14] Harrison J Menzel HG Clement CH ICRP, Eckerman K. Icrp publication 119: Compendium of dose coefficients based on icrp publication 60. *Annals of the ICRP*, 41(Suppl 1):1–130, 2012. Published correction appears in Ann ICRP. 2013 Aug;42(4):345.
- [15] Jean-Claude Nenot, Jean Brenot, Dominique Laurier, Alain Rannou, and Dominique Thierry. *ICRP Publication 103: The 2007 Recommendations of the International Commission on Radiological Protection*. International Commission on Radiological Protection, France, 2009. INIS-FR-18-0662.
- [16] Glen Knoll. *Radiation Detection and Measurement (4th ed.)*. John Wiley, Hoboken, NJ, 2010.
- [17] Runqiu Gu, Jianlin Wang, Pan Wang, Xin Mao, Binwei Lin, Wanchao Tan, Xiaobo Du, Feng Gao, and Tingting Wang. Alanine/electron spin resonance dosimetry for flash radiotherapy. *Radiation Physics and Chemistry*, 225:112113, 2024.
- [18] F. Gómez, D. M. Gonzalez-Castaño, N. G. Fernández, et al. Development of an ultra-thin parallel plate ionization chamber for dosimetry in flash radiotherapy. *Medical Physics*, 49(7):4705–4714, 2022.
- [19] Marco Marinelli, Giuseppe Felici, Federica Galante, Alessia Gasparini, Lucia Giuliano, Sophie Heinrich, Matteo Pacitti, Giuseppe Prestopino, Verdi Vanreusel, Dirk Verellen, Claudio Verona, and Gianluca Verona Rinati. Design, realization, and char-

- acterization of a novel diamond detector prototype for flash radiotherapy dosimetry. *Medical Physics*, 49(3):1902–1910, 2022.
- [20] B. R. Muir and D. W. Rogers. Monte carlo calculations of electron beam quality conversion factors for several ion chamber types. *Medical Physics*, 41(11):111701, 2014.
- [21] Leon Dunn, Guy Godwin, James Hellyer, and Xiaolei Xu. A method for time-independent film dosimetry: Can we obtain accurate patient-specific qa results at any time postirradiation? *Journal of Applied Clinical Medical Physics*, 23(3):e13534, 2022.
- [22] Elsa Y. León Marroquin et al. Evaluation of the uncertainty in an ebt3 film dosimetry system utilizing net optical density. *Journal of Applied Clinical Medical Physics*, 17(5):466–481, Sep 2016.
- [23] Tania Santos, Tiago Ventura, and Maria do Carmo Lopes. A review on radiochromic film dosimetry for dose verification in high energy photon beams. *Radiation Physics and Chemistry*, 179:109217, 2021.
- [24] Mojgan Z. Heydari, Eirik Malinen, Eli O. Hole, and Einar Sagstuen. Alanine radicals. 2. the composite polycrystalline alanine epr spectrum studied by endor, thermal annealing, and spectrum simulations. *Journal of Physical Chemistry A*, 106(38):8971 – 8977, 2002. Cited by: 78.
- [25] Zetian Yang, Henk Vrielinck, Luiz Jacobsohn, Philippe Smet, and Dirk Poelman. Passive dosimeters for radiation dosimetry: Materials, mechanisms, and applications. *Advanced Functional Materials*, 34:2406186, 07 2024.
- [26] Yasser S. Soliman, Ramy Amer Fahim, Paolo Pellicoli, Michael Krisch, W.B. Beshir, A.A. Abdel-Fattah, Muhammad G. Abd El-Moghny, and Mohamed S. El-Deab. Comparison of the dosimetric response of two sr salts irradiated with 60co -rays and synchrotron x-rays at ultra-high dose rate. *Radiation Physics and Chemistry*, 208:110923, 2023.
- [27] Maude Gondré, Patrik Gonçalves Jorge, Marie-Catherine Vozenin, Jean Bourhis, François Bochud, Claude Bailat, and Raphaël Moeckli. Optimization of Alanine Measurements for Fast and Accurate Dosimetry in FLASH Radiation Therapy. *Radiation Research*, 194(6):573 – 579, 2020.
- [28] Gareth R Eaton, Sandra Eaton, David Barr, and Ralph Weber. *Quantitative EPR*. 01 2010.

- [29] Vitaly Nagy. Accuracy considerations in epr dosimetry. *Applied Radiation and Isotopes*, 52(5):1039–1050, 2000.
- [30] M.P.R. Waligórski, G. Danialy, Kim Sun Loh, and R. Katz. The response of the alanine detector after charged-particle and neutron irradiations. *International Journal of Radiation Applications and Instrumentation. Part A. Applied Radiation and Isotopes*, 40(10):923–933, 1989.
- [31] Araceli Gago-Arias, Diego González-Castaño, Faustino Gómez, Eva Peteiro, Consuelo Lodeiro, and Juan Pardo-Montero. Development of an alanine dosimetry system for radiation dose measurements in the radiotherapy range. *Journal of Instrumentation*, 10:T08004, 08 2015.
- [32] *Accuracy Requirements and Uncertainties in Radiotherapy*. Number 31 in Human Health Series. INTERNATIONAL ATOMIC ENERGY AGENCY, Vienna, 2016.
- [33] Eric Jones, Travis Oliphant, Pearu Peterson, et al. SciPy: Open source scientific tools for Python, 2001–.
- [34] International Organization for Standardization and ASTM International. ISO/ASTM 51607:2013 - Standard Practice for Use of the Alanine-EPR Dosimetry System, 2013.
- [35] L. Giuliano et al. Title of the paper.
- [36] Anthony Bonfrate et al. Monte carlo modeling of a commercial machine and experimental setup for flash-minibeam irradiations with electrons. *Medical Physics*, 52(2):1224–1234, 2025.
- [37] A.I. Ivannikov, A.M. Khailov, S.P. Orlenko, V.F. Stepanenko, F. Trompier, and K. Sh Zhumadilov. Formation of different types of paramagnetic centers in the alanine dosimeters exposed to alpha and gamma radiation - study by epr spectroscopy. *Radiation Measurements*, 140:106467, 2021.
- [38] Hugo Palmans. Effect of alanine energy response and phantom material on depth dose measurements in ocular proton beams. *Technology in Cancer Research & Treatment*, 2(6):579–586, 2003. PMID: 14640769.
- [39] Barbara Michalec, Liliana Stolarczyk, Niels Bassler, Marzena Rydygier, Anna Spaleńiak, and Renata Kopeć. Alanine dosimeters for let measurement in proton radiotherapy. *Radiation Measurements*, 175:107150, 2024.
- [40] Muhammad Ramish Ashraf, Mahbubur Rahman, Rongxiao Zhang, Benjamin B.

Williams, David J. Gladstone, Brian W. Pogue, and Petr Bruza. Dosimetry for flash radiotherapy: A review of tools and the role of radioluminescence and cherenkov emission. *Frontiers in Physics*, 8, August 2020.

A | Appendix A

A.1. Film reading script

```

1 close all;
2 clearvars;
3 warning off all;
4 clc;
5
6 % Define path to images
7 pathwithimage = ['R:\CPO\ETUDIANTS\JULIEN','\Manipes\'];
8 chp = 10;

```

```

1 % Select and load the background image
2 [filename_bck, datadir_bck] = uigetfile([pathwithimage,'*.tif'], 'Select
  .tif image as background');
3 [B, mapb] = imread(fullfile(datadir_bck, filename_bck));
4 [pb, qb, rb] = size(B);
5 X1b = [0:passss:passss*(pb-1)]; Y1b = [0:passss:passss*(qb-1)];
6 tmpb = B(:,:,1); % Red channel of background image
7 fhbck = figure('Name', 'Select one point for background', 'Position',
  [100, 100, qb, pb]);
8 imagesc(tmpb);
9 [POSXb_exp, POSYb_exp] = getpts;
10 I_Bckg = mean(mean(tmpb(POSYb_exp-chp:POSYb_exp+chp, POSXb_exp-chp:
  POSXb_exp+chp)));

```

```

1 % Select and load the Gafchromic film image
2 [filename, datadir] = uigetfile([pathwithimage,'*.tif'], 'Select.tif
  image');
3 [A, map] = imread(fullfile(datadir, filename));
4 [p, q, r] = size(A);
5 X1 = [0:passss:passss*(p-1)]; Y1 = [0:passss:passss*(q-1)];
6 tmp = A(:,:,1); % Red channel of the image
7 fh1 = figure('Name', 'Select one point', 'Position', [100, 100, q, p]);
8 imagesc(tmp);
9 [POSX_exp, POSY_exp] = getpts;

```

```
10 I_exp = mean(mean(tmp(POSY_exp-chp:POSY_exp+chp, POSX_exp-chp:POSX_exp+
    chp)));
```

```
1 % Compute net optical density (netOD)
2 a = 11.61; b = 52.3; c = 2.861; d = 0;
3 I_unexp = 46648.3;
4 netOD = log10((I_unexp - I_Bckg) / (I_exp - I_Bckg));
```

```
1 % Convert image to dose map
2 for i = 1:p
3     for j = 1:q
4         tmpD(i,j) = log10((I_unexp - I_Bckg) / (single(tmp(i,j)) -
    I_Bckg));
5     end
6 end
7 tmpD(tmpD<0) = 0;
8 for i = 1:p
9     for j = 1:q
10        tmpD(i,j) = d + a*tmpD(i,j) + b*tmpD(i,j).^c;
11    end
12 end
```

```
1 % Display dose image
2 figure('Name','Dose_Image','Position', [200, 100, q+20, p]);
3 imagesc(tmpD);
4 caxis([0 23]);
5 xlabel('Off-axis distance [mm]'); ylabel('Off-axis distance [mm]');
6 title('Dose Distribution');
```

```
1 check_export = checkboxDialog();
2 if check_export
3     [filename_dicom, datadir_dicom] = uigetfile([pathwithimage,'*.dcm'],
    'Select a DICOM file as a template');
4     dicom_path = [datadir_dicom, filename_dicom];
5     metadata = dicominfo(dicom_path);
6     outputFileName = [filename(1:end-4), '.dcm'];
7     dicomwrite(tmpD, outputFileName, metadata, 'CreateMode', 'Copy');
8 end
```

A.2. Saturation curve fit

```
1 import pandas as pd
2 import numpy as np
```

```

3  from scipy.optimize import curve_fit
4  import seaborn as sns
5  import matplotlib.pyplot as plt
6
7 %matplotlib inline

1 data = pd.read_csv("psat104.csv", sep=";", usecols=["SqrtMicrowavePower"
2   , "MeasurementParam.Amplitude"])
3
4 def func(P, A_0, P_sat, exp):
5     return A_0 * P * (1 + P**2/P_sat) ** (-exp)
6
7 x = data["SqrtMicrowavePower"]
8 y = data["MeasurementParam.Amplitude"]

1 popt, pcov = curve_fit(func, x, y, p0=(10, 4, 1), bounds=((0, 0, 0),
2   .inf, np.inf, np.inf)))
3
4 A_0, P_sat, exp = popt
5
6 y_pred = func(x, A_0, P_sat, exp)
7 residuals = y - y_pred
8
9 ss_res = np.sum(residuals**2)
10 ss_tot = np.sum((y - np.mean(y))**2)
11 r_squared = 1 - (ss_res / ss_tot)

12 print("Fit Parameters:")
13 print(f"A_0={A_0:.2f}")
14 print(f"P_sat={P_sat:.2f}")
15 print(f"exp={exp:.2f}")
16 print(f"R^2={r_squared:.4f}")

1 x_bin = np.linspace(min(x), max(x), 1000)
2 y_fit = func(x_bin, A_0, P_sat, exp)
3
4 plt.figure(figsize=(10, 6))
5 sns.scatterplot(data=data, x="SqrtMicrowavePower", y="MeasurementParam.
6   Amplitude", color="blue", label="Experimental Data")
7 sns.lineplot(x=x_bin, y=y_fit, color="red", label=f"Fit (R^2={r_squared:.4f})")
8
9 plt.xlabel("Squared Microwave Power [mW]", fontsize=12)
10 plt.ylabel("Amplitude [amp]", fontsize=11)
11 plt.legend(fontsize=12)

```

```
11 | plt.show()
```

A.3. Calibration curve

```

1 from google.colab import drive # Grant access to your Google Drive
2 drive.mount('/content/drive', force_remount=True)

1 data_path = "drive/MyDrive/tesi_magistrale/samplefolder2" # Mount the
   folder containing .csv files

1 import pandas as pd
2 import numpy as np
3 import seaborn as sns
4 import matplotlib.pyplot as plt
5 from matplotlib import rcParams
6 import math
7 from statistics import stdev, mean
8 import matplotlib.ticker as mticker
9 import scipy
10 from scipy.stats import linregress

1 rcParams['figure.figsize'] = 7.5, 3.75

1 def custom_print(*args):
2     formatted_args = [f"{x:.2f}" if isinstance(x, float) else x for x in
           args]
3     print(*formatted_args)

1 no_dose = pd.read_csv(f"{data_path}/proton_conv_100MeV_0Gy.csv", sep=";"
   , skiprows=88, names=["magnetic_field", "amplitude"])
2 sns.lineplot(no_dose, x="magnetic_field", y="amplitude", label='0 Gy')

1 doses = [10, 20, 30, 40]
2 samples = [1, 2, 3, 4, 5, 6, 7, 8, 9, 10]
3 samples_string = [f"{s}" for s in samples]
4 doses_string = [f"{d}" for d in doses]

5
6 mean_list = []
7 stdev_list = []

8
9 for d in doses_string:
10     amplitude_list = []
11     for s in samples_string:
12         df = pd.read_csv(f"{data_path}/proton_conv_100MeV_{d}Gy_{s}.csv"
           , sep=";", skiprows=3600, engine='python', skipfooter=4900,
           names=["magnetic_field", "amplitude"])

```

```

13     no_dose = pd.read_csv(f"{data_path}/proton_conv_100MeV_0Gy.csv",
14         sep=";", skiprows=3600, engine='python', skipfooter=4900,
15         names=["magnetic_field", "amplitude"])
16     df["relative_amplitude"] = df["amplitude"] - no_dose["amplitude"]
17
18     amplitude_list.append((df["relative_amplitude"].max() - df[
19         "relative_amplitude"].min()))
20
21     std = stdev(amplitude_list)
22     err = std / mean(amplitude_list) * 100
23     mean_list.append(mean(amplitude_list))
24     stdev_list.append(std)
25     custom_print("Coefficient_of_variation_for", d, "Gy=", err, "%")
26
27 custom_print("Mean_amplitudes_vector_is", mean_list, "Standard_deviations"
28             "vector_is", stdev_list)

```

```

1 import matplotlib.pyplot as plt
2 from matplotlib import rcParams
3
4 plt.errorbar(doses, mean_list, yerr=stdev_list, fmt='o', capsizes=5,
5               ecolor='red')
6 plt.xlabel('Absorbed_dose_in_water[Gy]')
7 plt.ylabel('Amplitude[amp]')
8 plt.title('Calibration_Curve')
9 plt.grid(True)
10 plt.show()

```

```

1 slope, intercept, r_value, p_value, std_err = linregress(doses,
2               mean_list)
3 r_squared = r_value**2
4
5 print(f"R^2 for the linear fit: {r_squared:.4f}")
6
7 x_fit = np.linspace(min(doses), max(doses), 100)
8 y_fit = slope * x_fit + intercept
9
10 plt.errorbar(doses, mean_list, yerr=stdev_list, fmt='o', capsizes=5,
11               ecolor='red', label='Data with errors')
12 plt.plot(x_fit, y_fit, 'b--', label=f'Fit: R^2={r_squared:.4f}')
13 plt.xlabel('Absorbed_dose_in_water[Gy]')
14 plt.ylabel('Amplitude[amp]')
15 plt.legend()
16 plt.show()

```

```
1 unknown_amplitude = [120, 130, 140] # Example unknown amplitude values
2 mean_unknown = mean(unknown_amplitude)
3 std_unknown = stdev(unknown_amplitude)
4
5 dose_unknown = (mean_unknown - intercept) / slope
6 dose_uncertainty = std_unknown / slope
7
8 print(f"The unknown dose is {dose_unknown:.2f} Gy with uncertainty {dose_uncertainty:.2f} Gy")
```

```
1 plt.errorbar(doses, mean_list, yerr=stdev_list, fmt='o', capsized=5,
2               ecolor='red', label='Calibration Data')
3 plt.axvline(x=dose_unknown, color='r', linestyle='--', label=f'Unknown
4 Dose = {dose_unknown:.2f} Gy')
5
6 plt.xlabel('Absorbed dose in water [Gy]')
7 plt.ylabel('Amplitude [amp]')
8 plt.legend()
9 plt.show()
```

A.4. Bragg Peak curve

```

1 from google.colab import drive # Grant access to your Google Drive
2 drive.mount('/content/drive', force_remount=True)

1 data_path = "drive/MyDrive/tesi_magistrale/samplefolder" # Mount the
   folder containing .csv files

1 import pandas as pd
2 import numpy as np
3 import seaborn as sns
4 import matplotlib.pyplot as plt
5 from matplotlib import rcParams
6 import math
7 from statistics import stdev, mean
8 import matplotlib.ticker as mticker

1 rcParams['figure.figsize'] = 7.5, 3.75

1 thickness = 2.4 # mm
2 diameter = 4 # mm

1 no_dose = pd.read_csv(f"{data_path}/0Gy.csv", sep=";", skiprows=88,
   names=["magnetic_field", "amplitude"])
2 sns.lineplot(no_dose, x="magnetic_field", y="amplitude", label='0 Gy')
3 plt.title('Blank (unirradiated) pellet EPR spectrum')

1 pelletIM = [1,2,3,4,5,6,7,8]
2 im_string = [f"{i}" for i in pelletIM]

3 amplitudeim_list = []
4 for i in im_string:
5     af = pd.read_csv(f"{data_path}/Particle_conv_100MeV_14Gyenter_{i}_IM
        .csv", sep=";", skiprows=4422, names=["magneticim_field",
        "amplitudeim"])
6     amplitudeim_list.append(af["amplitudeim"].max() - af["amplitudeim"].
      min())
7
8
9 print("Internal markers amplitude =", amplitudeim_list)
10 std = stdev(amplitudeim_list)
11 print("Standard deviation =", std)

1 pellet = [1,2,3,4,5,6,7,8]
2 pellet_string = [f"{d}" for d in pellet]

```

```

3  amplitude_list = []
4
5  for d in pellet_string:
6      df = pd.read_csv(f"{data_path}/Particle_conv_100MeV_14Gyenter_{d}.
7          csv", sep=";", skiprows=3000, engine='python', skipfooter=3000,
8          names=["magnetic_field", "amplitude"])
9  no_dose = pd.read_csv(f"{data_path}/0Gy.csv", sep=";", skiprows
10     =3000, engine='python', skipfooter=2000, names=["magnetic_field",
11     "amplitude"])
12 df["relative_amplitude"] = df["amplitude"] - no_dose["amplitude"]
13 amplitude_list.append(df["relative_amplitude"].max() - df["relative_
14     amplitude"].min())
15
16 sns.lineplot(df, x="magnetic_field", y="relative_amplitude", label=f"
17     Pellet_n_{d}")
18 plt.xlabel("Magnetic_field[mT]")
19 plt.ylabel("PTP_Amplitude[amp]")
20 plt.legend(prop={'size': 8})
21 plt.show()

```

```

1  depth = [0, 6, 6.4, 7, 7.4, 7.8, 8.2, 8.6]
2  plt.plot(depth, amplitude_list)
3  plt.xlabel("Depth_in_the_water[cm]")
4  plt.ylabel("Peak_to_Peak_Amplitude")
5  plt.title("Bragg_Peak")
6  plt.xticks(depth[::1])
7  plt.show()

```

```

1  ampnormal_list = [amp / IM for amp, IM in zip(amplitude_list,
2      amplitudeim_list)]
3  ampnormal_list = [x / thickness for x in ampnormal_list]
4
5  stdnormal = [std / IM for std, IM in zip(amplitudeim_list,
6      amplitudeim_list)]
7  stdnormal = [x / thickness for x in stdnormal]
8  stdnormal = mean(stdnormal)
9
10 print("Normalized_PTP_amplitudes", ampnormal_list, "with_reproducibility
11     _std", stdnormal)

```

```

1  doses = [0, 5, 10, 20, 30, 40]
2  mean_list = [0, 45.71, 88.23, 172.71, 259.17, 348.52]
3  mean_list = [x / IM for x, IM in zip(mean_list, amplitudeim_list)]
4  mean_list = [x / thickness for x in mean_list]
5

```

```

6 doses_list = []
7 for index, amplitude in enumerate(ampnormal_list):
8     dose_unknown = np.interp(amplitude, mean_list, doses)
9     doses_list.append(dose_unknown)
10
11 plt.plot(depth, doses_list, marker='o', linestyle='--', color='b', label=
12     'Alanine Data')
13 plt.xlabel("Depth in the water [cm]")
14 plt.ylabel("Interpolated Dose to Alanine")
15 plt.legend()
16 plt.show()

```

```

1 data = pd.read_csv(f"{data_path}/ionchambercalibrationBP.csv", sep=";",
2     skiprows=1, names=["Depth", "Dose"])
3 depth_ion = data['Depth']
4 dose_ion = data['Dose']
5
6 plt.plot(depth_ion, dose_ion, marker='o', linestyle='--', color='r',
7     label='Ion Chamber Data')
8 plt.plot(depth, doses_list, marker='o', linestyle='--', color='b', label=
9     'Alanine Data')
10
11 plt.xlabel("Depth in the water [cm]")
12 plt.ylabel("Interpolated Dose to Alanine [Gy]")
13 plt.legend()
14 plt.show()

```

```

1 y_unknown = mean(ampnormal_list)
2 sigma_y = stdnormal
3
4 a = 0.002836
5 sigma_a = 0.000016
6 b = 0.000233
7 sigma_b = 0.000356
8
9 x_unknown = (y_unknown - b) / a
10
11 term1 = sigma_y**2 / a**2
12 term2 = sigma_b**2 / a**2
13 term3 = ((y_unknown - b)**2 * sigma_a**2) / a**4
14
15 sigma_max = np.sqrt(term1 + term2 + term3)
16
17 print(f"Total uncertainty (sigma_total): {sigma_max:.6f} [Gy]")

```

A.5. Alanine and film comparison (conventional and FLASH)

```

1 from google.colab import drive # Grant access to your Google Drive
2 drive.mount('/content/drive', force_remount=True)

1 data_path = "drive/MyDrive/tesi_magistrale/data/new_measurements/IRSN"
    measurement/flash-conv_may_IRSN"

1 import pandas as pd
2 import numpy as np
3 import seaborn as sns
4 import matplotlib.pyplot as plt
5 from matplotlib import rcParams
6 import math
7 from statistics import stdev, mean

1 rcParams['figure.figsize'] = 7.5, 3.75

1 pellet = [1,2,3]
2 pellet_string = [f"{d}" for d in pellet]

3
4 amplitude_listIMconv7gy = []
5 for d in pellet_string:
6     df = pd.read_csv(f"{data_path}/Conv_7MeV_7Gy_P{d}_rubis.csv", sep=";",
7         skiprows=5000, engine='python', skipfooter=1, names=["magnetic
        field", "amplitude"])
8     amplitude_listIMconv7gy.append(df["amplitude"].max() - df["amplitude
        "].min())
9     sns.lineplot(df, x="magnetic field", y="amplitude", label=d)

10 std7gy = stdev(amplitude_listIMconv7gy)
11 mean7gy = np.mean(amplitude_listIMconv7gy)

12
13 print('For pellets [1,2,3] the IM amplitudes are',
14     amplitude_listIMconv7gy)
15 print('Mean amplitude:', mean7gy, 'Standard deviation:', std7gy)
16 print('Coefficient of variation for IM:', (std7gy/mean7gy) * 100, '%')

1 pellet = [1,2,3]
2 pellet_string = [f"{d}" for d in pellet]
3 sample = [1,2,3,4,5,6,7,8,9,10,11]
4 sample_string = [f"{s}" for s in sample]
5

```

```

6 mean_conv7gy = []
7 std_conv7gy = []
8
9 for d in pellet_string:
10    amplitude_list_conv = []
11    for s in sample_string:
12        df = pd.read_csv(f"{data_path}/Conv_7MeV_7Gy_P{d}_{s}.csv", sep=
13            ";", skiprows=3000, engine='python', skipfooter=3000, names=[ "magnetic_field", "amplitude"])
14        amplitude_list_conv.append(df["amplitude"].max() - df["amplitude"]
15            ".min()")
16
17        std_conv = stdev(amplitude_list_conv)
18        mean_conv = np.mean(amplitude_list_conv)
19        std_conv7gy.append(std_conv)
20        mean_conv7gy.append(mean_conv)
21
22 print('Mean_amplitudes:', mean_conv7gy, 'Standard_deviations:',
23       std_conv7gy)

```

```

1 normal_amplitude7gy_list = [mean / amplitude for mean, amplitude in zip(
2     mean_conv7gy, amplitude_listIMconv7gy)]
3
4 filmdose = [7.39, 7.50, 7.49]
5 normal_amplitude7gy_film_list = [normal / film for normal, film in zip(
6     normal_amplitude7gy_list, filmdose)]
7
8 print("Normalized_Amplitude_for_7_Gy_conventional:",
9       normal_amplitude7gy_film_list)

```

```

1 pellet = [1,2]
2 pellet_string = [f"{d}" for d in pellet]
3
4 amplitude_listIM7flash = []
5 for d in pellet_string:
6    df = pd.read_csv(f"{data_path}/Flash_7MeV_7Gy_P{d}_rubis.csv", sep=
7        ";", skiprows=5000, engine='python', skipfooter=1, names=[ "magnetic_field", "amplitude"])
8    amplitude_listIM7flash.append(df["amplitude"].max() - df["amplitude"]
9        ".min()")

```

```

9 std7 = stdev(amplitude_listIM7flash)
10 mean7 = np.mean(amplitude_listIM7flash)
11
12 print('FLASH\u20227\u2022Gy\u2022IM\u2022Mean: ', mean7, 'Standard\u00b7deviation:', std7)

1 normalamplitude7gyflash_list = [mean / amplitude for mean, amplitude in
2     zip(mean_flash_7gy, amplitude_listIM7flash)]
3 normalstd7gyflash_list = [std / amplitude for std, amplitude in zip(
4     std_flash_7gy, amplitude_listIM7flash)]
5
6 filmdose = [7.17, 7.15]
7 normalamplitude7gyfilmflash_list = [normal / film for normal, film in
8     zip(normalamplitude7gyflash_list, filmdose)]
9 normalstd7gyfilmflash_list = [normal / film for normal, film in zip(
    normalstd7gyflash_list, filmdose)]

df = pd.DataFrame(
    {
        "target_dose": ["7\u2022Gy"] * 5 + ["18\u2022Gy"] * 2,
        "type": ["Conventional"] * 3 + ["Flash"] * 4,
        "normalized_amplitude": normalamplitude7gyfilmflash_list +
            normalamplitude7gyfilmflash_list +
            normalamplitude18gyfilmflash_list,
        "absolute_error": absolute_error7conv + absolute_error7flash +
            absolute_error18flash,
        "relative_error": relative_error7conv + relative_error7flash +
            relative_error18flash
    }
)

import matplotlib.pyplot as plt
import numpy as np
from matplotlib.patches import Patch

target_doses = df['target_dose'].unique()
target_dose_mapping = {dose: idx for idx, dose in enumerate(target_doses)}
x_positions = np.zeros(len(df))
offset = 0.15
idx = 0

```

```

12 for dose in target_doses:
13     df_dose = df[df['target_dose'] == dose]
14     n = len(df_dose)
15     base_x = target_dose_mapping[dose]
16     positions = np.linspace(base_x - offset*(n-1)/2, base_x + offset*(n
17         -1)/2, n) if n > 1 else [base_x]
18     x_positions[idx:idx+n] = positions
19     idx += n
20
21 type_colors = {'Conventional': '#1f77b4', 'Flash': '#ff7f0e'}
22 colors = df['type'].map(type_colors)
23
24 fig, ax = plt.subplots(figsize=(5,5))
25 ax.bar(x_positions, df['normalized_amplitude'], yerr=df['absolute_error',
26     ], color=colors, width=offset*0.75, capsize=5, alpha=0.5)
27 ax.set_xticks([target_dose_mapping[dose] for dose in target_doses])
28 ax.set_xticklabels(target_doses)
29 plt.show()

```

A.6. Detector inter-comparison

```

1 import pandas as pd
2 import numpy as np
3 import seaborn as sns
4 import matplotlib.pyplot as plt
5 from matplotlib import rcParams
6 import math
7 from statistics import stdev, mean

1 depthpcc05 = [1, 3.09, 4.135, 5.18, 6.225, 7.27, 9.36, 11.45, 16.675,
2     21.9, 27.125, 32.35, 37.575]
3 depthpcc05 = [i-5.25 for i in depthpcc05] # Shift depth reference
4 depthdiamond = [1, 6.225, 11.45, 16.675, 21.9, 27.125]
5 pulse_number = 57

1 Troom = 20 # Room temperature in Celsius
2 Troomref = 20
3 press = 997 # Pressure in hPa
4
5 ktp = ((273.2 + Troom) / (273.2 + Troomref)) * (1013.25 / press)
6 kelec = 1 # Electrometer correction factor
7
8 plus300V = 4.93e-9

```

```

9 minus300V = 4.95e-9
10 kpol = ((plus300V + minus300V) / (2 * plus300V))
11
12 plus100V = 4.77e-9
13 ks = 1.198 - 0.875 * (plus300V / plus100V) + 0.6677 * ((plus300V /
14     plus100V) ** 2)
15 print("ktp=", ktp)
16 print("kelec=", kelec)
17 print("kpol=", kpol)
18 print("ks=", ks)

```

```

1 moyenneppc05 = [5.09, 4.94, 4.97, 5.28, 5.30, 5.23, 5.11, 4.96, 4.55,
2     3.68, 2.44, 1.18, 0.32]
3 stdppc05 = [0.17, 0.25, 0.03, 0.04, 0.06, 0.06, 0.03, 0.04, 0.06, 0.06,
4     0.03, 0.01, 0.003]
5 hpl = 1.019 # PPC05 chamber calibration factor
6
7 mqpl = [(i * 1e-9) / pulse_number for i in moyenneppc05]
8 mqplstd = [(i * 1e-9) / pulse_number for i in stdppc05]
9
10 mq = [ks * kpol * kelec * ktp * i * hpl for i in mqpl]
11 mqstd = [ks * kpol * kelec * ktp * i * hpl for i in mqplstd]
12
13 print("mq=", mq, "C/pulse")

```

```

1 kqq0ppc05 = 0.933
2 ndwq0ppc05 = 1.42e9 # Calibration factor
3
4 doseh2oppc05 = [i * kqq0ppc05 * ndwq0ppc05 for i in mq]
5 stddoseh2oppc05 = [i * kqq0ppc05 * ndwq0ppc05 for i in mqstd]
6
7 dosetotppc05 = [i * pulse_number for i in doseh2oppc05]
8 stddosetotppc05 = [i * pulse_number for i in stddoseh2oppc05]
9
10 print("Total_dose_PPC05:", dosetotppc05, "Gy", "with_std:",
11     stddosetotppc05)

```

```

1 moyennediamond = [0.98, 0.95, 0.84, 0.69, 0.44, 0.2]
2 stddiamond = [0.01, 0.002, 0.002, 0.0, 0.002, 0.0]
3
4 ndwq0diamond = 7.18e9 # Diamond calibration factor
5
6 dosetotdiamond = [i * ndwq0diamond * 1e-9 for i in moyennediamond]
7 stdtotdiamond = [i * ndwq0diamond * 1e-9 for i in stddiamond]

```

```

8
9 print("Total_dose_Diamond:", dosetotdiamond, "Gy", "with_std:",
       stdtotdiamond, "Gy")
10
11 plt.errorbar(depthpc05, dosetotppc05, yerr=stddosetotppc05, linestyle='--',
12               marker='o', markersize=4)
13 plt.errorbar(depthdiamond, dosetotdiamond, yerr=stdtotdiamond, linestyle='--',
14               marker='o', markersize=4)
15
16 plt.xlabel("Depth [cm]")
17 plt.ylabel("Dose_to_dosimeter [Gy]")
18 plt.legend(["PPC05_conv.", "Diamond_conv."])
19 plt.show()
20
21 epeaulanine = 5.68 # Alanine depth
22
23 alaninenormal = [0.0026918147128718105, 0.0027396278121695566,
24   0.002774172673351945]
25 filmdose = [7.39, 7.50, 7.49]
26 percerror = [0.009952598345697951, 0.012354535607139632,
27   0.017469607282335986]
28
29 print("Alanine_normalized_amplitudes:", alaninenormal, "with_relative_"
      "film_doses:", filmdose, "[Gy] at", epeaulanine, "cm")
30 print("Percentage_error:", percerror)
31
32 print("For_a_7_Gy_FLASH_irradiation:")
33 diamond = 7.44
34 alaninenormal = [0.0025501496422632498, 0.0026528068037445316]
35 filmdose = [7.17, 7.15]
36 percerror = [0.02653113557249775, 0.022148970775800865]
37 print("Alanine_normalized_amplitudes:", alaninenormal, "with_relative_"
      "film_doses:", filmdose, "Gy")
38
39 print("For_an_18_Gy_FLASH_irradiation:")
40 diamond = 18.56
41 alaninenormal = [0.002092825147731633, 0.0020917092776884063]
42 filmdose = [19.94, 19.92]
43 percerror = [0.0058163234310184475, 0.014558454620166977]
44 print("Alanine_normalized_amplitudes:", alaninenormal, "with_relative_"
      "film_doses:", filmdose, "Gy")

```

A.7. TOPAS simulation script

```

1 % Clear workspace and initialize
2 clc;
3 warning off all;
4 delete runjob.sh;
5
6 % Define parameters
7 nrjliste = [100]; % Energy list
8 Nbpart = 20000; % Number of particles
9 aperture = 72; % Aperture size
10 seed = 1;
11 cluster = 'CEA'; % Cluster name
12
13 % Define alanine pellet positions
14 alanineposition = (5-0.125)-[0 4 6 6.25 6.5 6.75 7 7.1 7.2 7.3 7.4 7.5
   7.6 7.7 7.8 7.9 8 8.1 8.2 8.3 8.4 8.5 8.75 9];
15 [s1, s2] = size(alanineposition);

```

```

1 for j = 1:length(nrjliste)
2     nrj = 0.9991 * nrjliste(j) + 1.6763;
3     plans_homogenes(); % Generate spot map
4     k = fieldsiz;
5     listespotsplan_TOPAS = listespotsplan_mbRT;
6
7     for l = 1:s2
8         create_plandescription_TOPAS_mbRT(size(listespotsplan_TOPAS', 2)
9             , listespotsplan_TOPAS', Nbpart);
10        namesimu = strcat('Main', num2str(j), '_f', num2str(k), '_ap',
11            num2str(l));
12        copyfile('Main.txt', strcat(namesimu, '.txt'));
13        delete Main.txt;
14    end
15 end

```

```

1 MAT = dicomread('Dose.dcm');
2 MATtot(:,:, :) = double(MAT(:,:,1,:));
3 LETd = dicomread('DoseAveragedLETd.dcm');
4 LETdtot(:,:, :) = double(LETd(:,:,1,:));
5 Zmc = 0.5:1:99.5;
6 plan(:,:, :) = sum(sum(MATtot(98:102, 98:102, :)));

```

```

1 alaninedepth = 1.25 + [0 4 6 6.25 6.5 6.75 7 7.1 7.2 7.3 7.4 7.5 7.6 7.7
   7.8 7.9 8 8.1 8.2 8.3 8.4 8.5 8.75 9] * 10;
2
3 for l = 1:s2

```

```

4 [Alaninedosetmp(1, 1), Alaninedosetmp(2, 1), filename_simu] =
5     lire_csvTOPAS_1voxel(strcat('dose_pellet_', num2str(l-1), '.csv'))
6 );
7
8 for l = 1:s2
9     Alaninedose(1, order_simu(1, l)) = Alaninedosetmp(1, l);
10    Alaninedose(2, order_simu(1, l)) = Alaninedosetmp(2, l);
11 end

```

```

1 figure(1);
2 hold on;
3 plot(Zmc, plan / plan(1,:) * absoluteexperimental(1,1), ':k', 'LineWidth',
4     , 1);
5 plot(datexp(:,1) + 0.25, datexp(:,2) / datexp(1,2) *
6     absoluteexperimental(1,1), 'b', 'LineWidth', 1);
7 errorbar(alaninedepth, Alaninedose(1,:)/ (Alaninedose(1,1)) *
8     absoluteexperimental(1,1), Alaninedose(2,:)/ (Alaninedose(1,1)), 'o',
9     , 'LineWidth', 2);
10 plot(alaninedepthexp, absoluteexperimental, 's', 'LineWidth', 2);
11
12 title('Bragg Peak in Water (100 MeV)');
13 xlabel("Depth [mm]");
14 ylabel("Normalized Dose to Medium [Gy]");
15 set(gca, 'FontName', 'Arial', 'FontSize', 14);
16 legend('Exp. data (ion chamber)', 'MC simulation (alanine)', 'Exp. data
17 (alanine)', 'Location', 'northwest');

```

A.8. Alanine TOPAS construction

A.8.1. Alanine dosimeter composition and geometry

```

1 # Alanine Material Composition
2 sv:Ma/Alanine/Components = 4 "Hydrogen" "Carbon" "Oxygen" "Nitrogen"
3 uv:Ma/Alanine/Fractions = 4 0.0791 0.4044 0.563591 0.1572
4 d:Ma/Alanine/Density = 1.42 g/cm3
5 s:Ma/Alanine/DefaultColor = "violet"

```

```

1 # EUDRAGIT NE 30D (2:1 molar ratio of Ethyl Acrylate and Methyl
2 Methacrylate)
3 Weight fraction of C = 0.5997
4 Weight fraction of H = 0.0807

```

```

4 Weight fraction of O = 0.3196
5 Density = 1.06 g/cm^3

```

```

1 # MYVATEX (Ethylene and Vinyl Acetate Copolymer, 10% Vinyl Acetate)
2 Weight fraction of C = 0.8264
3 Weight fraction of H = 0.1364
4 Weight fraction of O = 0.0372
5 Density = 0.9934 g/cm^3

```

A.8.2. Alanine dosimeter construction

```

1 # Alanine Dosimeter Composition
2 AERIAL Alanine Pellet:
3   - 91.63% Pure Alanine
4     - H 7.91%
5     - C 40.44%
6     - N 15.72%
7     - O 35.91%
8   - 6.37% EUDRAGIT NE 30D
9   - 2% MYVATEX

```

A.8.3. Alanine pellet geometry definition

```

1 # Alanine Pellet Geometry
2 b:Ma/Alaninepellet/BuildFromMaterials = "True"
3 sv:Ma/Alaninepellet/Components = 3 "Alanine" "Binder1" "Binder2"
4 uv:Ma/Alaninepellet/Fractions = 3 0.9163 0.0637 0.02
5 d:Ma/Alaninepellet/Density = 1.3789 g/cm3

```

A.8.4. Cylinder alanine geometry

```

1 # Cylinder of 4mm diameter and 2mm height
2 s:Ge/DemoCylinder/Type = "TsCylinder"
3 s:Ge/DemoCylinder/Parent = "World"
4 s:Ge/DemoCylinder/Material = "Alaninepellet"
5 d:Ge/DemoCylinder/TransX = 0 cm
6 d:Ge/DemoCylinder/TransY = 0 cm
7 #d:Ge/DemoCylinder/TransZ = 12 cm
8 d:Ge/DemoCylinder/RotX = 0 deg
9 d:Ge/DemoCylinder/RotY = 0 deg
10 d:Ge/DemoCylinder/RotZ = 0 deg
11 d:Ge/DemoCylinder/RMin = 0 mm

```

```
12 d:Ge/DemoCylinder/RMax          = 2 mm
13 d:Ge/DemoCylinder/HL           = 1.15 mm
14 d:Ge/DemoCylinder/SPhi         = 0 rad
15 d:Ge/DemoCylinder/DPhi         = 2*pi rad
16 s:Ge/DemoCylinder/Color        = "lightblue"
17 s:Ge/DemoCylinder/DrawingStyle = "FullWireFrame"
```

B | Appendix B

B.1. Images

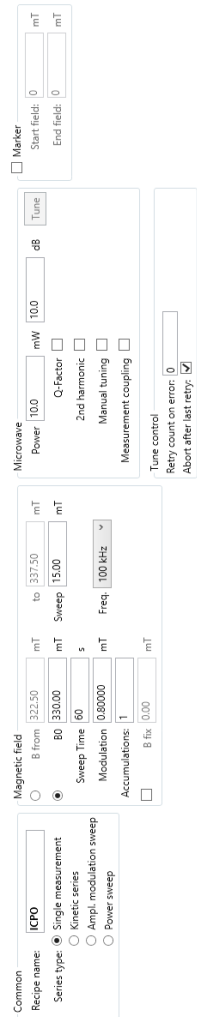


Figure B.1: The ICPO recipe was the standard for measuring all of the pellets from our experiments.

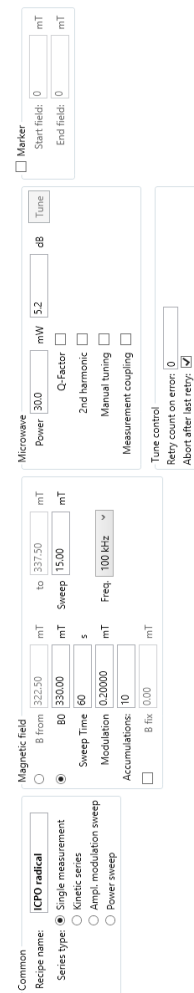


Figure B.2: The recipe used to create the different radicals spectrum by changing the power.

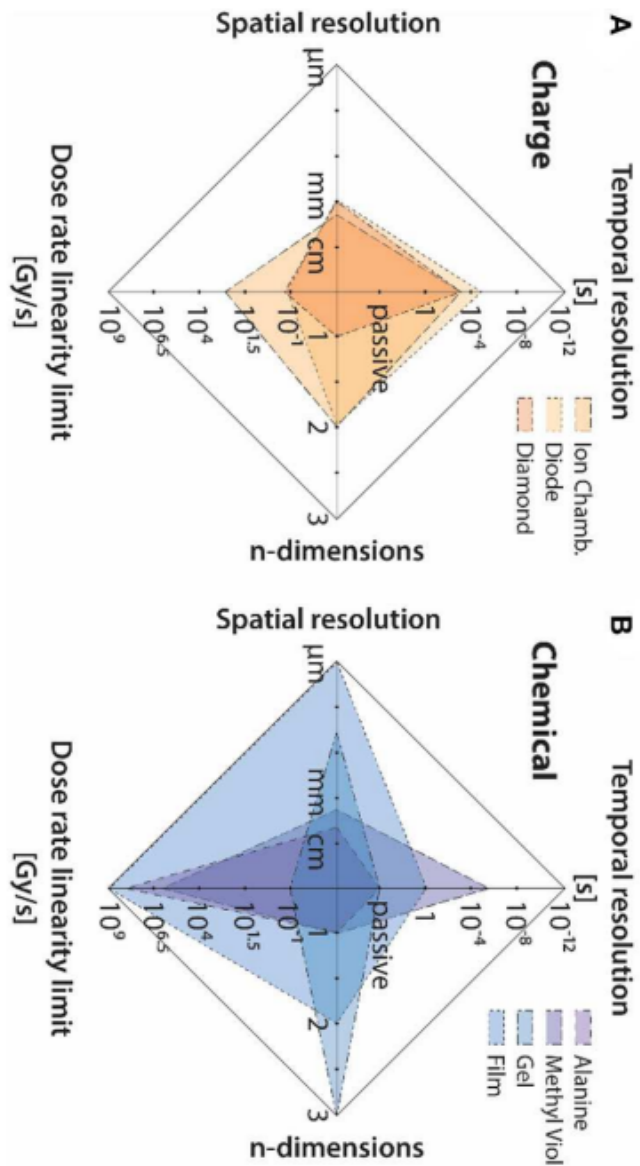


Figure B.3: Dosimeter comparison provided by Ashraf [40].

C | Appendix C

C.1. Tables

Table C.1: Results of data analysis of a conventionally irradiated pellet with 40 Gy of dose to water, with amplitudemodulation variation.

Modulation [mT]	Normalized amplitude [amp]	$\sigma_{\text{rep.}}$ [amp]	Dose read [Gy]	$\sigma_{\text{rep.}}$ [Gy]	RSD [%]
0.2	0.10	0.0009	34.56	0.37	0.90
0.4	0.11	0.0005	36.25	0.29	0.53
0.6	0.11	0.0009	38.23	0.39	0.85
0.8	0.12	0.0006	40.76	0.32	0.56
1	0.13	0.0005	43.36	0.31	0.45

Table C.2: Results of data analysis of a conventionally irradiated pellet with 40 Gy of dose to water, with microwave power variation. RSD represents the relative standard deviation.

Mic. Power [mW]	Normalized amplitude [amp]	$\sigma_{\text{rep.}}$ [amp]	Dose read [Gy]	$\sigma_{\text{rep.}}$ [Gy]	RSD [%]
1	0.17	0.001	57.59	0.65	1
5	0.14	0.0004	47.59	0.30	0.29
10	0.13	0.0004	44.31	0.29	0.35
15	0.10	0.0005	35.49	0.27	0.47
20	0.09	0.0006	30.34	0.28	0.69

Table C.3: Results of data analysis of a conventionally irradiated pellet with 40 Gy of dose to water, with time sweep variation. RSD represents the relative standard deviation.

Time [s]	PTP amplitude [amp]	$\sigma_{\text{reproducibility}}$ [amp]	$\sigma_{\text{reproducibility}}$ [Gy]	RSD [%]
5	344.95	3.71	0.41	1
10	342.14	2.09	0.26	0.6
30	343.25	1.28	0.20	0.3
60	343.34	1.29	0.20	0.3
120	343.09	0.82	0.17	0.2
240	338.58	1.61	0.22	0.4

Table C.4: Data analysis of a conventionally irradiated pellet with cavity temperature variation.

T_{cavity} [°C]	PTP Amplitude [amp]	Dose read [Gy]	σ_{acc} [amp]	σ_{acc} [Gy]
28.46	397.51	41.26	1.61	0.24
28.77	390.64	40.55	2.03	0.27
30.7	385.89	40.05	1.17	0.20
32.22	382.73	39.73	1.27	0.21
36.23	372.30	38.64	1.28	0.21
37.11	368.97	38.30	1.51	0.22
38.23	369.29	38.33	1.58	0.23

Table C.5: Results of data analysis for conventional irradiation in a phantom with 100 MeV protons using alanine pellets for each dose.

Dose to water [Gy]	PTP amplitude [amp]	IM amplitude [amp]	Normalized amplitude [amp]	$\sigma_{\text{rep.}}$ [amp]	$\sigma_{\text{rep.}}$ [Gy]
0	0	3086.21	0	0.0005	0.18
10	97.01	3080.97	0.03	0.0003	0.10
20	192.89	3096.15	0.06	0.0005	0.17
30	287.10	3088.70	0.09	0.0004	0.15
40	385.50	3079.02	0.12	0.0002	0.07

Table C.6: Results of data analysis of conventional irradiation in water with 100 MeV protons using alanine pellets for each dose.

Dose to water [Gy]	PTP amplitude [amp]	IM amplitude [amp]	Normalized amplitude [amp]	$\sigma_{\text{rep.}}$ [amp]	$\sigma_{\text{rep.}}$ [Gy]
0	0	3059.30	0	0.0005	0.19
5	45.71	3068.82	0.01	0.0006	0.20
10	88.23	3062.62	0.02	0.0006	0.20
20	172.71	3053.40	0.05	0.0003	0.11
30	259.17	3060.57	0.08	0.0009	0.30
40	348.52	3051.11	0.11	0.0010	0.33

Table C.7: Results of data analysis of conventional irradiation in phantom with 226 MeV protons of an alanine pellet for each dose.

Dose to water [Gy]	PTP amplitude [amp]	IM amplitude [amp]	Normalized amplitude [amp]	$\sigma_{\text{rep.}}$ [amp]	$\sigma_{\text{rep.}}$ [Gy]
0	0	5451.33	0	0.0003	0.15
10	143.41	5435.71	0.02	0.0003	0.16
20	276.64	5443.22	0.05	0.0002	0.15
30	411.21	5445.29	0.07	0.0005	0.24
40	551.44	5450.53	0.10	0.0005	0.26

Table C.8: Results of data analysis of conventional irradiation in phantom with 7 MeV electrons of an alanine pellet for each dose.

Dose to water [Gy]	PTP amplitude [amp]	IM amplitude [amp]	Film reading [Gy]	Normalized amplitude [amp]	σ_{total} [amp]
7	108.15	5437.12	7.39	0.0027	0.00013
7	110.78	5391.49	7.50	0.0027	0.00014
7	112.62	5420.45	7.49	0.0028	0.00014

Table C.9: Results of data analysis of FLASH irradiation in phantom with 7 MeV electrons of an alanine pellet for each dose.

Dose to water [Gy]	PTP amplitude [amp]	IM amplitude [amp]	Film reading [Gy]	Normalized amplitude [amp]	σ_{total} [amp]
7	101.71	5563.07	7.17	0.0025	0.00014
7	103.61	5462.80	7.15	0.0026	0.00014
18	232.00	5559.56	19.94	0.0020	0.00010
18	226.20	5429.01	19.92	0.0020	0.00010

Table C.10: Results of data analysis of conventional irradiation in phantom with 100 MeV protons for each dose using alanine pellets.

Dose to water [Gy]	PTP amplitude [amp]	IM amplitude [amp]	Normalized amplitude [amp]	$\sigma_{rep.}$ [amp]	$\sigma_{rep.}$ [Gy]
0	0	5450.53	0	0.0003	0.19
10	146.59	5440.11	0.02	0.0001	0.16
20	287.99	5440.12	0.05	0.0002	0.20
30	423.41	5442.76	0.07	0.0003	0.25
40	555.95	5450.53	0.10	0.0002	0.29

Table C.11: Results of data analysis of conventional irradiation in phantom with 100 MeV protons of an alanine pellet for each dose.

Pellet N°	Depth [cm]	PTP amplitude [amp]	IM amplitude [amp]	Normalized amplitude [amp]	Dose interpolated [Gy]
1	0	88.06	3110.94	0.011	9.94
2	6	150.05	3100.65	0.020	17.31
3	6.4	164.97	3100.92	0.022	19.08
4	7	217.81	3100.70	0.029	25.23
5	7.4	336.77	3104.62	0.045	38.61
6	7.8	20.42	3097.83	0.003	2.23
7	8.2	7.71	3104.65	0.001	0.84
8	8.6	6.90	3103.42	0.001	0.75

Table C.12: Results of data analysis of conventional irradiation in phantom with 100 MeV protons of an alanine pellet for each dose.

Pellet N°	Depth [cm]	PTP amplitude [amp]	IM amplitude [amp]	Normalized amplitude [amp]	Dose interpolated [Gy]
1	0	84.58	3046.62	0.011	9.27
2	4	111.90	3035.11	0.015	12.56
3	6	150.71	3040.91	0.020	17.14
4	7	255.81	3042.71	0.035	29.30
5	7.25	329.54	3036.70	0.045	37.58
6	7.4	321.18	3031.85	0.044	36.70
7	7.5	257.69	3027.48	0.035	29.66
8	7.6	177.93	3031.32	0.024	20.42
9	7.75	26.44	3036.53	0.003	2.75
10	8	12.18	3036.70	0.001	1.27
11	8.25	10.50	3029.60	0.001	1.09
12	8.5	12.43	3037.41	0.002	1.29

List of Figures

1.1	Spread out Bragg peak (SOBP) and comparison with a high energy proton beam (shaded area). The proton's range is adapted to the tumor's depth.	3
1.2	Relative dose deposition in depth in water for different particles.	5
1.3	Cylinder model for energy deposition and cut-off definitions used for (un)restricted LET calculations	6
1.4	Differences between sparsely and densely ionizing particles (X-rays and carbon ions) and interactions at the DNA scale.	8
1.5	Graphical representation of therapeutic ratio.	10
1.6	Summary of mechanistic hypothesis for the FLASH effect.	13
1.7	Typical temporal characteristics of different accelerators.	14
2.1	Scheme of the ion chamber.	20
2.2	Saturation behavior of current (I) with increasing voltage (V).	20
2.3	Scheme of the semiconductor detector.	22
2.4	Semiconductor's band structure.	22
2.5	Gurney-Mott mechanism for latent-image formation.	27
2.6	EBT active component polymerization: upon exposure to photon energy or thermal energy, the linear structure (a) undergoes polymerization, leading to the formation of cross-linked structures (b) and (c) through a resonance-stabilized process.	28
2.7	OD as a function of $\log(\text{time})$ for a period of 24 H post irradiation for doses between 0 to 18 Gy.	29
2.8	Example of a sensitometric curve for film.	30
2.9	The film dosimeter placed in the EPSON scanner.	31
2.10	An example of what the EPSON scanner gives as a numerized result.	31
2.11	Elaboration of the film using the Matlab code.	31
2.12	Evolution of dose over time for the film dosimeter.	32
2.13	The molecular structure of alanine.	33
2.14	Signal of each one of the alanine radicals.	33

2.15 When the magnetic field is scanned, the energies of the two spin states of an unpaired electron diverge. At the magnetic field for which the energy difference between the two electron spin states is equal to $h\nu$ for the spectrometer, there is absorption of energy by the spins, which is called resonance.	36
2.16 Splitting of an EPR signal due to the local field of a neighboring spin = 1/2 nucleus	37
2.17 Example of saturation behavior.	39
2.18 Criteria for the evaluation of an EPR dosimeter material.	42
2.19 The cyclotron and its top view.	50
2.20 Scheme of a beam rotating system gantry.	50
2.21 Irradiation setup at the proton gantry. Lasers are used to verify the dosimeter's alignment.	51
2.22 The electron FLASH LINAC head with the applicator.	53
2.23 Experimental setup showing the water tank and straw alignment before irradiation.	54
2.24 The peak-to-peak signal variation of EPR in function of the depth.	54
2.25 Ion chamber with the alanine and the tape: the final waterproofing setup. .	55
3.1 EPR peak-to-peak (PTP) signal for a 40 Gy pellet irradiated with 100 MeV protons in phantom. The legend shows the different modulation amplitudes of the study.	58
3.2 Correlation between normalized amplitude and modulation amplitude. Each label represents the dose interpolated from the calibration in section 3.2.1.	59
3.3 The relative standard deviation over different modulation amplitudes.	59
3.4 EPR PTP signal for a 40 Gy pellet irradiated with 100 MeV protons in phantom. The legend shows the different microwave powers analyzed.	61
3.5 Internal marker variation (the signal between 340 mT to 345 mT) following a change of microwave power. The EPR signal we are interested in for the dose lays between 328 and 330 mT.	62
3.6 The squared microwave power is linked to amplitude with a squared function behavior.	62
3.7 Fit of squared microwave power values against normalized amplitude. Each label represents the dose interpolated from the calibration in section 3.2.1.	63
3.8 Behavior of the RSD with microwave power variation.	64
3.9 EPR signal for a 40 Gy pellet irradiated with 100 MeV protons in phantom. The times in the legend are relative to the EPR time sweeps.	64

3.10	The relative standard deviation for different sweep times.	65
3.11	EPR signal for a 40 Gy pellet irradiated with 100 MeV protons in phantom. The legend shows the EPR cavity temperatures.	66
3.12	The variation of the amplitude as a function of the temperature, which shows a decreasing trend.	66
3.13	The linear correlation between amplitude and temperature.	67
3.14	Calibration curve for 100 MeV protons in solid phantom, obtained with EPR signal amplitude analysis from alanine pellets.	68
3.15	Calibration curve for 100 MeV protons in water, obtained with EPR signal amplitude analysis from alanine pellets.	69
3.16	Evaluation of the dose delivered to a pellet irradiated with an unknown (or independent) amount of dose, using the calibration curve for 100 MeV protons in a solid water phantom.	71
3.17	The two different calibration curves for 100 MeV and 226 MeV proton energy irradiation in alanine. Error bars were not reported to improve readability but are presented in Table C.10 and C.7.	72
3.18	EPR signal for alanine pellets irradiated with 100 MeV protons in water inside of a ion chamber "shell". The numbers in the legend are relative to the pellet number, and with its increase the depth also increases.	73
3.19	Bragg peak depth-dose profiles obtained for alanine dosimeter and ion chamber.	74
3.20	Bragg peak shapes for alanine dosimeter and ion chamber with the new data point relative to the old experiment in the area of the Bragg peak. . .	74
3.21	EPR signal for alanine pellets irradiated with 100 MeV protons in water inside of a ion chamber "shell". The numbers in the legend are relative to the pellet number, and with its increase the depth also increases.	75
3.22	Bragg peak shapes for alanine dosimeter and ion chamber, with increased sampling within the Bragg peak.	76
3.23	Bragg Peak shape for ion chamber, alanine and water, with LET (TEL) distribution in alanine and water.	77
3.24	Bragg peak from experimental data and simulation with RE estimation. .	78
3.25	EPR spectra of γ irradiated alanine (low LET). The central narrow line is denoted by Y, the central wider line is denoted by X.	80
3.26	EPR spectra of α irradiated alanine (high LET).	81
3.27	EPR spectra of alanine irradiated at different microwave power: 2 mW, 10 mW and 30 mW. Pellet 1 corresponds to entrance and pellet 25 to the peak. The spectra display signals related to different radicals.	82

3.28 The structures of alanine radicals.	82
3.29 In this bar plot we see the comparison of conventional and FLASH irradiations on alanine, grouped in 7 Gy and 18 Gy of dose delivered by the beam.	85
3.30 The diamond and ion chamber dose profiles.	85
B.1 The ICPO recipe was the standard for measuring all of the pellets from our experiments.	117
B.2 The recipe used to create the different radicals spectrum by changing the power.	117
B.3 Dosimeter comparison provided by Ashraf [40].	118

List of Tables

1.1	Average values for energy and range in water for particles employed in radiotherapy.	5
1.2	These limits apply only to doses received above the normal local natural background radiation.	16
2.1	Values of N_{D,w,Q_0} for different types of dosimeters.	25
3.1	Results of conventional irradiation on the active dosimeters.	86
3.2	Results of conventional irradiation on passive dosimeters, with each film dosimeter paired with the alanine dosimeter it was irradiated with.	86
3.3	Results of FLASH 7 Gy irradiation.	87
3.4	Results of FLASH for 18 Gy irradiation.	87
C.1	Results of data analysis of a conventionally irradiated pellet with 40 Gy of dose to water, with amplitudemodulation variation.	119
C.2	Results of data analysis of a conventionally irradiated pellet with 40 Gy of dose to water, with microwave power variation. RSD represents the relative standard deviation.	119
C.3	Results of data analysis of a conventionally irradiated pellet with 40 Gy of dose to water, with time sweep variation. RSD represents the relative standard deviation.	119
C.4	Data analysis of a conventionally irradiated pellet with cavity temperature variation.	120
C.5	Results of data analysis for conventional irradiation in a phantom with 100 MeV protons using alanine pellets for each dose.	120
C.6	Results of data analysis of conventional irradiation in water with 100 MeV protons using alanine pellets for each dose.	120
C.7	Results of data analysis of conventional irradiation in phantom with 226 MeV protons of an alanine pellet for each dose.	120
C.8	Results of data analysis of conventional irradiation in phantom with 7 MeV electrons of an alanine pellet for each dose.	120

C.9 Results of data analysis of FLASH irradiation in phantom with 7 MeV electrons of an alanine pellet for each dose.	121
C.10 Results of data analysis of conventional irradiation in phantom with 100 MeV protons for each dose using alanine pellets.	121
C.11 Results of data analysis of conventional irradiation in phantom with 100 MeV protons of an alanine pellet for each dose.	121
C.12 Results of data analysis of conventional irradiation in phantom with 100 MeV protons of an alanine pellet for each dose.	121